2009

EXPERIMENTAL STUDY OF THE SCALAR CONCENTRATION FIELD IN TURBULENT FLOWS

Partha Sarathi

EXPERIMENTAL STUDY OF THE SCALAR CONCENTRATION FIELD IN TURBULENT FLOWS

(Spine Title: Scalar concentration field in turbulent flows)

(Thesis Format: Monograph)

by

Partha Sarathi

Department of Civil and Environmental Engineering
Faculty of Engineering Science

A thesis submitted in partial fulfillment
of the requirements for the degree of
Doctor of Philosophy

The School of Graduate and Postdoctoral Studies
The University of Western Ontario
London, Ontario, Canada

THE UNIVERSITY OF WESTERN ONTARIO
THE SCHOOL OF GRADUATE AND POSTDOCTORAL STUDIES

CERTIFICATE OF EXAMINATION

Supervisor	Examiners
Dr. Gregory A. Kopp	Dr. Denis O'Carroll
Co-supervisor	Dr. Kamran Siddiqui
Dr. Paul J. Sullivan	Dr. Colin Denniston
	Dr. Nils Mole

The thesis by
Partha Sarathi

Entitled

EXPERIMENTAL STUDY OF THE SCALAR CONCENTRATION FIELD IN TURBULENT FLOWS

is accepted in partial fulfillment of the
requirements for the degree of
Doctor of Philosophy

Date_____

_____
Chair of the Thesis Examination Board

ABSTRACT

An experimental investigation has been carried out in a relatively simple turbulent flow in order to directly measure for the first time the Expected Mass Fraction (EMF) of the state of a contaminant concentration field within a contaminant cloud. Particle image velocimetry (PIV) and Planar laser induced fluorescence (PLIF) were used to measure simultaneous velocity and concentration fields, respectively. The EMF is a relatively simple measure of the state of a contaminant cloud. It has been shown that the EMF is approximately self-similar when concentrations are normalized by the centreline mean concentration. It has been shown that a reasonable approximation of the EMF moments is possible by using the centreline absolute moments. The results are compared with the theoretical and experimental results established for a line source of scalar in grid turbulence.

The two closure approximations in the evolution of the moments of the probability density function of a scalar concentration are validated experimentally using simultaneous measurements of velocity and concentration fields. The effect of molecular diffusivity is brought into the convective closure approximation by introducing a representative 'local concentration scale', which appears to be a robust improvement in the approximation and can be estimated directly from the centreline moments. The concept of fractal scaling is used in dealing with under-resolved dissipation measurements by using an extrapolation scheme. This leads to two distinct self-similar regions within the Batchelor scale and the Integral scale, separated by the Kolmogorov scale, in the measured constant of the dissipative closure approximation.

Key words: Turbulent diffusion, Scalar, Contaminant plume, Dispersion, Particle image velocimetry (PIV), Planar laser induced fluorescence (PLIF), self-similarity, Expected mass fraction (EMF), Probability density function (PDF), Moment, Batchelor scale.

To my Parents

ACKNOWLEDGEMENTS

I am extremely grateful to my supervisors Dr. Gregory A. Kopp and Dr. Paul J. Sullivan for their constant help and motivation during the past four years. They are truly great mentors. I would also like to express my sincere gratitude to Dr. Roi Gurka (Ben-Gurion University, Israel) for his encouragement and guidance during this study.

I would like to thank Mr. Christopher Vandelaar for his prompt help and support in building and maintaining the experimental setup for this study. Special thanks to my friends and fellow graduate students for their encouragement and their interest shown in this study.

I would like to express my affectionate appreciation to my parents for their encouragement and consideration during my long academic education.

TABLE OF CONTENTS

LIST OF TABLES

LIST OF FIGURES

LIST OF NOTATIONS

$\langle \cdot \rangle$	Ensemble average
A	Area
B	Proportionality constant
B_n	Proportionality factor
$B(\phi,\psi)$	Parameter for Beta distribution function
C	Mean concentration
C_o	Centreline mean concentration
C'	Relative mean concentration
$\hat{C}$	Normalized mean concentration
$\widetilde{C}$	Concentration integrated over the cross-section
D_K	Dimension of the *K*-zone
D_B	Dimension of the *B*-zone
$F(f)$	Power spectral density
G	Proportionality constant
$G(\cdot)$	Gamma function
I	Fluorescence intensity
K	Pressure drop coefficient
K_n	Normalized Central moments
$K(t)$	Spatial variance growth rate
L, L_x	Integral length scale
M	Mesh size of the grid
M_n	EMF moments
$\hat{M}$	Normalized EMF moments
Q	Released mass in the contaminant cloud
$\overline{Q}$	Average concentration flux across the vertical plume axis
$R(\tau)$	Lagrangian autocorrelation coefficient
Re	Reynolds number
Re_λ	Reynolds number based on Taylor Micro-scale

S	Proportionality constant
Sc	Schmidt number
T, t, t'	Time
T_L	Lagrangian integral constant
U	Mean velocity
U_o	Nozzle exit velocity
U_{ref}	Free stream velocity
$X(t)$	Lagrangian displacement
a, k	Distribution parameters
a_w	Laser attenuation coefficient in water
a_o	Laser attenuation coefficient in fluorescence
a_n, b_n	distribution parameters for normalized central moments
$a.s.$	an integral over space
b	Universal constant
c	Universal constant
d	Length scale of the cross-section of a pipe or channel
$\bar{f}$	Mean concentration of source fluid
$f(\theta;x,t)$	Probability density functions of source fluid
$\bar{g}$	Mean concentration of non-source fluid
$g(\theta;x,t)$	Probability density functions of non-source fluid
h	Height of the water tunnel
l	screen mesh size
m_n	Absolute moments
p	Probability density function
q	Expected Mass Fraction (EMF) function
$r(x',t)$	Location of the centre-of-mass
t_L	Lagrangian time scale
u	Streamwise component of velocity
u_*	Friction velocity

$u'(t)$	Lagrangian velocity
v	Vertical component of velocity
u_r, u_θ, u_x	Components of the velocity in cylindrical coordinate system
$v(t)$	relative velocity of the two particles
w	Steady source emission rate
$\boldsymbol{x}$	Location as a vector
x	streamwise component of the displacement
x'	streamwise component of the motion relative to an axis
y	Lateral component of the displacement
$\bar{y}$	Location of the centre-of-mass
z	Vertical component of the displacement
z_o	Roughness height
σ	Spatial variance
θ	Concentration
θ_o	Source concentration
Γ	Calibrated concentration
κ	Molecular diffusivity
π	Probability of being in marked fluid
δ	Delta function
η_B	The Batchelor scale
η	The Kolmogorov scale
η_{OC}	The Obukhov-Corrsin cut-off length scale
ν	Kinematic viscosity
ε	Rate of energy dissipation
τ	Time lag
θ_a, θ_b	Arbitrary values of concentration
θ_{max}	Maximum measured concentration at a location
μ_n	Central moments

λ_n	Constant parameters
α,β	Distribution parameters
Θ	Normalized maximum value of concentration
ϕ,ψ	Parameters used in Beta distribution calculation
θ_o^*	Local concentration scale based on convective closure approximation
θ_o^+	Local concentration scale based on centreline absolute moments
χ	Open area ratio for screens
λ	Taylor micro-scale
μ_{nf}	Central moments of $\bar{f}$
μ_{ng}	Central moments of $\bar{g}$
θ_1	Equivalent background concentration
θ_2	Equivalent source concentration
γ, ξ	Constants
Ω	Empirical factor

Chapter 1: Introduction

1.1 Background

In modern society, the production of hazardous materials has increased exponentially, as have their diverse uses. Large numbers of chemical disasters in the past show that the accidental release of hazardous materials is an important problem. On top of that, regular industrial emissions from stacks or rooftop vents cause a wide range of negative consequences for human health and productivity. In hazard studies, it is important to know the mixing and transport of such contaminants. In most natural and engineered environments the flows are turbulent, greatly increasing both the mixing and complexity. Common examples include contaminant discharges in water bodies, smoke plumes in the atmosphere, and chemical mixing in reactors.

The problem to be addressed here is accidental releases of hazardous contaminants into the atmosphere. In assessing the hazards from an accidental release, the greatest danger of exposure comes from the highest concentrations within the cloud of the contaminant gas. For flammable gases, a regime of particular interest is when the concentrations above the flammable limit or within an arbitrary limit. However, sometimes a very small amount of contaminant (parts per billion) can be detected through human olfaction (e.g. malodor).

1.2 Why this problem is difficult

Environmental flows are in a turbulent state of motion. In turbulent flows variables such as velocity and scalar concentration are random. The magnitude of the fluctuations of scalar concentration is well illustrated by Figure 1.1, which shows a time series of a fixed point measurement of concentration downstream of a continuously emitting point source. The figure is very much like various observations within the atmospheric boundary layer, which show frequent peaks in concentration that are many standard deviations above the mean value. A contaminant cloud in atmospheric flows can be spread out over kilometers by the large scale turbulent velocity components. However, the reduction of concentration values (e.g., the peaks in Figure 1.1) takes place only through molecular diffusion at scales comparable with the conduction cut-off length (about 1 mm in the atmospheric boundary layer). Normally, one would investigate the probability density function (PDF) of concentration as it evolves in time at each location in space to quantify the concentration field. The PDF is theoretically difficult – the equations that govern its evolution are intractable in even the simplest flows, and challenging to measure in experimental flows. Even in the laboratory, one needs to use repeated releases of many clouds to approximate even the crudest statistics. Additional difficulties arise in environmental flows in that they are intrinsically, to some extent, unsteady and spatially inhomogeneous.

1.3 A new framework

One would like to cast the problem of a sudden release of contaminants in a simpler framework than provided by the PDF, but one which still contains relevant

information. This would be practically consistent with release details that would be known for the accidental spill of contaminant materials. To this end, we consider the problem in three parts. These are the location of the cloud, the size of the cloud and the state of the concentration within the cloud (see the sketch in Figure 1.2). The state of the concentration in the cloud will be given by the Expected Mass Fraction (EMF) function (Heagy and Sullivan 1996), which is the focus of this thesis. All values of concentration within each realization of the cloud are used in the compilation of the EMF. Thus, the spatial dependence present in the PDF is eliminated, such that relatively little variation between realizations is expected and the shape of the EMF is expected to be reasonably simple. The Expected Mass Fraction portrays the fraction of the released mass found over various concentrations and it records the change of concentration values as the mass fraction migrates from higher to lower values of concentration as the cloud evolves in time (Heagy and Sullivan 1996). The attractiveness of this concept has led to some theoretical discussion and use of indirect approximations based on measured data. One such study suggests that the EMF can be simply represented by a Beta function (which can be thought of as using the leading term of the Jacobi orthogonal polynomial expansion as an approximation). However, no direct measurement of the EMF has been made prior to the current investigation. In Chapter 3, a description of the experiments using a dye plume from a line source in grid turbulence is given, in which the instantaneous concentration is used to compile the EMF. Thus, the objectives of the thesis are to measure for the first time the Expected Mass Fraction (EMF) function and to assess the other expressions as necessary along the way.

1.4 Plan of the presentation

The order of the thesis is as follows. In Chapter 2, a framework for the analysis is presented in detail from the existing literature. Chapter 3 describes the experimental setup, measurement techniques and flow characteristics. Chapter 4 presents the experimental results and a discussion of the results follows in Chapter 5. Concluding remarks with recommendations for extending this study are given in Chapter 6.

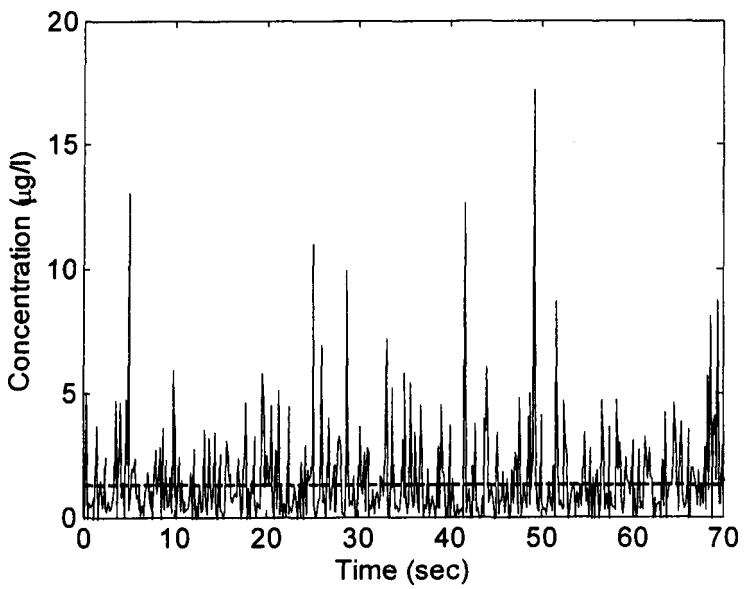

Figure 1.1: Time series of the concentration measurements in a plume (the dashed line is the time average of the concentration measurements).

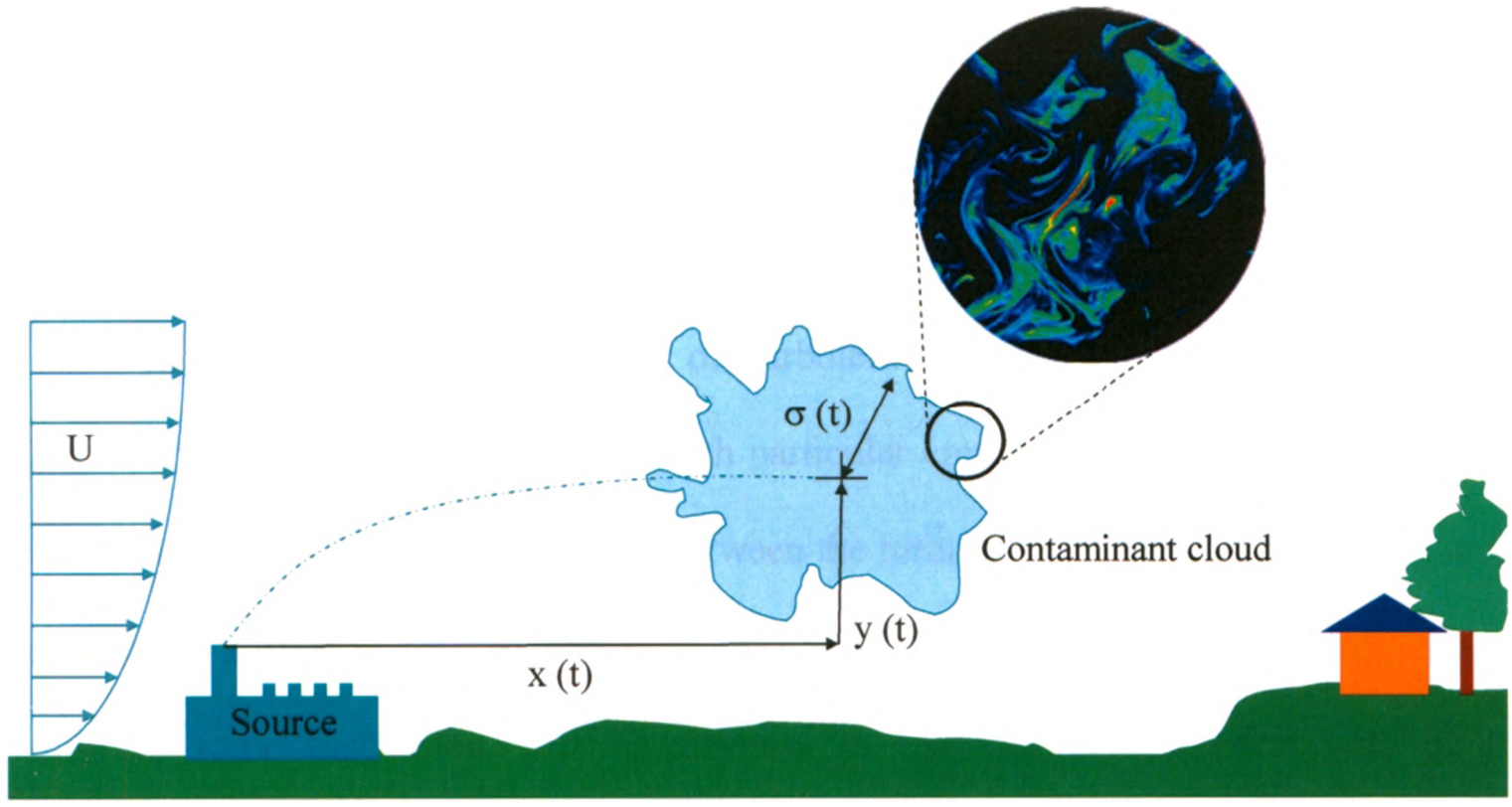

Figure 1.2: A conceptual framework for contaminant cloud dispersion.

Chapter 2: Turbulent Diffusion

2.1 Introduction

In this chapter the problem of turbulent diffusion is discussed, within the framework set out in Chapter 1, and with particular emphasis on contaminant clouds. In particular, a distinction will be drawn between the turbulent motions that contribute to the location (§ 2.3), size (§ 2.4) and state (§ 2.5) of contaminant concentration fields. In addition, some discussion will be devoted to the high-concentration tails of the probability density function in § 2.6. This range of (high) concentration values, with possibly low probability of occurrence, can be of inordinately high consequence, as discussed in Chapter 1.

The approach taken here is to use lower-order moments to approximate the PDF and EMF function. A proposed closure scheme that provides a simple and relatively general solution for the equation governing the evolution of moments, and which has received some limited but encouraging qualitative comparison with data, is discussed in § 2.7. The primary objective of this experimental investigation is to directly measure the EMF function with a secondary objective to assess the terms of the proposed closure scheme.

There is an inevitable problem of adequate spatial and temporal resolution in measuring concentration values in a turbulent flow. In Chapter 4, an extrapolation scheme to approximate continuum-level resolved values from more poorly resolved ones

is developed. As background to that development, discussion is provided in § 2.8 on self-similarity within the scalar field.

2.2 Statistical description of scalar diffusion

In this study, we consider the concentration $\Gamma(\boldsymbol{x},t)$, in units of mass per unit volume, of a miscible contaminant fluid at a position located by vector, $\boldsymbol{x}$, at time, t, within the turbulent host fluid. Concentration is a random variable in turbulent flows such that the only reproducible quantity is an ensemble average. Usually, for steady flows, ensemble averages are approximated experimentally by taking time averages. The important case of the sudden release of contaminant resulting in a contaminant cloud requires a number of repeated releases to approximate the ensemble average.

In assessing the hazards due to an accidental release, the greatest danger from the exposure of hazardous gases dispersing in the atmosphere often comes from the highest concentrations within the cloud of the contaminant gas (ten Berge et al. 1986; Davies 1989; Griffiths 1991). In order to evaluate the risk involved in exceeding a dangerous level of contaminants, it is natural to investigate the probability density function, $p(\theta;\boldsymbol{x},t)$, for the contaminant concentration. The probability density function (PDF) is defined as

$$p(\theta;\boldsymbol{x},t)d\theta = prob\{\theta \le \Gamma(\boldsymbol{x},t) < \theta + d\theta\}. \tag{2.1}$$

The equation for the evolution of the PDF can be derived from the convective diffusion equation (Chatwin 1990),

$$\frac{\partial p}{\partial t} + \nabla\cdot\left(p\langle u|\Gamma=\theta\rangle\right) = \kappa\nabla^2 p - \kappa\frac{\partial^2}{\partial\theta^2}\left(p\langle(\nabla\Gamma)^2|\Gamma=\theta\rangle\right), \tag{2.2}$$

where $\langle \cdot | \cdot \rangle$ denotes the conditional expected value and κ is the molecular diffusivity. In general, knowledge of all of the moments, m_n, defined as

$$m_n(\mathrm{x},t) = \langle \Gamma(\mathrm{x},t)^n \rangle = \int_o^\infty \theta^n p(\theta;\mathrm{x},t) d\theta, \tag{2.3}$$

is equivalent to the PDF, and one expects to get a reasonable approximation to the probability density function from the inversion of joint set of low order moments (Derksen and Sullivan 1990). The equation for the moments is

$$\frac{\partial m_{n+1}}{\partial t} + \nabla \cdot \langle u \Gamma^{n+1} \rangle = -n(n+1)\kappa \langle \Gamma^{n-1} (\nabla \Gamma)^2 \rangle + \kappa \nabla^2 m_{n+1}. \tag{2.4}$$

The diffusive term, $\kappa \nabla^2 m_{n+1}$, is generally much less than the convective term, $\nabla \cdot \langle u' \Gamma^{n+1} \rangle$, and can be ignored. It would appear that the equations for the evolution of the moments are less complex than those for the PDF; however, it still remains intractable due to the lack of closure of the two terms.

The only agency to reduce concentration is the molecular diffusivity, κ. Without molecular diffusivity the only outcome at any position, x, and time, t, is either zero or, for a uniform source, the initial uniform concentration, θ_o. In this case, the PDF is

$$p(\theta;x,t) = (1 - \pi(x,t))\delta(\theta) + \pi(x,t)\delta(\theta - \theta_o), \tag{2.5}$$

where $\pi(x,t)$ is the probability of being in marked fluid. That is $C(x,t) = \pi(x,t)\theta_o$, where we denote the mean concentration, $m_1(x,t)$, as $C(x,t)$ hereafter as a matter of convention and convenience, and all the moments are

$$m_{n+1}(x,t) = \theta_o{}^n C(x,t). \tag{2.6}$$

The total moments, when $\kappa = 0$, are conserved,

$$\int_{a.s.} m_{n+1}(\mathbf{x},t)d\,\mathbf{x} = \theta_o^{\,n} \int_{a.s.} C(\mathbf{x},t)d\,\mathbf{x} = \theta_o^{\,n} Q\,. \tag{2.7}$$

where *a.s.* denotes the volume integral is taken over all space while $Q = \int_{a.s.} C(\mathbf{x},t)d\mathbf{x}$ is the total release mass in the cloud. The only agency to take moments out of the system is the molecular diffusion.

When a "blob" of contaminant is released in a turbulent flow the turbulent convective motions stretch the contaminant into ever-thinning sheets and strands until the thinning (due to stretching) is balanced by thickening due to molecular diffusivity. This occurs at the conduction cut-off length, $\eta_B = (\nu\kappa^2/\varepsilon)^{1/4}$, where, ν is the kinematic viscosity and ε is the rate of turbulent energy dissipation per unit mass. η_B is of the order 10^{-3}-10^{-5} m in most flows. Experimental evidence of both Dahm et al. (1991) and Corriveau and Baines (1993) show virtually all of the contaminant to be confined within such sheets and strands. This fine scale texture is manifest in fixed point measurements where the "spiky" concentration record, as in Figure 1.1, is observed (see for example Mylne and Mason 1991 for field measurements and Schopflocher 1991 for laboratory results). These high concentration spikes, frequently many standard deviations above the mean, cause significant measurement issues to arise (pertaining to spatial and temporal resolution (Schopflocher and Sullivan 1998)).

The mean concentration is relatively insensitive to either molecular diffusivity or experimental resolution. In the equation for the mean concentration ($n = 0$ in (2.4)), the last term on the right hand side, $\kappa\nabla^2 m_{n+1}$, is small with respect to the other terms.

Therefore the mean concentration, although the easiest to predict and to measure, does not tell us anything about concentration reduction. Higher order moments are extremely sensitive to both κ and experimental resolution. The instantaneous gradients that appear in the right hand side of the moment equation (2.4) are large over the thin sheets and strands. Coarser spatial and temporal resolutions limit the extreme values of concentration near zero and the maximum concentration and the moments are increasingly reduced with the moment order. For example, in a laboratory experiment on the centreline of a contaminant jet, Sakai et al. (discussed in Chatwin and Sullivan 1993) showed that the mean square value of concentration, when the spatial resolution is improved over the normally used values, to be increased by a factor of two.

Given the complexities of contaminant diffusion in environmental flows, which are to some extent intrinsically unsteady and inhomogeneous, making approximations for ensemble averages is problematic, and particularly so, in the case of a contaminant cloud. It is worth noting that in the well controlled laboratory experiments of Hall et al. (1991), where a tent full of contaminant was released in a boundary layer only the mean concentration could be measured confidently with 100 repeat releases.

So, it is clearly desirable to obtain a simple measure of the contaminant concentration reduction. One can cast the problem of a contaminant cloud into a framework in which one seeks the answers to three basic questions. These are: Where is it? How big is it? And, what is the state of concentration within the cloud? The answers to these questions, as will be discussed in the following, will depend on different (and

sometimes independent) ranges of scales of turbulent motion and, hence, present different problems in determining approximations for ensemble averages.

2.3 The location of the cloud

The question of 'where the cloud is' at some time, t, following release at $t = 0$, is answered by the location of the centre-of-mass, $\langle x(t) \rangle$. We will consider the case of a large initial cloud where 'meandering', i.e., the movement of the cloud as a whole by large scale turbulent motion, is not an issue. This is found from the so-called 'one fluid particle' analysis (Batchelor 1949). That is, the initial cloud is made up of elemental fluid particles, which do not interfere with each other or change shape during their travel. Superposition of trajectories from all of the fluid particles from the initial cloud are then used to compile the probable arrival of a particle from the initial cloud at the location (within a small volume element centered on), $\boldsymbol{x}$, at time, t. We note that the differential equation governing the mean concentration (equation (2.4) with $n = 0$) is linear and, as such, admits a superposition of solutions. A weighting is used to reflect the initial cloud concentration when it is non-uniform and the number of particles located at a particular position, normalized by the conserved release mass, provides the mean concentration, $C(\boldsymbol{x},t)$, from which the centre-of-mass, $\langle x(t) \rangle$, is derived as

$$\langle \mathbf{x}(t) \rangle = Q^{-1} \int_{a.s.} \mathbf{x} C(\mathbf{x},t) dv \,. \tag{2.8}$$

Often symmetry in the turbulent flow structure will obviate the location of $\langle x(t) \rangle$. For example, in homogeneous turbulence, statistics are determined from the repeated release of one typical fluid particle irrespective of release position. In the case of a ground level release in the constant stress region of the neutral atmospheric boundary layer (typically

10-100 m above the ground), the statistical properties of the particles depend only on the friction velocity, u_*, and time, t, by the Lagrangian similarity analysis of Batchelor (1964). That is, the three components of the centre-of-mass are given by

$$\left.\begin{aligned} \langle y(t)\rangle &= 0, \\ \frac{d\langle z\rangle}{dt} &= bu_*, \\ \frac{d\langle x(t)\rangle}{dt} &= \frac{u_*}{k}\ln\left(\frac{c(z)}{z_o}\right), \end{aligned}\right\} \qquad (2.9)$$

where x is the streamwise, y is the lateral and z is the vertical component of the displacement vector; b and c are universal constants, which Batchelor estimated to be about 0.1 - 0.2 (see also Chatwin 1968); k is von Karman constant ($k = 0.4$), u_* is the friction velocity; and z_o is the roughness height.

A second special case is the flow within a lengthwise uniform conduit such as a pipe or open channel. Here, a marked fluid particle will sample all of the velocity variation over the flow cross-section (of area A) during its migration due to the cross-stream components of turbulent motion. After a sufficient period of time the particle will 'forget' its release position on the flow cross-section and move downstream with the flow discharge velocity $\langle x(t)\rangle = Ut$ where

$$U = A^{-1}\int_A u(y,z)dA. \qquad (2.10)$$

2.4 The size of the cloud

The next question to address in this (simplified) framework is "how big is the cloud"? The size of the cloud is measured by the spatial variance of the cloud. For the case of a cloud without meandering, as above, we consider the classical analysis of Taylor (1921) in isotropic turbulence, and the further analysis of Batchelor (1952) in this section. The analysis is readily generalized to shear flows, even with the inclusion of molecular diffusivity (Sullivan 2004).

A purely statistical treatment of resolving diffusion from a continuous source was first introduced by Taylor (1921). His discussion includes a demonstration that the usual laws of differentiation may be applied to the mean values of fluctuating variables and their products. If *X(t)* and $u'(t)$ are the Lagrangian displacement and velocity respectively of a typical particle, after time *t*; $\langle X^2 \rangle$, the ensemble average of the mean square values of *X(t)*, is found from

$$\frac{d\langle X^2 \rangle}{dt} = 2\langle X \frac{dX}{dt} \rangle = 2\langle Xu' \rangle = 2\int_0^t \langle u'(t)u'(t+\tau) \rangle d\tau \,. \tag{2.11}$$

For homogeneous and stationary turbulence, the average properties are uniform in space and steady in time. Hence, the velocity product may be replaced by $\langle u'^2 \rangle R(\tau)$, where

$$R(\tau) = \frac{\langle u'(t)u'(t+\tau) \rangle}{\langle u'^2 \rangle} \tag{2.12}$$

is the Lagrangian autocorrelation coefficient, which results in

$$\frac{d\langle X^2 \rangle}{dt} = 2\langle u'^2 \rangle \int_0^t R(\tau) d\tau \,, \tag{2.13}$$

and

$$\langle X^2 \rangle = 2\langle u'^2 \rangle \int_0^T \int_0^t R(\tau) d\tau dt \,. \tag{2.14}$$

Here $\langle X^2 \rangle^{1/2}$ would represent the standard deviation of spatial displacement of the particles at time, T. Hence, the mean square of the deviations of the particle is finally expressed in terms of the mean square velocity of the particle and the Lagrangian correlation coefficient between the velocity of the particle at time, t, and that at time, $t+\tau$. The correlation should be unity when $\tau = 0$, and is effectively zero for large τ. Hence,

$$\langle X^2 \rangle = \langle u'^2 \rangle T^2 \qquad \text{for} \quad \text{small } T \tag{2.15}$$

$$\langle X^2 \rangle = 2\left(\int_0^T R(\tau) d\tau \right) \langle u'^2 \rangle T \quad \text{for} \quad \text{large } T, \tag{2.16}$$

the integral in the bracket being the Lagrangian time scale, t_L.

Batchelor (1949) showed that for the diffusion in homogenous turbulence at short time, when the correlation coefficient becomes unity, particle velocity fluctuations of all frequencies contribute to the dispersion exactly as they do to the turbulent energy. At large time, the slower fluctuations (larger scales) progressively dominate the dispersion; in effect the high frequency components merely oscillate the position of the particle, whereas the low frequency components tend to displace it in a more sustained way. One can define an apparent diffusivity (K) at large time as one half the spatial variance growth rate (Pasquill 1974, pp. 126),

$$K(t)_x = \frac{1}{2}\frac{d\langle X^2\rangle}{dt} = \langle u'^2\rangle \int_0^t R(\tau)d\tau \,. \tag{2.17}$$

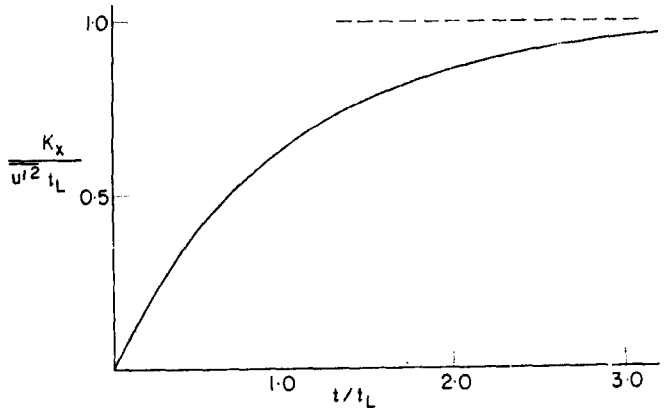

Figure 2.1: Apparent eddy diffusivity as per equation (2.17). [Adapted from Csanady (1973), pp. 63]

The value of K is initially zero, increases with time, at first approximately linearly and then more slowly, finally tending to the constant value of equation (2.17). This is shown in Figure 2.1. The observed spread of smoke plumes in the atmosphere over short distances show an increase in K with distance of travel. Sullivan and Yip (1985) showed that for a continuous source of contaminant, the time dependence was an important feature in describing dispersion in the natural atmospheric boundary layer where the use of even a spatially dependent 'eddy diffusivity' was inadequate.

The main feature here is that the largest scales of turbulent motion make the dominant contribution to the variance growth rate at all times. This is particularly relevant, for example, in finding average values in field experiments where the relevant length and time scales for averaging purposes are many times those scales in the flow. It

is also worth noting that the variance growth rate only becomes a constant (as in molecular diffusivity, where the constant is κ) when the integral over the Lagrangian autocorrelation function becomes constant.

The formulation can be readily generalized to shear flows such as the flow in a channel or pipe. Here, though, the Lagrangian particle displacement and velocities depend on release position. We consider the motion relative to an axis moving with the discharge velocity, i.e., the streamwise component $x'(t) = x(t) - Ut$ and $u'(t) = u(t) - U$. The direct contribution in the lateral and longitudinal direction due to fluctuating turbulent motions are comparable to $u_* d$, where d is the length scale of the cross-section, e.g., the diameter of a pipe. By far the largest contribution to variance growth rate is in the streamwise direction and comes from the interaction between the cross-stream mixing and the mean velocity gradient. That is, the longitudinal growth rate is reduced by cross-stream mixing from what would be the case if released particles continued to travel with the release mean velocity without lateral movement. Thus, neglecting the direct contribution from longitudinal fluctuating motions, for a particular release position on the cross section, we have

$$\frac{1}{2}\frac{d\langle x'(t)^2\rangle}{dt} = \int_0^t \langle u'(t)u'(t+\tau)\rangle d\tau . \tag{2.18}$$

After normalizing with the relevant mean velocity scale, U, and the turbulent cross-stream mixing time scale, d/u_*,

$$\frac{1}{2}\frac{d\langle x'(t)^2\rangle}{dt} = \frac{U^2 d}{u_*}\int_0^t \frac{\langle u'(t)u'(t+\tau)\rangle}{U^2} d\left(\frac{\tau u_*}{d}\right). \tag{2.19}$$

Following a long period of time from release, when the location of release is 'forgotten' and the particle has sampled the variation over the cross-section many times the integral converges to

$$\frac{1}{2}\frac{d\langle x'^2\rangle}{dt} \sim \frac{U^2 d}{u_*} = \frac{(Ud)^2}{u_* d}. \tag{2.20}$$

That is, the variance growth rate is given by the ratio of two diffusivities, the square of a diffusivity based on the mean velocity to the cross-stream diffusivity due to the fluctuating turbulent motion. An argument can be made based on an extension of the central limit theorem that displacements will have a Gaussian distribution about an axis moving with the discharge velocity. That is, for the concentration, integrated over the cross section, is

$$\tilde{C}(x,t) = \int_A C(x,t)dA, \tag{2.21}$$

$$\tilde{C}(x,t) = \frac{Q}{\sigma\sqrt{2\pi}} e^{-\frac{1}{2}\left(\frac{x-Ut}{\sigma}\right)^2}, \tag{2.22}$$

$$\frac{1}{2}\frac{d\sigma^2}{dt} = T_L \frac{U^2 d}{u_*}, \tag{2.23}$$

where T_L is the Lagrangian integral constant. One notes that when the typical marked fluid particles sample the viscous dominated region adjacent to the walls (or equivalent recirculating region around roughness elements applies for non-smooth walls), the motion is reduced and leading to a long upstream tail in $\tilde{C}(x,t)$, and also delays the approach to symmetrical Gaussian form for a long time (Dewey and Sullivan 1977).

In the special case of the neutral atmospheric boundary layer mentioned above, the Lagrangian similarity theory gives the components of the variance as (Batchelor 1964; Chatwin 1968)

$$\left.\begin{aligned} \langle (x(t)-\langle x(t)\rangle)^2\rangle &\propto u_*^2 t^2, \\ \langle y(t)^2\rangle &\propto u_*^2 t^2, \\ \langle (z(t)-\langle z(t)\rangle)^2\rangle &\propto u_*^2 t^2. \end{aligned}\right\} \qquad (2.24)$$

We now consider the case where scales of turbulent motion are large enough to transport the cloud in its entirety. This is graphically apparent with a meandering plume from a continuous release. Here, we are concerned with the probable location of the centre-of-mass of individual clouds and the distribution of concentration in the centre-of-mass reference frames. This is referred to as 'relative diffusion' in contrast to 'absolute diffusion' when displacements are referred to a fixed point or inertial reference frame system. The variance growth rate here is determined from a two fluid particle analysis in which the fluid particles comprising the initial cloud are taken two at a time over all possible pairs (Batchelor 1952). The separation between a typical pair of particles *y(t)* contributes to the variance as

$$\frac{1}{2}\frac{d\langle y(t)^2\rangle}{dt} = \int_0^t \langle v(t)v(t+\tau)\rangle d\tau, \qquad (2.25)$$

where, v*(t)*is the relative velocity of the two particles.

A very practical advantage in centre-of-mass coordinates is that at any time *t*, it is the length scales of turbulence that are of the size of particle separation that are

important. Scales that are much larger just move both particles together and do not contribute to their separation. Smaller scales just jiggle the particles about and are less effective in separating them than scales of the separation size. In absolute diffusion the largest scales are always the most important, whereas in relative diffusion and at small separations only small scales matter and taking averages are much less problematic.

Another big advantage in relative diffusion occurs for extremely high Reynolds numbers. The cascading process in turbulence suggests that large scale eddies that contain non-homogeneities such as information on container size, etc. interact with smaller scales and so on to the smallest scales of turbulence where energy is taken out of the system by viscosity. That is, the inertial terms pump energy down the system without redistribution, while the pressure term acts to make the turbulence structure isotropic. For a sufficiently high Reynolds number, there will be a range of scales between the large energy containing scales and the small dissipation scales – 'the inertial sub-range', that only depends on the energy transfer rate, i.e., the rate of energy dissipation per unit mass. On simple dimensional grounds Batchelor (1952) shows that if the contaminant cloud is in this range, then

$$\langle y^2 \rangle = \left(\frac{2}{3} \alpha t \right)^3 . \tag{2.26}$$

Richardson (1926) pointed out that relative dispersion is an accelerating process in which an initial marked volume of fluid is spread at a rate dependent upon its size and arrived at the '4/3 power law' for the relative diffusion as

$$\frac{1}{2} \frac{d\langle y^2 \rangle}{dt} = \alpha y^{4/3} \tag{2.27}$$

where $\alpha = c\varepsilon^{1/3}$; c is an universal constant of order one, and ε is the rate of energy dissipation. This was observed with floating particles over a range of 2 m to 2 km in the ocean (Richardson and Stommel 1948; Ozmidov 1957, 1960). It should be noted that generally, to get a substantial inertial sub-range (usually in the ocean and atmosphere), a very high Reynolds number is needed.

The relationship between the mean concentration distributions in absolute diffusion is derived from that in relative diffusion with a convolution integral. If we let $r(x',t)$ be the probable location of the centre-of-mass x' and $C'(y,t)$ the relative mean concentration, the mean concentration in absolute diffusion is (Munro et al. 2003)

$$C(x,t) = \int_{-\infty}^{\infty} r(x',t)C'(x-x',t)dx' . \tag{2.28}$$

One can note that the probability of the centre-of-mass location can be found from C and C' by using a Fourier Transform, for example. It may be equally compelling to combine the probable centre-of-mass location and cloud size from a relative framework and simply consider the location and size in an inertial framework.

2.5 The state of the cloud

The next issue to be addressed is the 'state of the cloud', or, in other words, the distribution of concentration values within it. For this, we introduce the Expected Mass Fraction (EMF) function defined as

$$q(\theta;t) = Q^{-1} \int_{a.s.} \theta p(\theta;x,t) d\mathbf{x}\,; \tag{2.29}$$

$$\int_0^\infty q(\theta;t) d\theta = 1\,, \tag{2.30}$$

where *a.s.* indicates an integral over all space (Sullivan and Ye 1997). This has the simple and straightforward interpretation that the expected fraction of the release mass, Q, that is between θ_a and θ_b is

$$\int_{\theta_a}^{\theta_b} q(\theta;t) d\theta\,. \tag{2.31}$$

The effect of molecular diffusivity, κ, to reduce concentration values is observed as the area under $q(\theta;t)$ shifts to lower values of θ as time increases. It is anticipated that few repeat releases of a cloud would be required to get an ensemble average approximation since all of the concentration values within the cloud are used at each compilation and the variations with location are integrated out. Because the spatial variation is integrated out one expects a more simple form of the EMF than would be observed of the PDFs throughout the cloud.

The moments of $q(\theta;t)$ are

$$M_n(t) = \int_0^{\theta_{max}} \theta^n q(\theta;t) d\theta\,. \tag{2.32}$$

These are simply related to the moments of the PDF, $p(\theta;\mathbf{x},t)$, as

$$M_n(t) = Q^{-1} \int_{a.s.} m_{n+1}(x,t) d\,\boldsymbol{x}\,. \tag{2.33}$$

It is to be noted that there is a maximum value of concentration, θ_{max}, which is the largest initial value of concentration that can never be exceeded. The evolution of the moments of the EMF is given by the relatively simple differential equation (Sullivan and Ye 1997),

$$\frac{\partial}{\partial t} M_n = -n(n+1)\kappa Q^{-1} \int_{a.s.} \langle \Gamma^{n-1}(x,t)(\nabla\Gamma(x,t))^2 \rangle dv . \tag{2.34}$$

The function $q(\theta;t)$ has not yet been directly measured. Approximations suggest that there is much less variation between realizations so that convergence is relatively fast. We also note that the EMF is the same for relative diffusion and absolute diffusion. Slightly modified versions of the EMF have been considered for fixed point measurements in plumes (Heagy and Sullivan 1996; Sullivan and Ye 1997).

A simple prescription of central moments, $\mu_n(x,t)$, of the PDF defined by

$$\mu_n(x,t) = \int_o^{\theta_{max}} (\theta - C)^n p(\theta;x,t) d\theta \tag{2.35}$$

was given in Chatwin and Sullivan (1990) and Sawford and Sullivan (1995). These have received a considerable amount of validation over a wide range of flows. Sawford and Sullivan (1995) also provided a generalized form of normalized moments for a non-uniform source concentration case by introducing additional parameters λ_n as:

$$\left.\begin{aligned} \frac{\mu_2}{(\alpha\beta C_o)^2} &= \hat{C}(1-\hat{C}) \\ \frac{\mu_3}{(\alpha\beta C_o)^3} &= \hat{C}(\lambda_3^2 - 3\hat{C} + 2\hat{C}^2) \\ \frac{\mu_4}{(\alpha\beta C_o)^4} &= \hat{C}(\lambda_4^3 - 4\lambda_3^2\hat{C} + 6\hat{C}^2 - 3\hat{C}^3), \\ &\vdots \end{aligned}\right\} \tag{2.36}$$

where, $\hat{C} = \frac{C}{\alpha C_o}$, and C_o is a local concentration scale (e.g., the maximum value). The parameters α, β and λ_n depend only on time in the case of sudden release or on distance downstream in the case of a steady release.

Higher normalized moments were derived by Mole and Clarke (1995) as

$$\begin{aligned} K_4 &= a_4 K_3^2 + b_4 \\ K_5 &= a_5 K_3^3 + b_5 K_3 , \\ &\vdots \end{aligned} \qquad (2.37)$$

where, $K_n = \frac{\mu_n(\mathbf{x},t)}{\mu_2^{n/2}(\mathbf{x},t)}$. These expressions have had widespread validation in both laboratory and field experiments. An important and significant feature is that these expressions can be validated with isolated fixed point measurements in the field. The connection between the coefficients that appear in equations (2.36) and (2.37) was shown in Schopflocher and Sullivan (2005) to be

$$\lambda_n^{n-1} = a_n \lambda_3^{2(n-2)} . \qquad (2.38)$$

It was also shown in Mole et al. (2008) that

$$\frac{a_n}{a_{n-1}} = \frac{n a_4 a_5}{(5n-20)a_4^2 - (4n-20)a_5} \qquad \text{for n = 6, 7... .} \qquad (2.39)$$

Schopflocher et al. (2007) used the relationships in (2.36), (2.37) and (2.38) to find the moments of the EMF, q, and it was found that the form of EMF should be a simple three parameter Beta function

$$q(\theta;\phi,\psi) = \frac{1}{B(\phi,\psi)\theta_{\max}} \left[\left(1 - \frac{\theta}{\theta_{\max}}\right)^{\psi-1} \left(\frac{\theta}{\theta_{\max}}\right)^{\phi-1} \right], \qquad (2.40)$$

where $B(\varphi,\psi)$ is defined in terms of a Gamma function, $G(\cdot)$, as

$$B(\varphi,\psi)=\frac{G(\varphi)G(\psi)}{G(\varphi+\psi)}\ . \tag{2.41}$$

It has a further advantage that the parameters are directly given in terms of the non-dimensional moments $\hat{M}_n = M_n/C_o^n$, where M_n are the moments of EMF. The solution is given in Schopflocher et al. (2007) as:

$$\begin{bmatrix} \hat{M}_2-\hat{M}_1^2 & -\hat{M}_1 \\ \hat{M}_3-\hat{M}_1\hat{M}_2 & -2\hat{M}_2 \end{bmatrix}\begin{bmatrix} z \\ \Theta \end{bmatrix}=\begin{bmatrix} -\hat{M}_2 \\ -2\hat{M}_3 \end{bmatrix}, \tag{2.42}$$

where $\phi=\hat{M}_1(z/\Theta)$, $\psi=\mathrm{z}-\phi$ and Θ is the maximum value of concentration normalized by C_o.

The idea of using a few lower order moments to represent the PDF (or the EMF) is appealing because of the relative ease of measurement and relative simplicity of the equations governing the moments. This procedure should provide a reasonable approximation for the bulk of the PDF but not necessarily perform well in the higher concentration tails.

2.6 High concentration tails

In order to concentrate on the high concentration tails of the PDF, we can break up the PDF in two parts and write moments. From extreme value theory, one can anticipate that the high concentration tails are given by the generalized Pareto density function (Mole et al. 2008),

$$g(\theta)=\frac{1}{a}\left(1-\frac{k\theta}{a}\right)^{1/k-1}, \tag{2.43}$$

where k and a are distribution parameters. This is valid for $0\le\theta\le\theta_{max}$, where $\theta_{max}=\frac{a}{k}<\theta_o$, θ_o being the source concentration. The parameter k determines the slope of $g(\theta)$ and it is greater than zero. This has been widely observed in field and laboratory measurements over a substantial range (about 60% on centreline and about 80% at one spatial variance away) of concentrations (Mole et al. 2008; Schopflocher 2001). The PDF of concentration is written as

$$p(\theta)=(1-\eta)f(\theta)+\eta g(\theta) \quad \text{for} \quad 0\le\theta\le\theta_{max}, \tag{2.44}$$

where $g(\theta)$ is the GPD and η is a positive constant. If it is assumed that at high concentration $f(\theta)$ is insignificant, then

$$p(\theta)\approx\eta g(\theta). \tag{2.45}$$

If we let θ_c be the concentration above which this is valid, then the probability that $\theta>\theta_c$ is approximately equal to D, where D is defined by

$$D=\eta\int_{\theta_c}^{\theta_{max}} g(\theta)d\theta=\eta\left(1-\frac{\theta_c}{\theta_{max}}\right)^{1/k}. \tag{2.46}$$

The absolute moments, m_n are

$$\begin{aligned} m_n &= (1-\eta)\int_0^{\theta_{max}}\theta^n f(\theta)d\theta+\eta\int_0^{\theta_{max}}\theta^n g(\theta)d\theta \\ &\approx (1-\eta)\int_0^{\theta_c}\theta^n f(\theta)d\theta+\eta\int_0^{\theta_{max}}\theta^n g(\theta)d\theta. \end{aligned} \tag{2.47}$$

For a sufficiently large n the contribution from $f(\theta)$ will be small compared with that from $g(\theta)$; thus,

$$m_n \approx \eta \int_0^{\theta_{max}} \theta^n g(\theta) d\theta . \tag{2.48}$$

With parameters a and k, $g(\theta)$ can be written as

$$\int_0^{\theta_{max}} \theta^n g(\theta) d\theta = \frac{n! a^n}{(1+k)(1+2k)...(1+nk)} . \tag{2.49}$$

Thus, for sufficiently large n,

$$\frac{m_{n-1}}{m_n} \approx \frac{1+nk}{na} = \frac{1}{a}\left(\frac{1}{n}\right) + \frac{k}{a} . \tag{2.50}$$

Therefore, at higher n, it is expected that the ratio of successive moments is a linear function of $1/n$ and one can find the parameters of the Pareto tail and, in particular, the $\theta_{max} = a/k$. It is to be noted that the problems at low concentration values due to the noise were avoided in the above approach (Lewis and Chatwin 1995). In the discussion of the paper by Mole et al. (2008), it was shown that the parameters and maximum concentration did not vary much over a plume cross section.

From the result and observation on the parameters we expect that the high concentration range of the EMF will be

$$q(\theta) \sim Q^{-1} \int_{a.s.} \theta \cdot \eta \frac{1}{a}\left(1 - \frac{k\theta}{a}\right)^{1/k - 1} d\mathbf{x} = \frac{\theta}{a}\left(1 - \frac{k\theta}{a}\right)^{1/k - 1} Q^{-1} \cdot \int_{a.s.} \eta \, d\mathbf{x} . \tag{2.51}$$

2.7 Moment closure approximations

From the discussion above, it would appear that one can use low order moments to approximate $q(\theta,t)$ and, in particular, to investigate the high concentration tail. To solve the moment equations, one would require two closure approximations; one for the

convective terms and the other for the dissipative terms. A convective closure approximation was made by Sullivan (2004) as

$$\nabla \cdot \langle u' \Gamma^{n+1} \rangle = -\theta_o^n \frac{\partial C}{\partial t}. \tag{2.52}$$

Here, the convective term was approximated without regard to molecular diffusion. A modified version of the convective closure approximation is proposed here for taking into account the effect of molecular diffusion by replacing the source concentration, θ_o, with a representative local concentration scale, θ_o^*.

We consider an axisymmetric plume and cylindrical coordinates for a continuous, steady point-source to test the convective approximation, which is

$$\nabla \cdot \langle u' \Gamma^{n+1} \rangle = \frac{1}{R} \frac{\partial \langle u_r R \Gamma^{n+1} \rangle}{\partial R} + \frac{1}{R} \frac{\partial \langle u_\theta \Gamma^{n+1} \rangle}{\partial \theta} + \frac{\partial \langle u_x \Gamma^{n+1} \rangle}{\partial x}. \tag{2.53}$$

On the right hand side the term $\frac{1}{R} \frac{\partial \langle u_\theta \Gamma^{n+1} \rangle}{\partial \theta} = 0$. Therefore, the approximation for an axisymmetric case using the convective closure is

$$-\frac{\partial C}{\partial x} \propto \frac{1}{U(\theta_o^*)^n} \left[\frac{\partial}{\partial x} \left(\langle u' \Gamma^{n+1} \rangle \right) + \frac{1}{y} \frac{\partial}{\partial y} \left(y \langle v' \Gamma^{n+1} \rangle \right) \right]. \tag{2}$$

A two dimensional plume created by a line source is also considered and the convective closure approximation is

$$-\frac{\partial C}{\partial x} \propto \frac{1}{U(\theta_o^*)^n} \left[\frac{\partial}{\partial x} \left(\langle u' \Gamma^{n+1} \rangle \right) + \frac{\partial}{\partial y} \left(\langle v' \Gamma^{n+1} \rangle \right) \right]. \tag{2.55}$$

These approximations need to be validated experimentally using simultaneous measurements of velocity and concentration fields.

A dissipative closure approximation was made in Moseley (1991) with some confirmation given in Mole (1995):

$$(\nabla\Gamma)^2 = \frac{B(\Gamma - \Gamma_t)^2}{\eta_B^{\,2}}, \tag{2.56}$$

where η_B is the conduction cut off length, B is a proportionality constant and Γ_t is a threshold concentration (which is set to be zero). The solution of the dissipative approximation for plumes behind both the line source and the point source can be written as

$$\langle\Gamma^{n-1}\left(\frac{\partial\Gamma}{\partial x}\right)^2\rangle + \langle\Gamma^{n-1}\left(\frac{\partial\Gamma}{\partial y}\right)^2\rangle + \langle\Gamma^{n-1}\left(\frac{\partial\Gamma}{\partial z}\right)^2\rangle = \frac{B}{\eta_B^{\,2}}\langle\Gamma^{n+1}\rangle \ . \tag{2.57}$$

The third term on the left hand side can be approximated to be the same as the other two terms.

The moment equation with these two approximations (with $\Gamma_t = 0$) becomes,

$$\frac{\partial m_{n+1}}{\partial\tau} + n(n+1)m_{n+1} = \theta_o^n\frac{\partial C}{\partial\tau}, \tag{2.58}$$

where, $\tau = \kappa B\, t/\eta_B^{\,2}$. The solution for a line source, where η_B is assumed to be constant throughout the flow, is

$$m_{n+1}(x,\tau) = \theta_o^n C(x,\tau) - n(n+1)\theta_o^n e^{-n(n+1)\tau}\int_o^\tau C(x,z)e^{n(n+1)z}dz\,. \tag{2.59}$$

Sullivan (2004) has shown that these closures lead to a good qualitative comparison with the measurements in the plume from a line source in grid turbulence for the distributed four lowest order central moments. To proceed further one needs a direct assessment of the relationships given in the closure approximations.

2.8 Self-similarity in the scalar field

An important aspect of passive scalar transport in turbulent flows is the fractal geometry of interfaces. Turbulent mixing and transport of passive scalars can be described as a combination of folding and wrinkling processes (Catrakis 2000). The effect of these processes can be studied by quantifying the geometric scale distributions of the convoluted structure of passive scalar interfaces within the fluid. The broader objective for this study is to utilize the concept of fractals or self-similarity of the passive scalar in a turbulent flow in dealing with under-resolved (experimental resolution is coarser than the Batchelor scale) dissipation calculation from the measurements.

From the smallest particle in nature to a cluster of galaxies, there has been a nested hierarchical organization in structures, which is known as fractal structure (Oldershaw 1989). For last few decades there has been a growing interest in the fractal properties of nature's geometry that was largely inspired by Mandelbrot (1983). However, the idea of self-similarity and fractal characteristics was first introduced by Richardson (1922). Fractal structures usually involve self-similarity, a form of invariance with respect to shifts in scale, in which small parts of a structure have similar geometrical properties as the larger parts of the structure (Oldershaw 1989). This is a key principle in the development of the similarity hypothesis for passive scalars in turbulent flow fields.

In the modern era of turbulence research, an emphasis has been given to the small-scale structure and the fractal geometry of turbulent passive scalar fields that is

built on several amendments to Kolmogorov's hypothesis. The phenomenological model of the small-scale passive scalar, introduced by Obukhov (1949) and Corrsin (1951), was based on similarity arguments. According to them, there exists an inertial range where the turbulent structure of the passive scalar field is independent of the large scales. This length scale is know as Obukhov-Corrsin length scale, $\eta_{oc} = (\kappa^3/\varepsilon)^{1/4}$. Later, Batchelor (1959) showed that the Obukhov-Corrsin cutoff length scale was appropriate only for low Schmidt number passive scalars ($Sc = \nu/\kappa << 1$) and that the strain rate of the fluctuating velocity determines the cutoff length scale for scalars with higher Schmidt numbers (Sc >> 1). This is called the Batchelor scale ($\eta_B = (\nu\kappa^2/\varepsilon)^{1/4}$).

Passive scalars in turbulent flows are rapidly stretched into thin sheet-like structures by the turbulent convective motion. The geometry of the interfacial surface has significant practical importance in a number of applications. In non-reactive mixing processes, the molecular diffusive flux occurs across concentration gradients at interfaces (Schumacher and Sreenivasan 2005). Estimating the resulting mixing is necessary for predicting the dilution of the pollutants into the atmosphere or the discharge of wastewater into a stream. Molecular diffusion happens within the smallest scales (η_B), where the concentration gradients are the highest. Sreenivasan (1991) argued that at a high Schmidt number, the convolutions of the scalar interface are space filling on scale between the Kolmogorov scale ($\eta = (\kappa^3/\varepsilon)^{1/4}$) and the Batchelor scale (η_B). The surface of the scalar, where diffusion happens, possesses fractal scaling (Sreenivasan 1991).

The concept of fractal scaling inspired us in dealing with the under-resolved (i.e., the experimental resolution is larger than the Batchelor scale) dissipation calculation in the context of this study. Prior to broadening the discussion dealing with the under-resolved dissipation calculation, it is important to understand the concept of fractals. To determine the fractal dimension of a scalar interface (i.e., scalar/non-scalar interface), one covers the space by boxes of fixed size and counts in each case the number of boxes that contain the scalar interface. If the number of boxes shows a power-law dependence on box size, the exponent characterizing the power-law is called the fractal dimension of the scalar interface (San Gil 2000). At higher Reynolds number, several scaling regimes may exist for a high Schmidt number passive scalar (Dasi 2004). The inertial-convective regime ($\eta <$ *length scale(r)* $< L$) is defined as the range with negligible effects of large-scale anisotropies, viscosity and diffusivity. In the viscous-convective regime ($\eta_B < r < \eta$) viscous effects start to play a role while molecular diffusivity does not. The scale range between the integral scale (L) and η will be called the K-zone, and the scale range between η and η_B and will be called the B-zone. The scalings are quite different for these two ranges. According to Prasad and Sreenivasan (1989) the fractal dimension of the K-zone is 2.36 and independent of flow configuration as long as the flow is fully turbulent. For large Schmidt numbers the dimension of the B-zone is 2.7. However, the scaling in the K-range is expected to be affected by the cut-off scales in particular by Reynolds number (Menevau and Sreenivasan 1990), and the mean shear flow (Sreenivasan and Dhruva 1998). The studies by Sreenivasan and Dhruva (1998), and Sreenivasan et al (1999) pointed out that the shear affects the quality of scaling by introducing a curvature type fractal data, which was greatly reduced by removing shear. Frederiksen et al. (1996,

1997) showed that a constant fractal dimension exists for the *B*-zone; however, the dimension depends on length scales larger than the Kolmogorov scale. Dasi et al. (2007) summarized experimental studies of the geometric properties of passive scalar interfaces and argued that large-scale anisotropy masks the constant fractal dimension, even if it exists.

Sreenivasan et al. (1989) argued that the large scale structure of the turbulence determines the precise amount of mixing; however, it is eventually the diffusive action at the molecular level that performs the actually mixing. Thus, the dynamics of turbulence transmit fractal-like properties to surfaces and the result is a large increase in surface area. The diffusive flux across these surfaces follows Fick's law of diffusion (Sreenivasan 1991). Sreenivasan et al. (1989) argued that the gradients across the scalar interface are of order $\Delta\Gamma/\eta_B$ for unit Schmidt number, where $\Delta\Gamma$ is the concentration difference at the interface. Sreenivasan (1991) developed a relation (equation (3.4) in his paper) between the surface area and the resolution of measurement with high Schmidt number scalars. The estimate of the gradients for flux across scalar interface is of order $\Delta\Gamma/\eta_B$, which shows Reynolds number similarity and Schmidt number similarity in the *K*-zone and the *B*-zone, respectively. The convolutions in the *K*-zone are self-similar but those in the *B*-zone are much more pronounced, where they essentially fill the space and render the effective thickness of the interface of order η for high Schmidt numbers. The physical picture that was depicted in Sreenivasan (1991), is shown here as Figure 2.2.

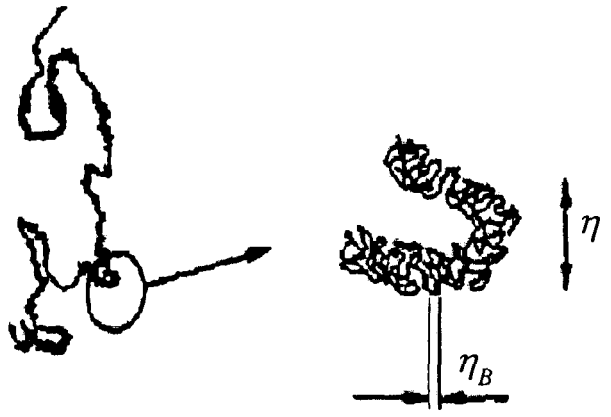

Figure 2.2: Schematic of the scalar interface when the Batchelor scale is resolved. (From Sreenivasan 1991)

This concept of fractal scaling shed light on dealing with the under-resolved dissipation calculation from the experiments, and will be utilized in § 4.4.

2.9 Summary

We have set out a new framework in terms of the answers to the following questions: where is a contaminant cloud? how big is it? and what is its state? The first two questions are determined from a "one particle" analysis (and possibly "two particle" analysis if one were to use a relative diffusion). These two questions do not depend on molecular diffusion or reduction of concentration values. Much has been done in the literature on the mean concentration field (Sullivan and Yip, 1985; Pope, 1998). In contrast, our focus in this study is on the 'state of the cloud'. That is, the reduction of the concentration values which only takes place due to molecular diffusion. The objectives of this study are to measure for the first time the Expected Mass Fraction (*EMF*) function and to assess the approximation given for closures as well as validate the other expressions where possible and as necessary along the way.

Chapter 3: Experimental Setup and Measurement Techniques

3.1 Introduction

To meet the objectives of the study, the scalar and velocity fields were measured downstream of a continuous release of a high Schmidt number passive scalar (Rhodamine 6G) into a uniform flow with grid turbulence. High-resolution measurements of the scalar and velocity fields were conducted in a centreline vertical plane parallel to the flow using Planar Laser Induced Fluorescence (PLIF) and Particle Image Velocimetry (PIV), respectively. This chapter provides an overview of the experimental apparatus, experiment procedures, and data processing methods. In addition, the experimental parameters and flow characteristics are described.

3.2 Flow facility – the water tunnel

A new water tunnel in the Boundary Layer Wind Tunnel Laboratory (BLWTL) at the University of Western Ontario has been built to broaden the scope and capabilities of experimental research relevant to fundamental and industrial problems such as the dispersion of contaminants in air and water. In this chapter a brief description of the water tunnel is presented.

Figure 3.1 shows an overview of the water tunnel, which consists of an inlet reservoir, where the water is introduced into the tunnel, followed by a settling chamber consisting of a honeycomb and screens, an 8:1 contraction, the test section and a 90 degree turn to return the water to the sump through a control valve. The total volume of

the underground sump is 36 m^3. The pump capacity is 0.063 m^3/s and the present set-up allows a maximum flow rate of 0.036 m^3/s, corresponding to a maximum average bulk velocity of 0.20 m/s. The water tunnel was designed to satisfy the criteria of a uniform mean velocity profile within 1% and turbulence intensity of less than 1% in the test section. Optical access was given a high priority so that the four walls of the test section are made of tempered glass. Details of the components follow below.

A 30 hp sump pump was chosen to generate the necessary head for the desired range of flow rates. The pump has 4 blades and a 166 mm diameter impeller and runs with a shaft speed of 3560 rpm. The power of the pump was over-designed to allow for expanded future scope. The pump supplies water through a 150 mm diameter piping system with five elbows. For distributing the flow of water through the piping system into the inlet reservoir uniformly, a manifold with a total of eight 50 mm diameter vertical pipes, each with 13 mm diameter holes in them, was placed in the inlet reservoir. Those small holes were placed at a centre-to-centre distance of 105 mm. The length of each of the vertical pipes is 1500 mm and they are separated by 250 mm centre-to-centre.

The inlet reservoir (2440 mm x 2030 mm x 3050 mm), constructed of stainless steel, was sized to reduce the turbulence generated from the incoming water through the pipe. To remove any bubbles from the flow, a 'sandwich' of 10 layers of fiberglass screen (each 34% solid) with a wire diameter 0.28 mm is placed in the middle of the inlet reservoir. To maintain a constant head in the tank, an overflow pipe is placed at a particular height, which drains excess supply water back directly to the underground

sump. In the reservoir, waves of about 10 mm height were observed on the water surface while running the tunnel but this has little effect on the steadiness in the test section, a point which is examined further below.

The lateral components of mean velocity and of the larger turbulent eddies can be reduced effectively by a honeycomb. Mehta and Bradshaw (1979) suggested that the cell length should be about 6 - 8 times its diameter for maximum benefit and the cell size should be smaller than the lateral wavelength of the velocity variation. The usual shapes of the honeycomb cell are hexagonal, square and triangular. Aluminum honeycombs are widely used in wind and water tunnels, as was the case here, where a 12.7 mm square, 100 mm long, honeycomb was installed at the settling chamber outlet.

Mehta (1985) carried out an experimental investigation on the effects of different types of screens on turbulent flow. A screen, or another uniform hydrodynamic resistance in a constant-area passage, experiences a drag force and, therefore, reduces the total pressure of the flow passing through it without altering the average velocity. In this case, velocity variations will be reduced as well since the drag force would be greater in regions where the velocity is higher than average, thus, tending to equalize the total pressure over the cross-section (Mehta 1985). A screen will, in principle, reduce the velocity defect in a turbulent boundary layer that passes through it. Several expressions have been derived over the years for the pressure drop coefficient of a screen, K; many of them were based on data from screens with open-area ratios, $\chi < 0.5$, where χ is defined

as $\chi = \left(1 - d/l\right)^2$, d is the screen wire diameter and l is screen mesh length. Weighardt's (1953) formulation for the prediction of the pressure drop coefficient

$$K = 6.5\left[\frac{1-\chi}{\chi^2}\right]\mathrm{Re}^{-1/3}, \tag{3.1}$$

where $$\mathrm{Re} = \frac{Ud}{\chi\nu}, \tag{3.2}$$

has been found to be accurate over a wide range of velocities ($0 < U < 20$ m/s; Mehta 1984). For screens with lower open-area ratios, the jets coming through the open areas coalesce into irregular patterns by mutual entrainment and actually produce flow non-uniformities of their own (Mehta 1985). Therefore, it has been suggested to use screens of open-area ratio of greater that 0.58. Screens reduce the longitudinal components of turbulence or mean velocity variation to a greater extent than the lateral components, so that the number of screens to be used is determined by the acceptable lateral component disturbance in the test section. For the pressure drops through the screens to be completely independent, the spacing should be such that the static pressure has fully recovered from the perturbation before reaching the next screen. For full benefit, from the turbulence reduction point of view, the minimum spacing should be of the order of the large energy containing eddies. It has been suggested that a screen combination with spacing equivalent to about 0.20 settling tank/chamber diameters performs successfully (Mehta and Bradshaw 1979). The optimum distance between the last screen and the contraction entry has also been found to be about 0.20 cross-section diameters. If this distance is much shorter, significant distortion of the flow through the last screen may be expected. On the other hand, if this distance is too long then unnecessary boundary layer growth may occur. In the design of the water tunnel, three screens were placed

downstream of a honeycomb. The spacing between the screens is $0.21\sqrt{A}$, where A is the cross-sectional area of the settling chamber. The square 11 Mesh screens are made of stainless steel with a wire diameter of 0.48 mm and an open-area ratio of 0.62. The distance between the last screen and the entry of the contraction is $0.161\sqrt{A}$.

The purpose of a contraction is to reduce the relative variations in velocity over the cross section by increasing velocity without altering the total pressure. A well designed contraction produces a uniform and steady stream at its outlet and avoids flow separations. It is possible to avoid separation in the contraction by making it very long, however this results in an increase of the tunnel length, cost and exit boundary layer thickness. A large contraction ratio is always advantageous; however, it also means higher construction and operating costs in addition to possible problems of noise and separation near the ends. Therefore, contraction ratios between 6 and 10 are normally used for small tunnels (Bell and Mehta 1989). A contraction ratio of 8, with a length of 1120 mm, has been used for the current water tunnel. The contraction of the low turbulence wind tunnel at the University of Toronto (e.g., Kopp and Keffer 1996) was followed in the current design.

The test section of the water tunnel is built out of 12.7 mm thick tempered glass held together using silicone. The length of the test section was chosen to be 10 times the height of the test section in order to allow for the study of developing turbulence. The width, *w*, and height, *h*, of the test section are 600 mm and 300 mm, respectively, while the length is 3000 mm. Three 150 mm diameter openings were placed near the beginning

of the test section on three sides (one on the top plate and two on the side plates). A manual valve is installed at the end of the curved section to control the flow rate. A discussion on performance of the water tunnel is presented in § 3.5.

3.3 The grid and plume delivery system

A square mesh grid formed of 6.35 mm diameter bars spaced at 25.4 mm in the water tunnel was used to create turbulence. The grid provides a mesh Reynolds number of 5000 with the maximum flow velocity of 0.2 m/s. The plume delivery system includes a 6.25 mm inner diameter nozzle as a point source located 100 mm downstream of the grid and a series of 3 mm diameter holes with 25.4 mm spacing on a lateral stainless steel tube of 6.25 mm diameter as a line source (see Figures 3.3.) attached to the grid. The nozzle is aligned with the centreline of the water tunnel and pointed in the downstream direction of the flow. A plume generator (Figure 3.4) is designed to maintain a steady flow rate of the tracer dye solution through the nozzle. A plume generator is set at the same height of the water level in the settling tank of the water tunnel in order to achieve a static pressure (i.e., static head) at the nozzle exit similar to the centre of the test section of the water tunnel (assuming negligible losses). The plume generator is designed to be airtight and the only opening to pass air through is a glass tube inserted into the cylindrical container. Another glass tube is inserted into the container, which is connected to the nozzle with a plastic tubing system and a control valve. The height difference between the lower ends of the two glass tubes generates the head necessary (i.e., driving head) to achieve a constant plume exit velocity, which is the same as the free stream velocity of the test section. In the experiments with the point source the driving head is

set at such a level that the plume generator would create a steady flow rate of 4.6 cm^3/sec to approach the free stream velocity (0.2 m/s) at the nozzle exit. Figure 3.5(a) shows the velocity profiles at a distance 5 mm downstream of the nozzle exit relative to the centreline exit velocity (U_o) measured by PIV and LDV (to be discussed in the following sections). A wake region is developed behind the nozzle exit; however, the wake disappears further downstream, which is shown in Figure 3.5(b) where velocities are normalized by the free stream velocity, U_{ref}.

3.4 Measurement techniques

In the present study, three laser-based measurement techniques were employed. A Laser Doppler Velocimetry (LDV) was used to characterize the flow in the water tunnel. PIV and PLIF were used to measure simultaneous velocity and concentration fields, respectively. Brief descriptions of these measurement techniques are presented here.

3.4.1 Laser Doppler Velocimetry

Point velocity data were obtained using a single component TSI Inc. laser Doppler velocimetry (LDV) system in back-scatter mode. The transmitting lens had a focal length of 350 mm in air, resulting in a measuring volume diameter and length of 0.046 mm and 1.2 mm, respectively. A two-axis motor-driven traversing unit was used to move the LDV probe in two directions, with a relative position accuracy (precision) of 0.015mm per 100mm of travel and a minimum displacement of 0.0025mm per step. The flow was seeded using Silicon Carbide particles with an average diameter of 2 μm and a density of 3200 kg/m^3. The accuracy of the velocity measurements depends on the

capability of the particles to follow the instantaneous motion of the medium. An analysis is presented in Appendix C (§ C1) to justify that for Silicon Carbide.

3.4.2 Particle Image Velocimetry

Particle image velocimetry (PIV) is a non-intrusive technique for measuring complex flow fields in a two dimensional plane providing two components of the velocity vector with high spatial resolution. In PIV measurements, two consecutive images are obtained to capture the light scattered by tracer particles from the laser pulses whose timing is precisely controlled. Two dimensional cross-correlations of a small interrogation area of the corresponding two images are obtained to deduce the displacement of particles in the interrogation areas. Raffel et al. (1998) describe the technique in detail.

The PIV system used for the current study makes use of a double pulse Nd:YAG laser operating at 15 Hz with energy of 120 mJ/pulse that produces a sheet of light at a wavelength of 532 nm illuminating the flow field which is seeded with the same particles that were used for the LDV measurements. The scattered light from the particles is collected into a CCD camera located 90 degrees to the light sheet. The CCD has an array of 1600 x 1200 pixels with a 12 bit dynamic range operating in double exposure mode. The images are then subsequently transferred to a computer, equipped with TSI Insight3G® software (TSI Inc. 2008), for the completion of a two frame cross-correlation analysis.

3.4.3 Planar Laser Induced Fluorescence

Planar laser induced fluorescence (PLIF) is a non-intrusive technique for measuring the spatial scalar concentration field in continuous flow. The underlying physical principle of this technique is based on the absorption and subsequent reemission of photons by fluorescent dye tracers. This allows one, to detect very small changes in the concentration very accurately. In order to measure the fluorescence signal, the emitted light has to be filtered to avoid signal contamination. Rhodamine 6G has a peak absorption at 530 nm wavelength and a peak emission around 560 nm wavelength (Arcoumanis et al. 1990). The concentration field in the laser sheet thus appeared as yellow-orange light. Recording the instantaneous intensity field with TSI Insight3G® software (TSI Inc. 2008) yielded the instantaneous concentration fields. The calibration of PLIF images is presented in § 3.6.

Figure 3.2a represents the schematic view of the experimental set up, where positions of the laser, grid, source, and also the coordinates are depicted. The origin of the coordinates is considered at the centre of the tunnel cross-section at the inlet of the test section. A typical experimental setup in order to measure simultaneous velocity and concentration using PIV and PLIF, respectively, is shown in Figure 3.2b, where the top view of the tunnel and the relative positions of the two CCD cameras are shown. An optical low-pass filter was places in front of the lens of the PLIF camera, which filters wavelengths smaller than 550 nm.

3.5 Hydrodynamic performance of the water tunnel

The hydrodynamic performance of a water tunnel can be characterized by its temporal stability, spatial uniformity and the turbulence properties in the test section. The temporal stability of the mean flow was measured at a flow velocity of 0.20 m/s. The results for a 4 hour long run are presented in Figure 3.6, where normalized centreline velocities at a location of x/h = 1.7 downstream of the inlet are shown. Each point in the time series is an average of 120 seconds of data at a sampling rate of about 200 Hz. As can be seen, the temporal variation of tunnel velocity is less than ±0.50%. Most of the measurement points were also clustered in a row within the 95% confidence level of the LDV uncertainty. Those few points, outside of the confidence level, were the result of the drifting of the tunnel.

Velocity non-uniformity in a cross-sectional plane across the tunnel is also an important measure of performance. A total number of 195 measurement positions were used at x/h = 2.33, as shown in Figure 3.7(a), to generate a velocity contour across the tunnel cross-section. However, for other cross-sectional profiles, 104 measuring points were used over 1/2 of the cross-section of the tunnel. Assuming a symmetrical velocity distribution on the other half cross-section of the tunnel, it has been calculated that the working sections (where the velocity variation is within ± 1%) were found to be approximately 85%, 75%, 65% and 55% of the cross section of the tunnel at distances of x/h = 0.33, 1.67, 5.33 and 7.67 downstream of the inlet of the test section, respectively. These are not shown here for brevity. Contour plots of the relative velocity of the tunnel cross-section at x/h = 2.33 are presented in Figure 3.7(b). The speed-up in the upper left

hand corner of the plot was due to a persistent air bubble on the upper surface of the water tunnel during those measurements. Since such bubbles are occasionally found in the test section, we made the choice to obtain the data there to determine the effects. The maximum speed-up was approximately 1%, which is deemed to be relatively minor within the overall performance of the tunnel.

Figure 3.8 shows the streamwise velocity profiles at different locations in the test section. One can note that the centreline velocity increases as the distance from the inlet increases due to the increasing thickness of the wall boundary layers. This can be more clearly seen in Figure 3.9, where only centreline longitudinal velocities at different downstream locations are plotted for a nominal free stream (inlet) velocity of 0.20 m/s where the increase in speed is observed to be about 8% up to $x/h \sim 8$. Figure 3.7 also shows clearly the increase in the thickness of the boundary layer for larger longitudinal distances from the inlet.

One of the most important measurements is the turbulence intensity in the test section. For a low value of turbulence intensity, careful management of the flow using a honeycomb and screens is required as well as a large area ratio for the contraction (Lumley and McMahon 1967; Robins 1978). The turbulence intensities within the test section were found to be uniform except near the boundary layers on the walls. LDV cannot reliably measure turbulence intensities less than 1% because of the uncertainty introduced by the inherent instability of the Bragg cell oscillator. To overcome this problem, hot film anemometry measurements were carried out in the empty water tunnel

and the measured turbulence intensity was found to be just less than 0.50% on the centreline of the tunnel at $x/h = 0.5$. Figure 3.10 shows the power spectral density of the streamwise velocity fluctuations obtained from the hot film measurements. The data were collected at a sampling rate of 2000 Hz and were low-pass filtered with a cutoff frequency of 50 Hz. This shows no governing frequency in the empty tunnel flow.

Figure 3.11 shows the longitudinal variation of the mean vertical component of the velocity on the centreline, relative to the average streamwise centreline velocity. Since the maximum variation is about 0.60% of the average streamwise velocity, the vertical component is essentially negligible.

Figure 3.12(a) shows mean streamwise velocity profiles at different locations downstream of the grid. Turbulence intensities are presented in Figures 3.12(b) - (c) for different downstream locations along the lines where $z/w = 0$ and $y/h = 0$, respectively. The turbulence intensity along the centreline of the tunnel cross-section varies from ~12% to 1.2%, decaying with distance from the grid, as expected. This rate of decay will be examined in further detail below, but it is clear from Figure 3.12 that the uniformity of the grid turbulence is as good as the empty tunnel (no turbulence producing grid at the inlet of the test section).

Figure 3.13 compares the mean streamwise velocity profiles measured with LDV and PIV systems at a distance of $x/M = 19.69$ ($x/h = 1.67$) downstream of the grid. In this figure, the streamwise velocities are normalized by the reference velocity at a distance 50

mm away from the walls, for both cases. These data show that the match between the two methods is satisfactory. One can note that the PIV data also shows the speed-up of the velocity close to the walls. The horizontal bars are one standard deviation of the LDV measurements.

In homogeneous turbulence the average properties of the random motion are independent of position in the fluid (Batchelor 1953). A good approximation to homogeneous turbulence can be achieved in wind or water tunnel experiments by passing a uniform stream through a grid. This homogeneous turbulence decays with distance from the grid, since there is no production due to the absence of mean velocity gradients (Pope 2000). Figure 3.14 shows measurements of $\langle u'^2 \rangle$ downstream of a grid, performed in the water tunnel. It is evident that the normal stress, $\langle u'^2 \rangle$, decays as

$$\frac{\langle u'^2 \rangle}{U^2} = G\left(\frac{x}{M}\right)^{-n}, \tag{3.3}$$

where M is the mesh size (i.e., 25.4 mm). The value of the decay exponent, n, is found to be 1.33 in the current experiment. Previous studies reported the values of the decay component between 1.15 and 1.45, with the best value for most experiments being about 1.3 (Mohamed and LaRue 1990). The value of G (~ 0.07 for the present study) varies widely depending on the geometry of the grid and the Reynolds number (Pope 2000).

Due to the fact that the flow velocity is sampled in time by random passages of the tracer particles through the measurement volume of the LDV, velocity information is available in unequally spaced data points over the time span. Therefore, the usual

methods for estimating the spectral content of signals using equally spaced data points are not applicable here. A number of different methods have been proposed for computing the Power Spectral Density (*PSD*) from LDV measurements, which were reviewed by Benedict et al. (2000). The methods based on the reconstruction of the time series have widely been used for calculating uniformly sampled time series. The most straightforward technique is the zero order interpolation between the unevenly spaced samples and subsequent re-sampling of the interpolated process to give a uniformly sampled process (Simon and Fitzpatrick 2004). Another technique of the reconstruction of the time series is the sample-and-hold technique, which reconstructs the time series by holding the value of each validated data point until the next arrival and re-sampling the data at equal intervals. Other approaches to time series reconstruction are exponential interpolation by Host-Madsen and Caspersen (1995), auto-regressive techniques by Veynante and Candel (1988), Kalmen reconstruction (Banning 1997), higher order interpolation methods and fractal reconstruction. These techniques have been reviewed by Tropea (1995) for spectrum estimation from LDV time series. For the current study, the linear interpolation method has been implemented for generating uniformly spaced time series.

The power spectral density of streamwise velocity fluctuations are presented in Figures 3.15 for time series measured on the centreline of the tunnel at $x/M = 3.94$ ($x/h = 0.33$) and $x/M = 27.56$ ($x/h = 2.33$). The average data rate was greater than 500 Hz. The time series was reconstructed using the linear interpolation method, with a re-sampling rate of 500 Hz. Following this, the data were low-pass filtered with a cutoff frequency of

125 Hz. The spectra depicted in Figures 3.15 were obtained from averaging ten, 30 sec blocks of data.

The power spectral density is plotted in the non-dimensional form $F(f)U/2\pi L_x u'^2$ versus the non-dimensional frequency, $2\pi f L_x/U$, where, $L_x = \left(U/u'^2\right)\int_0^\infty \langle u'(t)u'(t+\tau)\rangle d\tau$ is the integral scale. The results in Figures 3.14 are compared with von Kármán's spectrum,

$$F(f)U/\left(2\pi L_x u'^2\right) = (2/\pi)\left\{1+1.8(2\pi f L_x/U)^2\right\}^{-5/6} \tag{3.4}$$

(Hinze 1959). Since power spectra of grid turbulence tend to have well defined shapes, it follows that the streamwise component of turbulence produced by grids can be described by a single velocity scale (u') and a single length scale (L_x), which have been incorporated in von Kármán's spectrum (Bearman and Morel 1983). The current measured spectra match well with the von Kármán spectrum for both the near grid and equilibrium regions.

The Taylor microscales ($\lambda=\sqrt{\{<u'^2>/<(du'/dx)^2>\}}$) at different downstream locations of the grid have been estimated to be approximately 5 mm (within the range of $19.69 \leq x/M \leq 47.24$) while at $x/M = 3.94$, the Taylor microscale was calculated to be about 3 mm. Present results show a reasonable match with previously reported results on Taylor microscales downstream of grids, where it has also been reported that far downstream both the Taylor microscale and the integral scale remain approximately constant during decay (Hurst and Vassilicos 2007).

3.6 Calibration of PLIF images

A new method of calibration for PLIF measurements is used here. This calibration method is based on the fact that there is constant flux through each cross-section of the fluorescent plume. The source concentration and the volumetric flow rate are known parameters for each experiment and provide the mass flow rate of the fluorescent dye through a section of the plume. The simultaneous measurements of PIV and PLIF enable one to calculate the mean flux across the cross-section in terms of the intensity of the emitted light (after subtracting the mean background intensity). This calculation is done for every pixel column of PLIF images. The procedure is repeated for different initial fluorescent concentrations keeping the relative positions and setup of the laser and the cameras the same. Calibration curves are generated with the linear dependence of intensity flux on concentration flux for every column of the field of view. Each of the calibrated images was also corrected for laser attenuation due to the presence of fluorescent dye. The calibration method described here takes into account the streamwise variation in the laser intensity and corrects it since the calibration method is based on a constant flux across every cross-section of the plume.

Simultaneous PIV and PLIF images are captured for a particular location with different source concentrations (e.g., 12, 25, 50, 75, 100, 125 $\mu g/l$). For each source concentration 1500 images are taken to construct average fields of concentration and velocity. The intensity flux (based on intensity of the emitted light) is calculated considering the mean plume cross-section, which is assumed to be axisymmetric behind a point source and two dimensional behind a line source (equation (3.5) is drawn based on

axisymmetric plume behind a point source). Using different source concentrations, fluxes are calculated by multiplying the intensity (I) and the velocity (u) at a certain point. Therefore the formulation of the total intensity flux at a cross-section behind a point source is

$$Intensity\ flux = \sum_{y=0}^{y_{\langle uI\rangle\to 0}} 2\pi\, y\, \Delta y \langle uI \rangle \quad \left(I \times m^3/\sec\right), \tag{3.5}$$

where y is the radial distance of the point, Δy is the length of an interrogation area and the integration is done from the centreline of the mean plume to the furthest point across the mean plume section, where the value $<uI>$ approaches zero. Figure 3.16(a) depicts a sample of mean intensity flux across a half plume. Figure 3.16(b) shows the variation of the total intensity flux in streamwise direction calculated using equation (3.5). The streamwise variation of the total intensity flux is a result of the variation of the laser intensity in the same direction. The volumetric flow rate of the plume generator and the known source concentration provides source flux,

$$\begin{aligned} Source\ flux &= volumetric\ flow rate \times concentration \\ &= m^3/\sec \times \mu g/litre \\ &= Q \times \Gamma . \end{aligned} \tag{3.6}$$

Since the intensity of the tracer fluorescence is proportional to the local tracer concentration, the source flux is also proportional to the intensity flux. Therefore,

$$\begin{aligned} Source\ flux &\propto Intensity flux \\ Q \times \Gamma &\propto Intensity flux \\ \Gamma &\propto \left(Intensity flux\right)/Q . \end{aligned} \tag{3.7}$$

The fluorescent concentration and emitted light intensity are linearly proportional within a certain range (< 120 $\mu g/l$). The linear relationship is used to produce the

calibration curves. At each location, a set of 4000 simultaneous PIV and PLIF measurements are made with a source concentration within the linear range. In order to get concentration directly, intensity flux is divided by the source volumetric flow rate, Q (m^3/s). Hence, calibration curves for each pixel column are developed using the linear relationship between source concentration and intensity flux per unit volumetric flow rate. A calibration curve for a pixel column is presented in Figure 3.17, which verifies the linear relationship between concentration and intensity in these experiments.

It is to be noted that the resolution of the intensity flux is one fourth of the resolution of PLIF images because of the PIV resolution (see Appendix C for details). Therefore, each calibration curve is used for calibrating four consecutive pixel columns of PLIF images with 400 x 300 pixels. Therefore, the calibration factors, which are nothing but the slopes of the calibration curves, are extended between consecutive four pixel columns as shown in Figure 3.18.

Each image needs to be corrected for vertical laser attenuation due to the presence of fluorescent dye. The corrected intensity can be calculated using Beer-Lambert law (Ferrier et al. 1993) as

$$I = I_o \exp\{(\alpha_w + \alpha_o \Gamma)\Delta y\}, \tag{3.8}$$

where, I is the intensity (grayscale) at location $y+\Delta y$, I_o is the intensity at location y, Γ is the local dye concentration ($\mu g/l$), α_w and α_o are the attenuation coefficients in water and extinction coefficient resulting from the fluorescent dye. The extinction coefficient resulting from Rhodamine 6G is a constant and equal to 0.00023 cm^{-1} $(\mu g/l)^{-1}$ and the

attenuation coefficients in water vary from 0.0011 to 0.0045 cm^{-1} (Daviero et al. 2001). In the above equation, local concentration (I) comes from previously calculated concentration using the linear calibration curve.

An attempt is made here to demonstrate a comparison of the present results with some previous studies. Mean concentration profiles in centreline vertical planes at the different distances downstream of the grid are shown in Figures 3.19. Each profile can be scaled with two parameters; the local centreline mean concentration C_o, and the spatial variance of the plume, σ. The spatial variance can be obtained for each profile using a least-squares fit to the Gaussian,

$$\frac{C}{C_o} = \exp\left\{\frac{-y^2}{2\sigma^2}\right\}. \tag{3.9}$$

A representative example of the least-squares fit to the Gaussian for all of the line source and point source plumes is shown in Figure 3.20 for the mean concentration profile behind a point source at a distance 500 mm from the grid. The variance growth rates for both the line source and the point source are shown in Figure 3.21. Normalized mean concentration at several streamwise locations are shown in Figure 3.22, where each profile is scaled with centreline line mean concentration (C_o) and spatial variance (σ). The mean vertical concentration data are clearly Gaussian and self-similar, which is in agreement with previous experimental studies (Fackrell and Robins 1982; Bara et al. 1992; Crimaldi et al. 2002).

Figures 3.23 and 3.24 present the vertical profiles of the distributed moments for several locations. The data is fitted using the parameters discussed in equation (2.36) in

Chapter 2. Sawford & Sullivan (1995) fitted these parameters to the data from a steady line source experiment in wind tunnel grid turbulence. The constants α, β vary with downstream distance for a steady release and are shown in Figures 3.25. The trends appear to follow the suggested behavior (Chatwin and Sullivan 1990). The expressions for K_n given in equation (2.37) in Chapter 2 are used to fit the normalized moments that are shown in Figures 3.26 and 3.27. The relationships between the moments predicted by Chatwin and Sullivan (1990) and Sawford and Sullivan (1995) have been found to agree reasonably well with present measurements, which have been found to be valid from a range of experiments including jets, wakes, plumes, uniformly sheared flow and buoyant jets (Chatwin and Sullivan 1990; Moseley 1991; Sawford and Sullivan 1995; Ye 1995).

3.7 Experimental summary and flow properties

In total, seven sets of experiment were conducted with two different plume source conditions. A summary of the experiments performed is presented in Table 3.1. Experiments were carried out using two different plume source conditions. One is a continuous point source and the other one is a continuous line source.

The measurements were carried out in grid turbulence generated by a square mesh grid, which gives a Reynolds number ($Re = UM/\nu$) of 5000 based on the mesh size and a flow speed of 0.2 m/sec. The flow properties (Taylor Micro-Scale Reynolds number ($Re_\lambda = \sqrt{\{<u^2>\}}\lambda/\nu$), dissipation rate ($\varepsilon$) and the Kolmogorov scale ($\eta = (\nu^3/\varepsilon)^{1/4}$), for details check Appendix A) are presented in Table 3.2.

Table 3.1: Summary of the experiments

Source condition	Flow condition	Measurement locations (mm)
Point source	Grid turbulence	500, 700, 1200, 1800
Line source	Grid turbulence	150, 500, 700

Table 3.2: Flow properties of the tunnel flow

	x (mm)	Taylor Microscale Reynolds number (Re_λ)	Dissipation rate (ε)	Kolmogorov scale (η), mm	Batchelor scale (η_B), mm
Point Source	500	37	9.2×10^{-6}	0.57	0.016
	700	30	3.8×10^{-6}	0.72	0.020
	1200	22	1.9×10^{-6}	0.84	0.024
	1800	16	1.7×10^{-6}	0.87	0.025
Line Source	150	35	9×10^{-5}	0.32	0.009
	500	23	8×10^{-5}	0.33	0.009
	700	15	1×10^{-5}	0.56	0.016

3.8 Data Processing

An important aspect of these experiments is the calculation of higher moments of simultaneous velocity and concentration, which involves relatively large experimental uncertainties. For the CCD cameras, the noise levels were reported to have a standard deviation of the order of two grey scale intensity levels (Ferrier et al. 1993). A series of 500 images were taken with a dark background (camera was covered with black cloth in a dark room) to check the noise levels and the standard deviation was found to be of the same order. The error from the camera noise level propagates through the calculations (Ferrier et al. 1993). The uncertainty analysis and the propagation of error are discussed in the Appendix B.

There is a tradeoff between experimental resolution and the uncertainties in the measurements. The convective closure validation (equation (2.54) and (2.55) in Chapter 2) is based on simultaneous measurements of velocity and concentration. The resolution in velocity measurements is restricted to 16 pixels after using 32 x 32 pixels interrogation area with 50% overlap. Therefore, the resolution of the concentration flux ($u'T$) depends on the resolution of velocity measurements. If one uses concentration (PLIF) measurements with 1600 x 1200 pixels array, the propagated error in the product becomes significant (>50%) for higher n values (order of moments). For this study we will cap $n \leq 3$. Since the resolution of the concentration flux depends on the coarser resolution of the PIV measurements, it is reasonable to apply the supersampling (i.e., averaging over a pixel array) method to each PLIF image in order to reduce the noise levels of the PLIF images. In order to estimate the proper averaging dimension, the time series are captured at a fixed location of PLIF images for different supersampling (averaging) dimensions (e.g., 2 x 2, 4 x 4, 8 x 8). The results are shown in Figure 3.28, where the spikes represent the scalar concentration filaments in the flow field. All three dimensions of the supersampling capture the basic "spiky" feature in the concentration field because the width of the filaments are of the order of the Kolmogorov scale that is larger than the largest supersampling dimension used here (albeit suppressed spikes are noticed for the case of 8 x 8 in some places in the time series). Figure 3.29 presents the PDFs of the concentration measurements for different supersampling dimensions. The three dimensions of the supersampling show a similar distribution. In order to get the convergence, the running averages are plotted in Figure 3.30, which shows a similar trend i.e., converge within the same number of realizations (samples). From the above analysis,

it is evident that from the scalar dissipation calculation point of view, where the actual concentration gradients are important, the use of 4 x 4 averaging is a reasonable approximation. It has also been observed using the dark background images that supersampling over a 4 x 4 pixel array reduces the noise level in PLIF images. The method of supersampling produces a PLIF image with a pixel array of 400 x 300 and the measurement resolution worsens, for example, to 0.13 mm from 0.033 mm at a distance 500 mm downstream of the grid behind a point source. The resolution in velocity measurements at this location is 0.52 mm. Figures 3.31 depict the resolution in both PLIF and PIV measurements. Figure 3.31(a) is a raw PLIF measurement whereas Figure 3.31(b) shows the same image supersampled over a 4 x 4 pixel array with a qualitative velocity map on it. A typical plot of simultaneous measurements of fluctuating velocity and intensity fields are shown in Figure 3.32. The supersampled images are calibrated using the method described in § 3.6.

The products ($\langle u'\Gamma^{n+1}\rangle$ and $\langle v'\Gamma^{n+1}\rangle$) of the convective closure validation were calculated by multiplying the fluctuating components of the velocity and the calibrated concentration value, raised to the power of $n+1$, followed by ensemble averaging of 4000 realizations. Taylor's "frozen turbulence" hypothesis allows us to use spatial average in the flow direction within a small distance where changes in the mean flow properties are negligible. The use of spatial averaging is not a sacrifice in individual point resolution in the measurements but, rather, an increase in number of points in the ensemble. An average of ten columns was taken to represent the final mean profiles of $\langle u'\Gamma^{n+1}\rangle$ and $\langle v'\Gamma^{n+1}\rangle$. Figures 3.33 represent the mean profiles of $\langle u'\Gamma^{n+1}\rangle$, $\langle v'\Gamma^{n+1}\rangle$ and

$y\langle v'\Gamma'^{n+1}\rangle$ behind a point source. The third term $y\langle v'\Gamma'^{n+1}\rangle$ was calculated for the axisymmetric case only, where y is the distance from the centreline of the plume. The calculated term ($\langle u'\Gamma'^{n+1}\rangle$) does not change significantly within one measurement plane in streamwise direction. Therefore, the streamwise gradients of mean concentration and $\langle u'\Gamma'^{n+1}\rangle$ were calculated between two consecutive measurement planes (for example, between 500 mm and 700 mm for point source measurements) representing a location at x ~ 600 mm. An average profile of $y\langle v'\Gamma'^{n+1}\rangle$ was generated by taking the average of 500 mm and 700 mm, for example, to represent the same location (x ~ 600 mm) of the streamwise gradients. Figure 3.34 depicts the gradient scheme of the measurements in both the streanwise and cross-stream directions. The cross-stream gradients were calculated using the linear central difference method within vertical pixels. Figures 3.35(a, b) show gradients of $\langle u'\Gamma'^{n+1}\rangle$ and $\langle v'\Gamma'^{n+1}\rangle$ profiles in two directions. Figure 3.36 is the representation of streamwise gradients of mean concentration. These three terms $d(\langle u'\Gamma'^{n+1}\rangle)/dx$, $d(y\langle v'\Gamma'^{n+1}\rangle)/dy$ and dC/dx are used to validate the convective closure approximation.

Figures 3.37 show the gradient calculation of absolute concentration in two directions. These gradient terms are squared and multiplied by the local absolute concentration powered by $n-1$, where n is the order of moment. These two terms are then added together to construct the LHS of the dissipative closure solution (equation (2.57) in Chapter 2) for one realization. This is followed by an ensemble average over 4000 realizations (images). The RHS of the solution is calculated by an ensemble average over

4000 images of absolute concentration powered by $n+1$, $<\Gamma^{n+1}>$. These two terms are plotted for first order of moment (Figure 4.19 in Chapter 4).

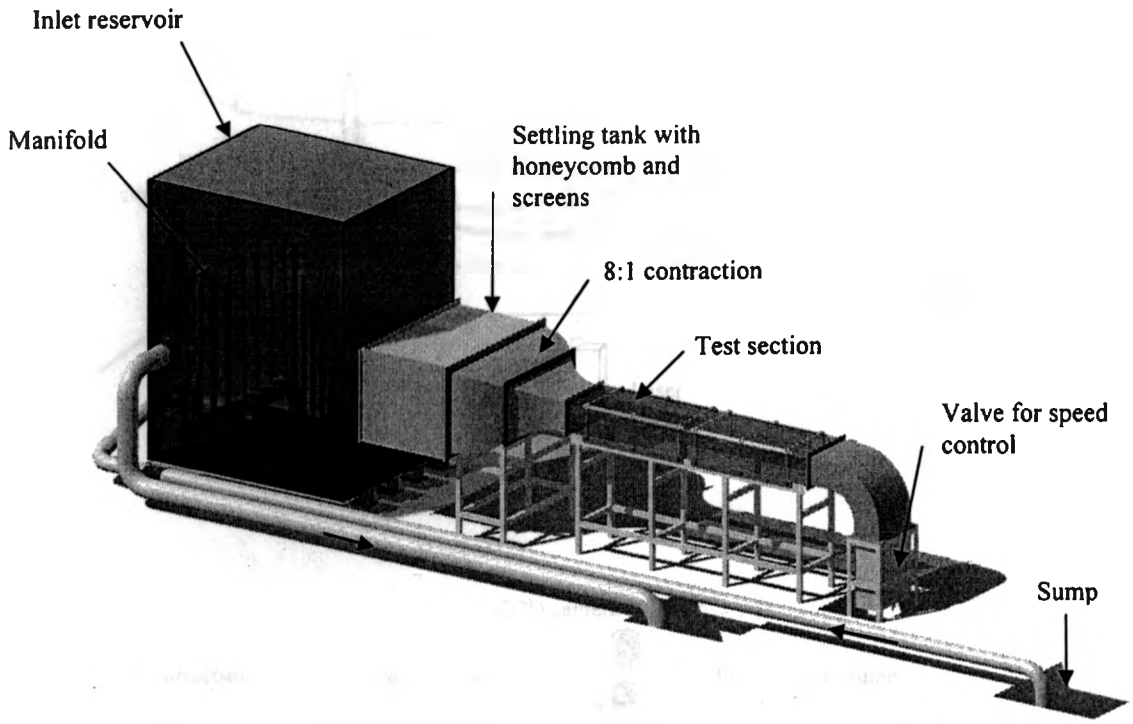

Figure 3.1: Isometric view of the water tunnel.

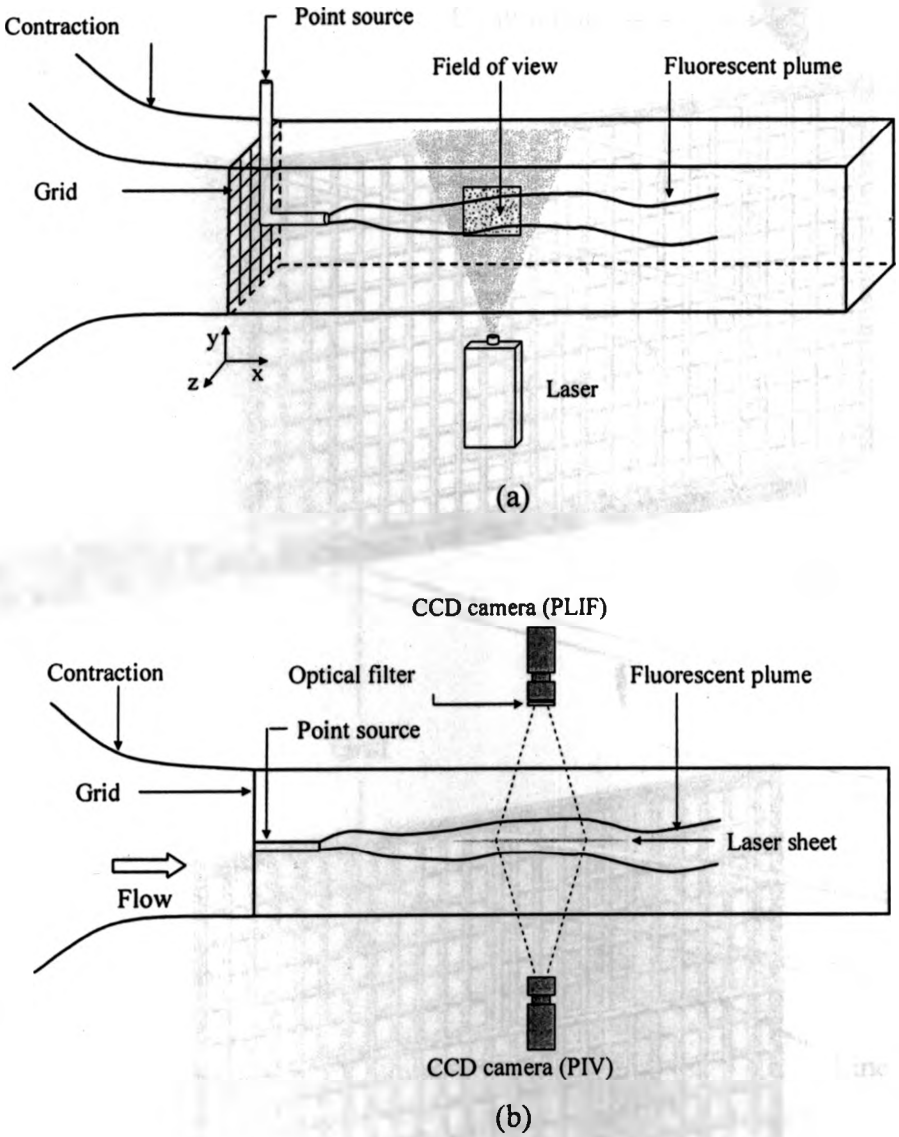

Figure 3.2: (a) Schematic view, (b) top view of the experimental setup.

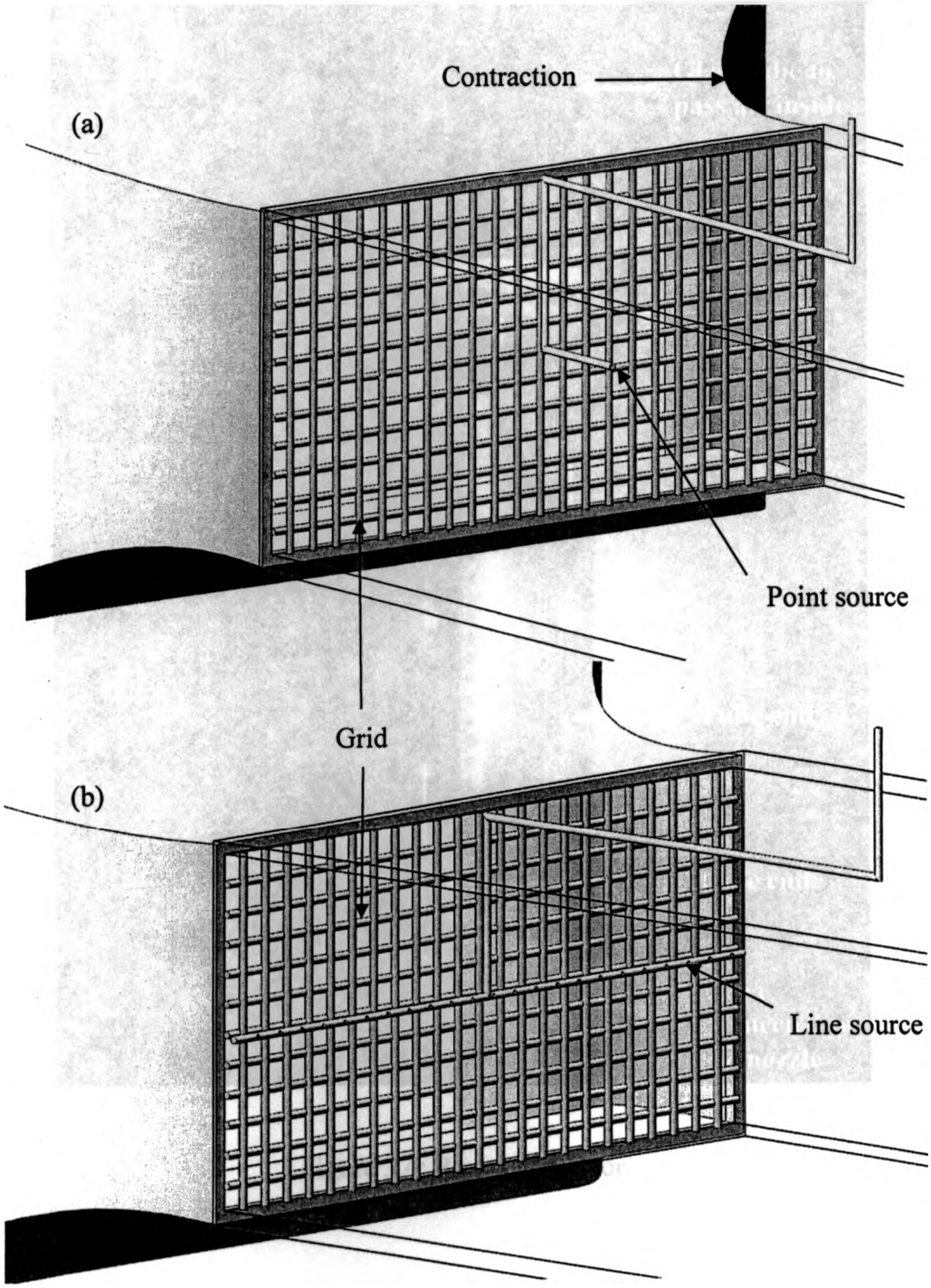

Figure 3.3: Setups of (a) the point source and (b) the line source with the grid.

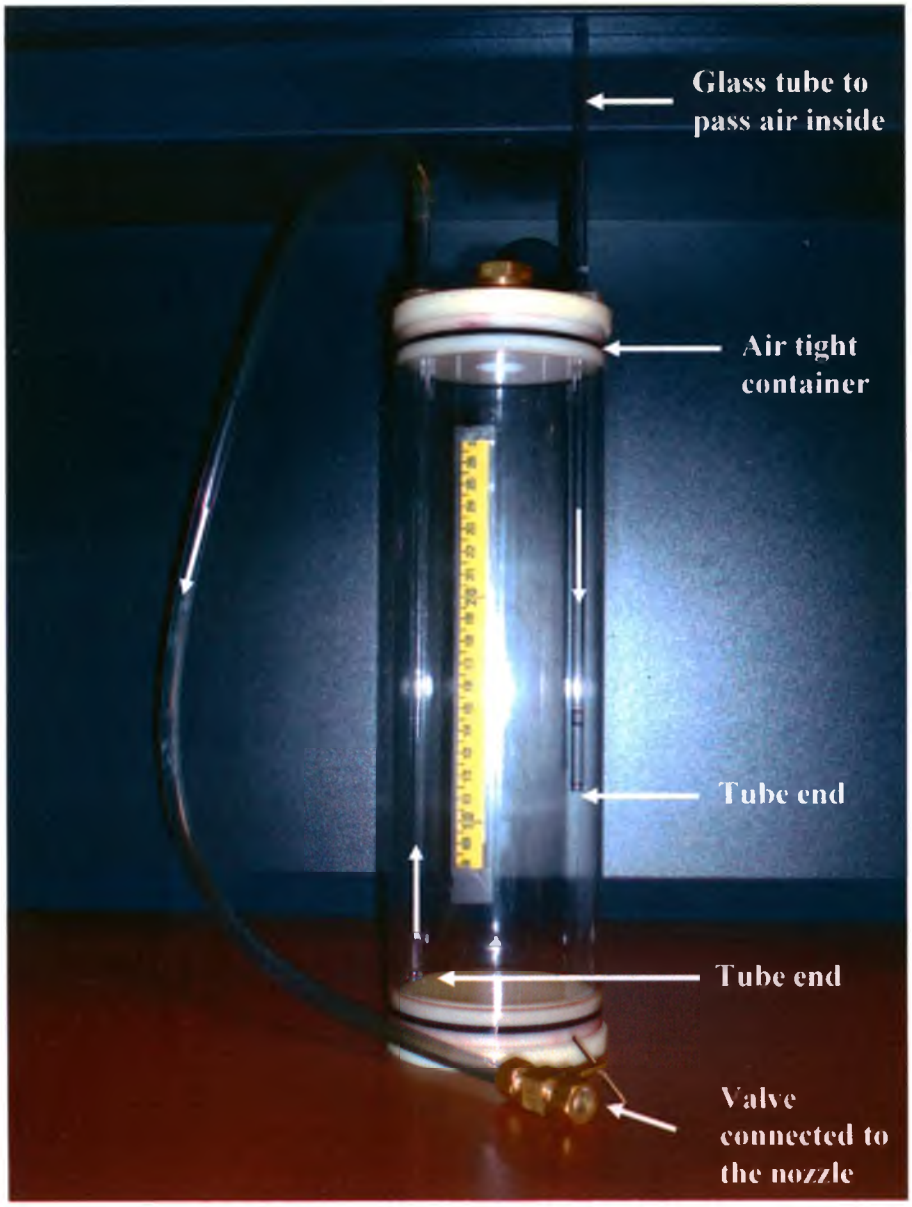

Figure 3.4: Plume generator.

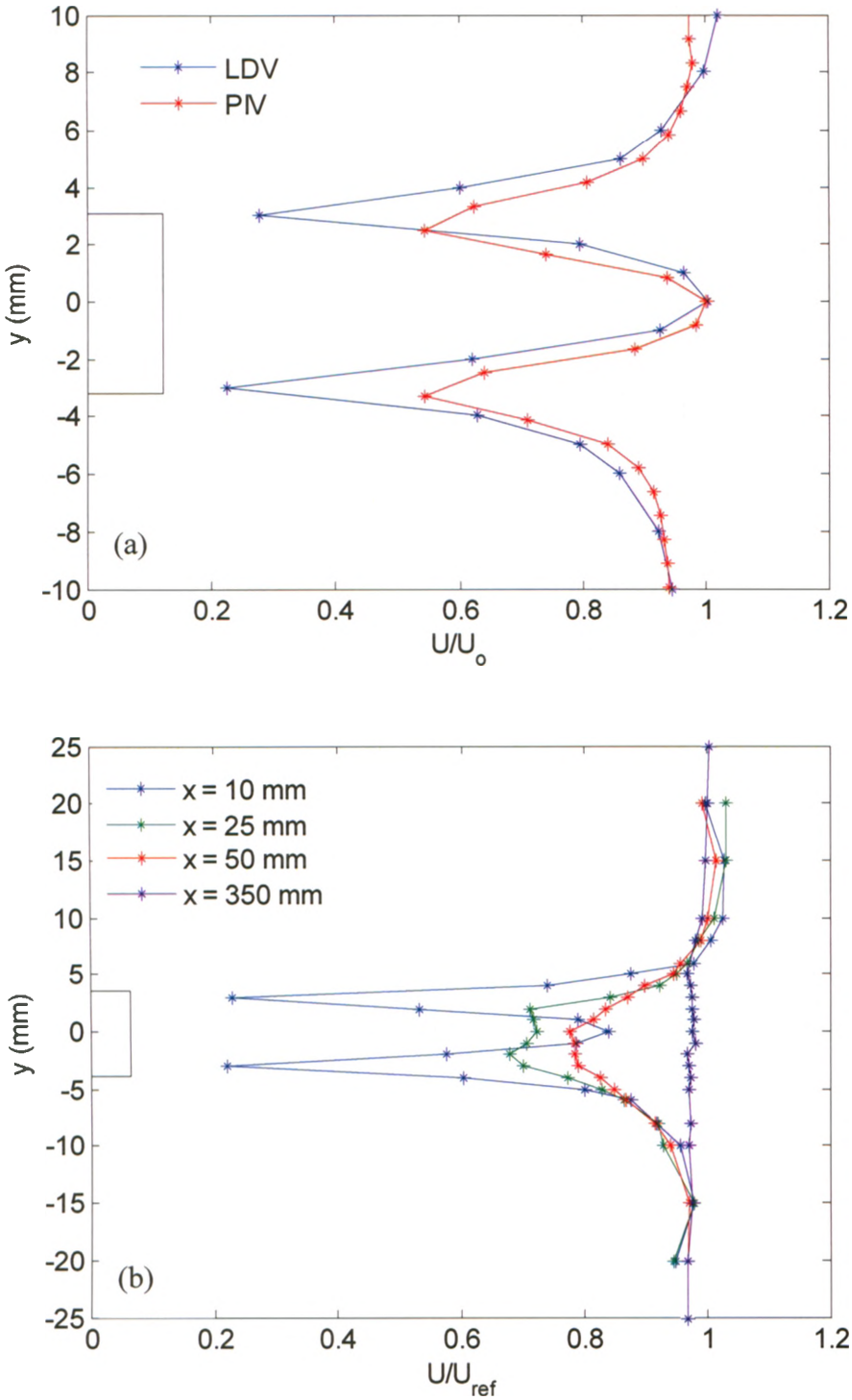

Figure 3.5 (a) Mean velocity profiles at a distance 5 mm downstream of the nozzle using PIV and LDV; (b) Mean velocity profiles at different downstream locations using LDV.

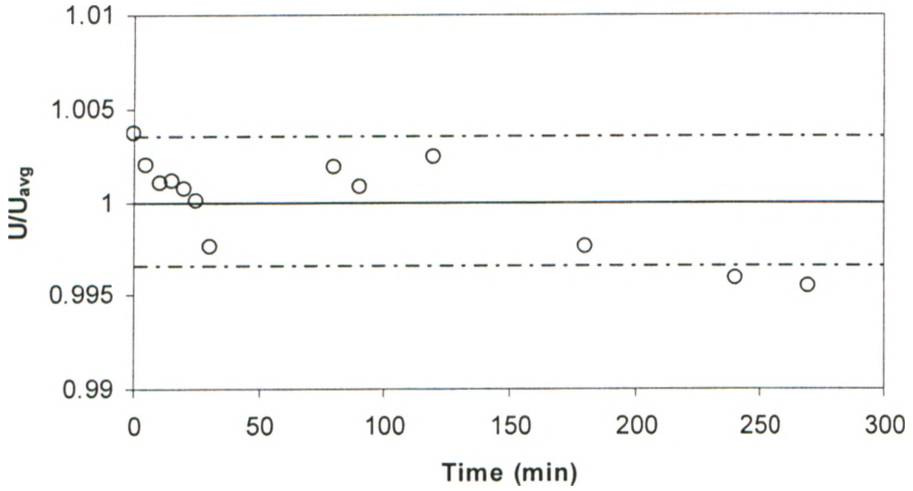

Figure 3.6: Variation of the mean streamwise velocity with time on the centreline at x/h = 1.67. The dashed line represents the 95% confidence limits of the LDV measurements.

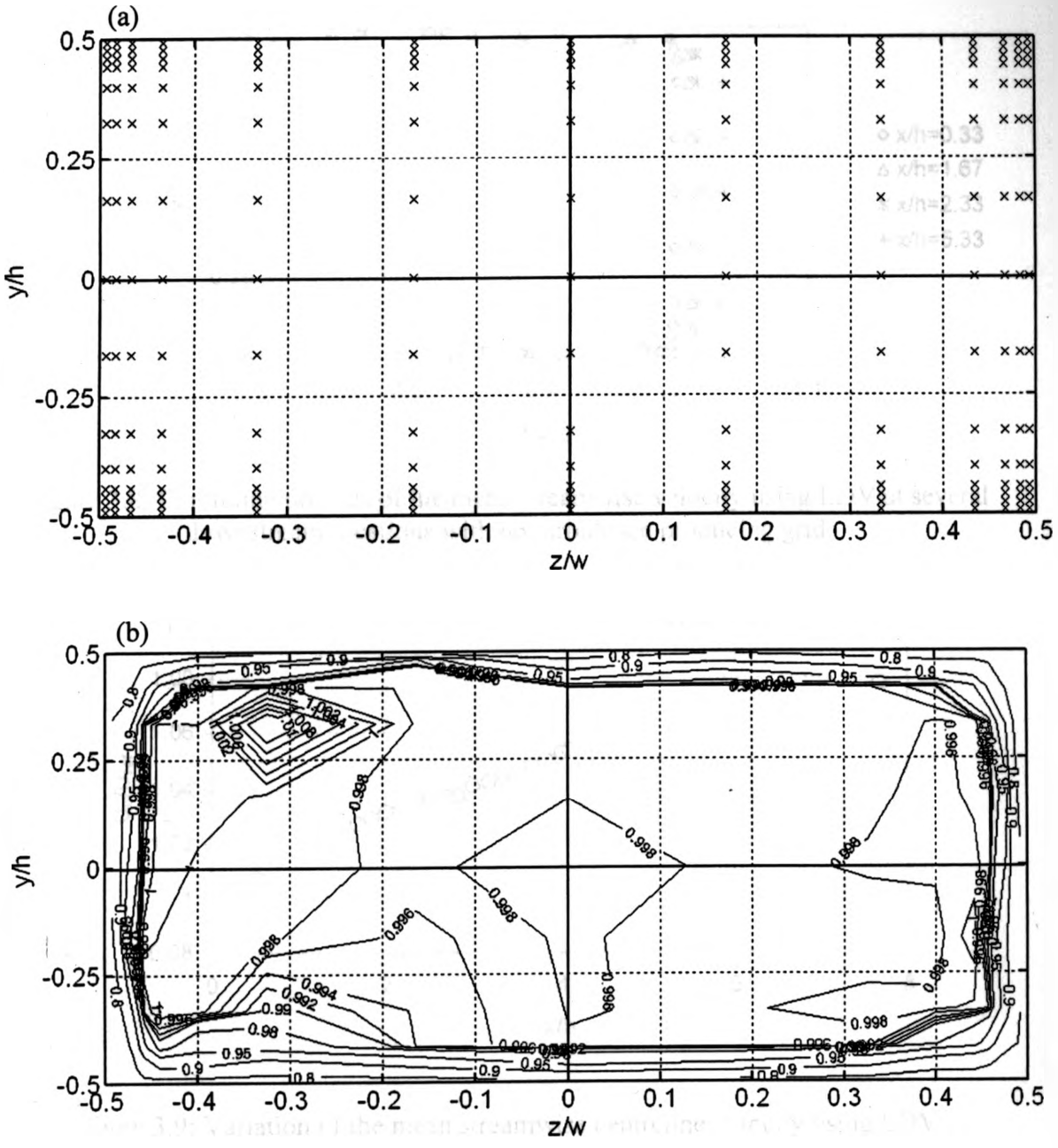

Figure 3.7: a) LDV measurement locations at x/h = 2.33, b) contour plot of the relative velocity of the tunnel cross-section at x/h = 2.33.

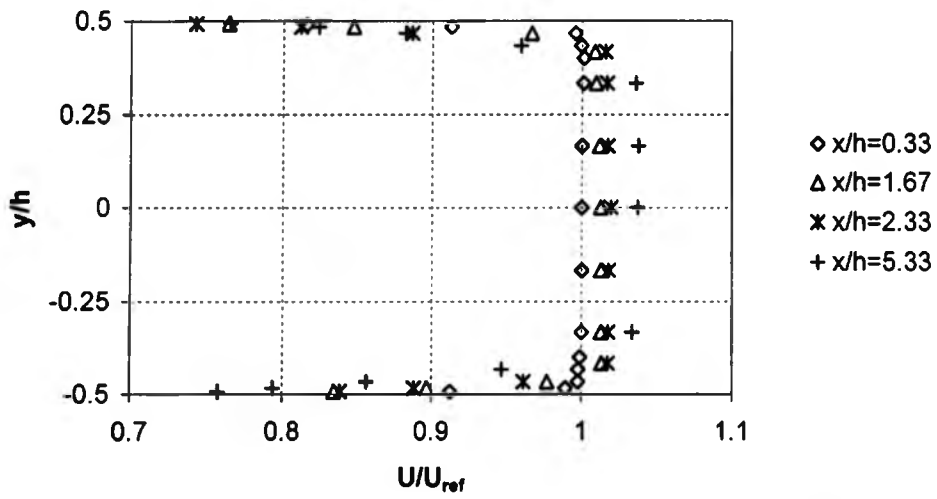

Figure 3.8: Centreline profiles of the mean streamwise velocity using LDV at several downstream locations with no turbulence producing grid.

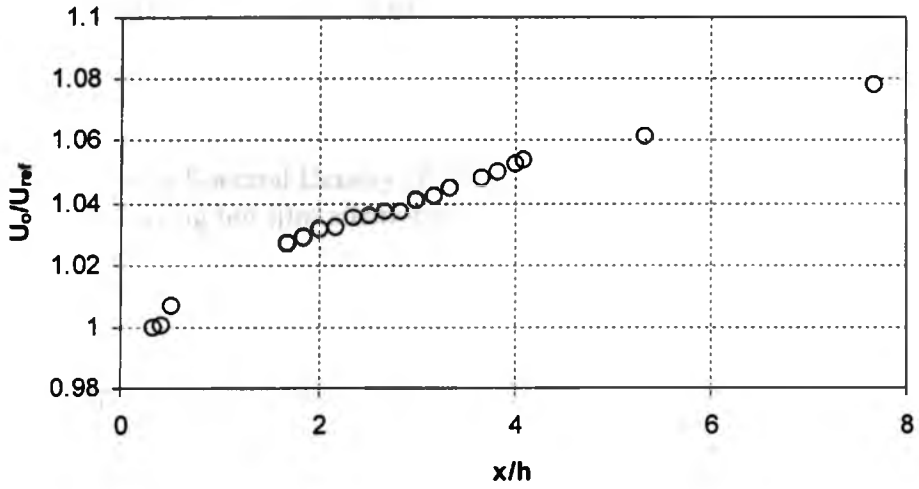

Figure 3.9: Variation of the mean streamwise centreline velocity using LDV.

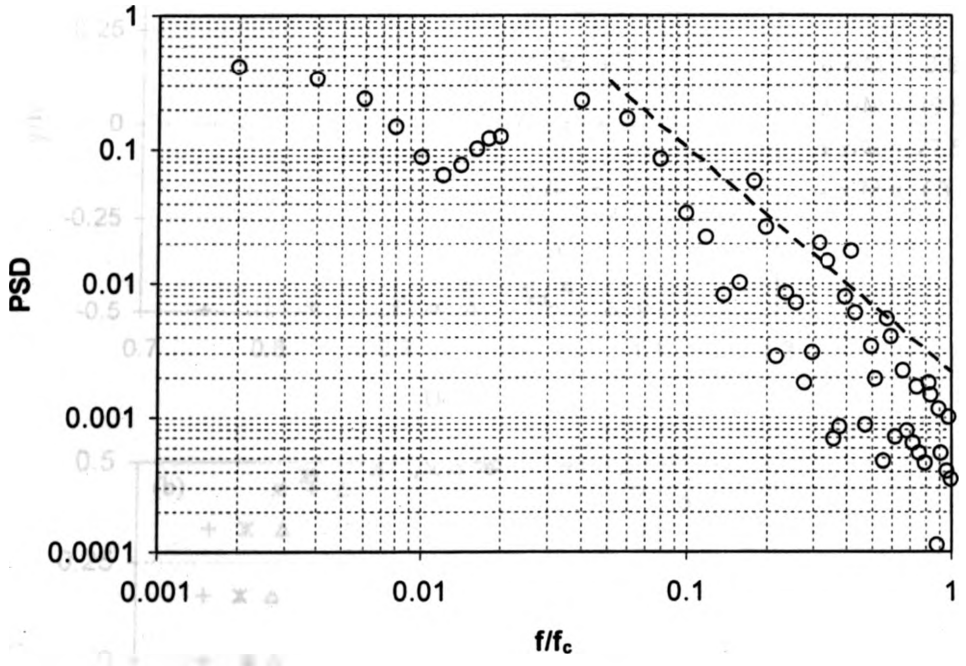

Figure 3.10: Power Spectral Density (*PSD*) of the streamwise velocity in the empty tunnel using hot film anemometry (dashed line is for -5/3 slope).

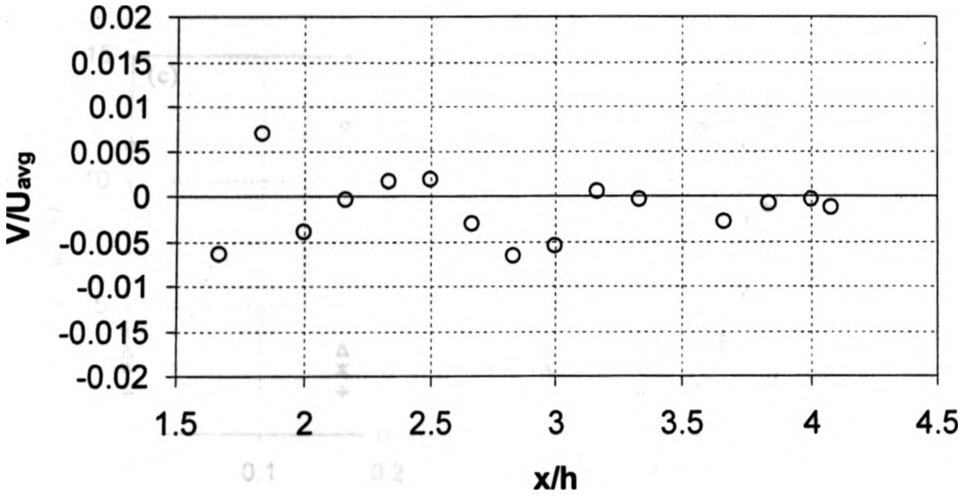

Figure 3.11: Relative vertical velocity components at centreline of the water tunnel for different locations downstream of the grid.

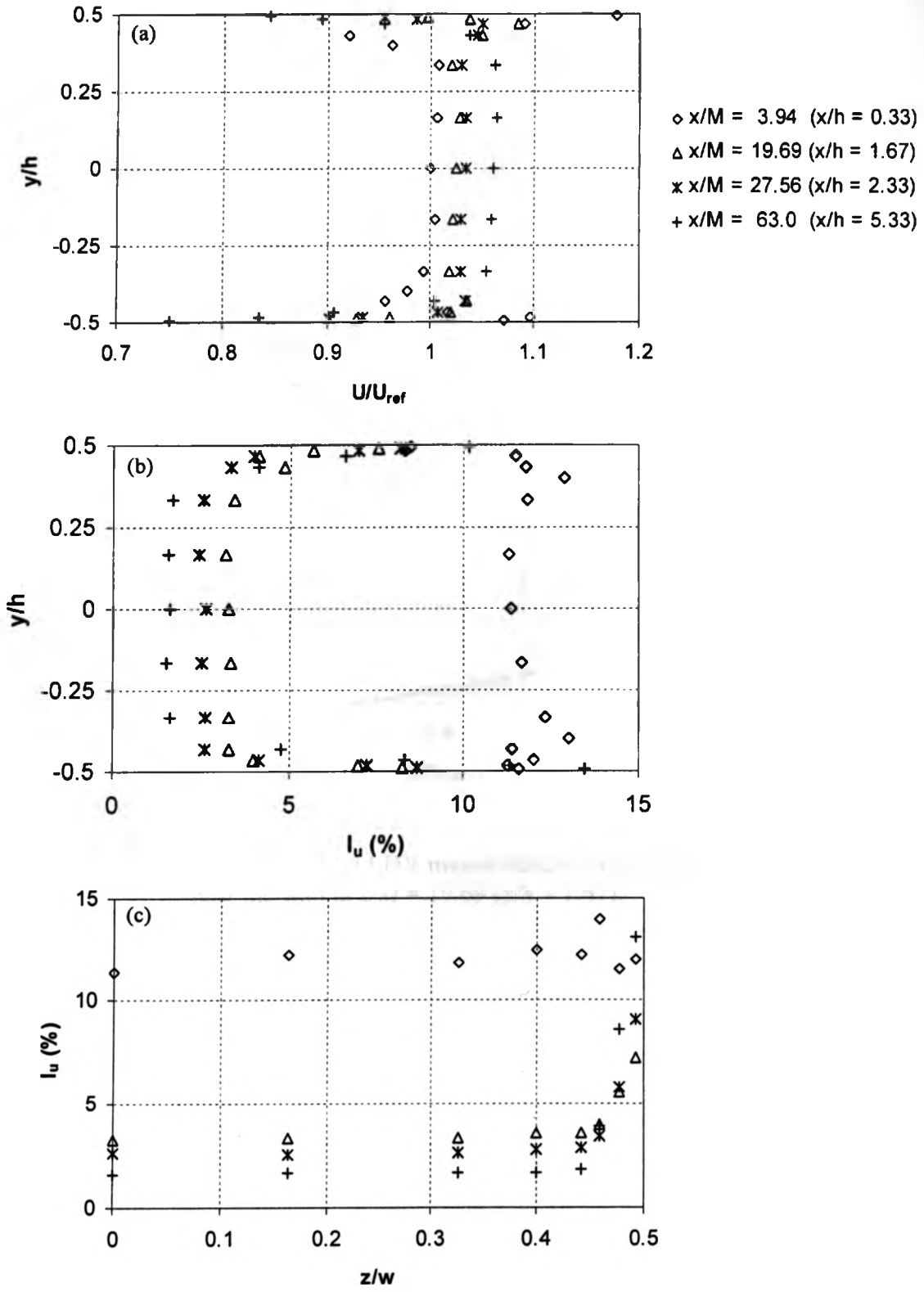

Figure 3.12: Centreline profiles in grid turbulence of (a) mean streamwise velocity, (b) turbulence intensity, and (c) lateral profiles of turbulence intensity.

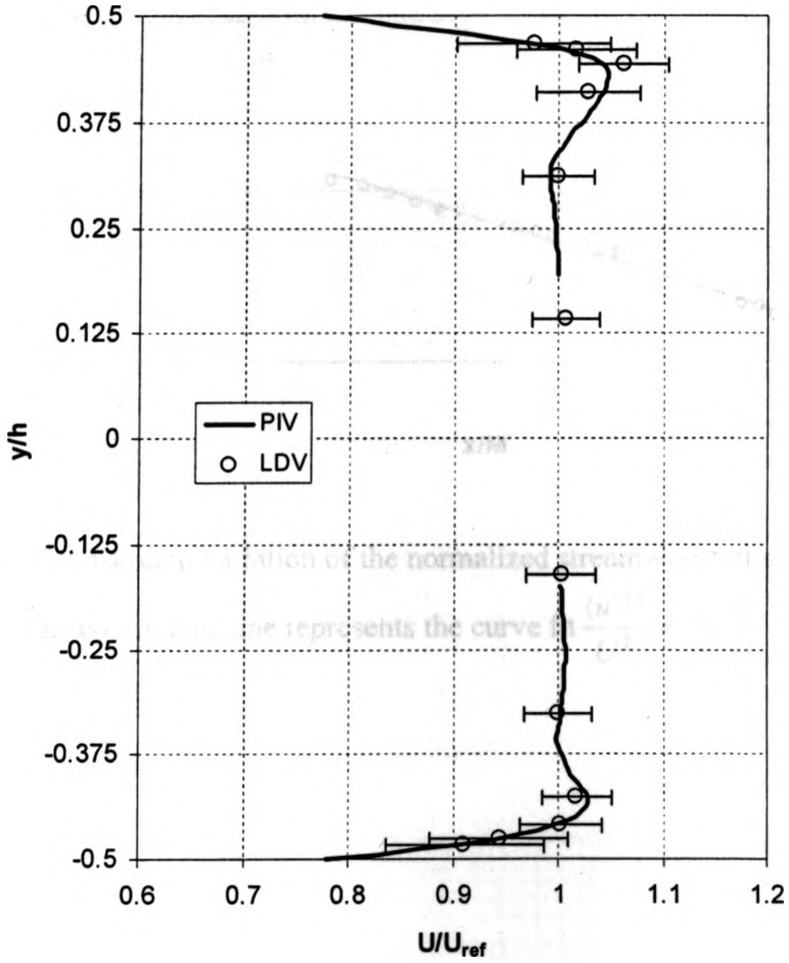

Figure 3.13: Comparison of the PIV and LDV measurements of the streamwise velocities near the wall at $x/M = 19.69$ ($x/h = 1.67$).

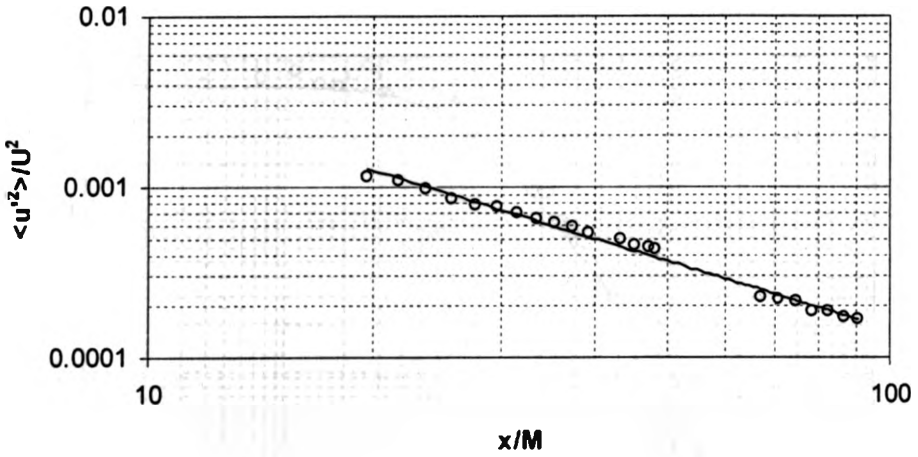

Figure 3.14: Downstream variation of the normalized streamwise turbulence intensity. The continuous line represents the curve fit $\frac{\langle u'^2 \rangle}{U^2} = G\left(\frac{x}{M}\right)^{-n}$.

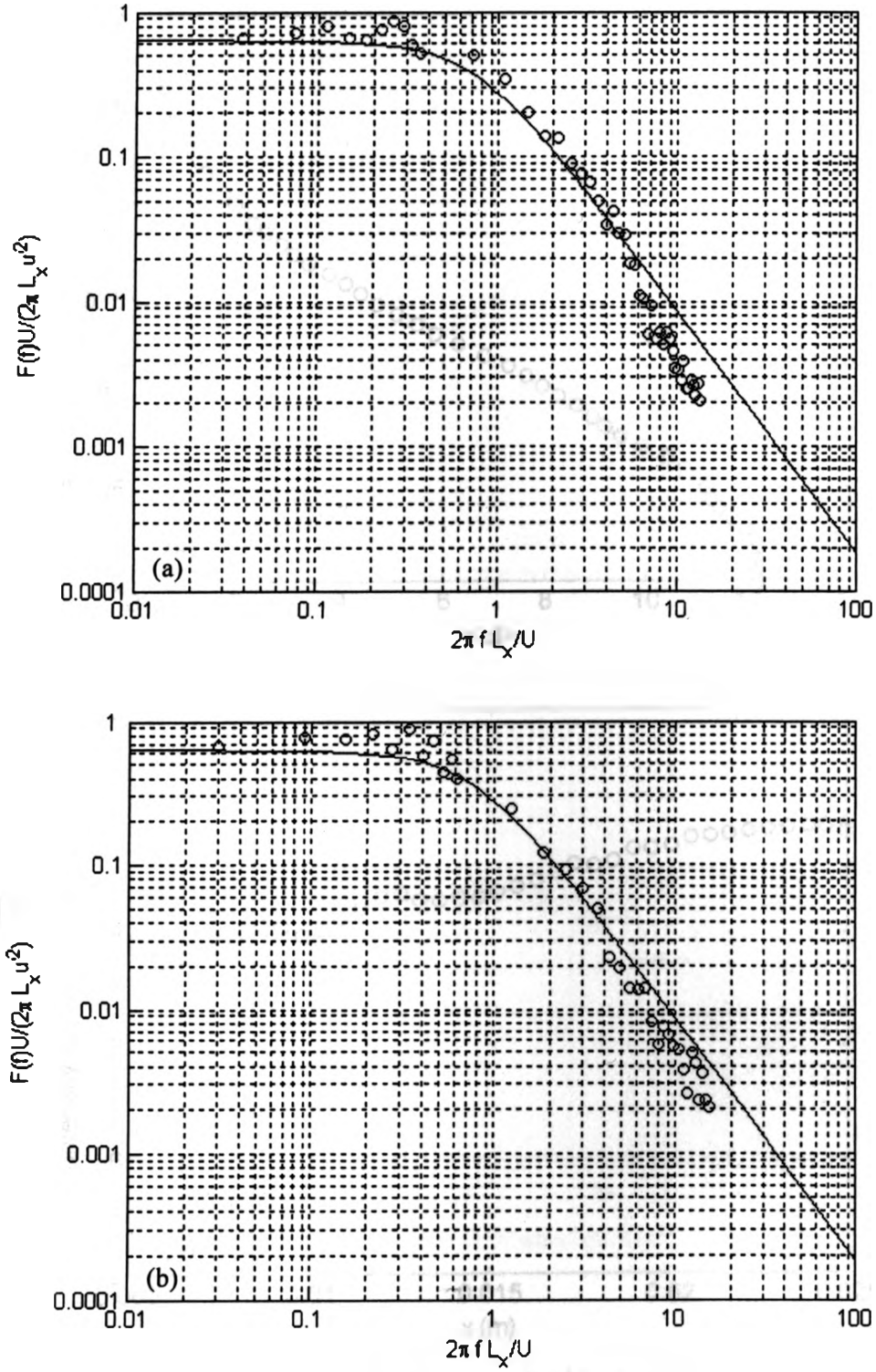

Figure 3.15: Power spectra at (a) $x/M = 3.94$ ($x/h = 0.33$) (b) $x/M = 27.56$ ($x/h = 2.33$) downstream of the grid. The solid line is the von Kármán spectrum.

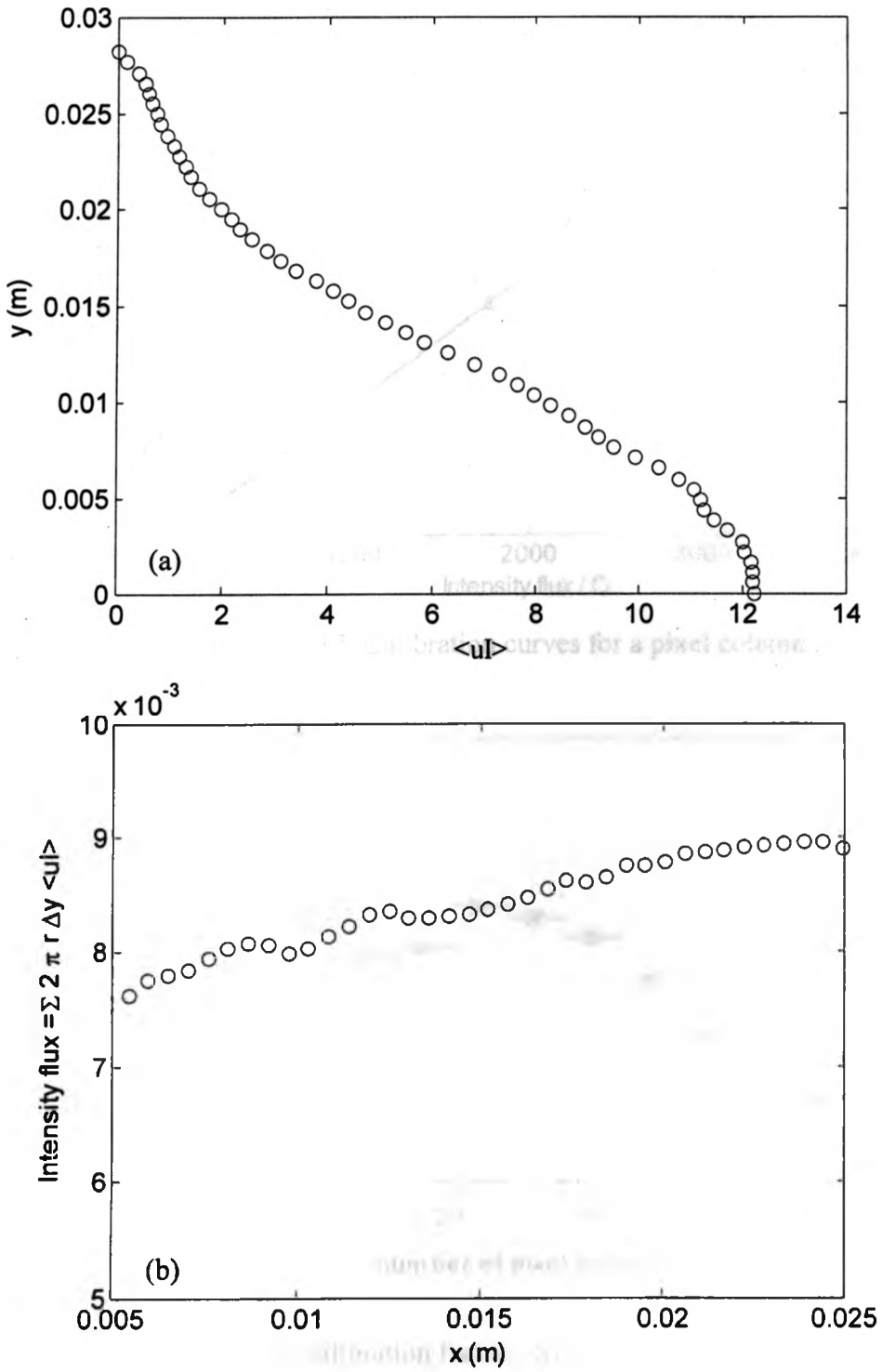

Figure 3.16: (a) Mean Intensity flux across a half plume, (b) Variation of the total intensity flux in streamwise direction.

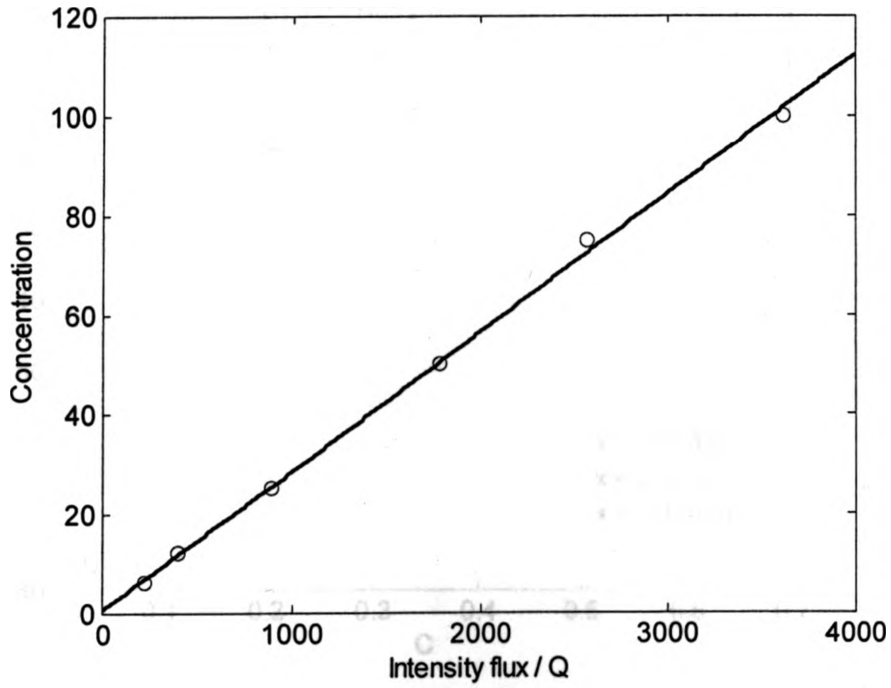

Figure 3.17: Calibration curves for a pixel column.

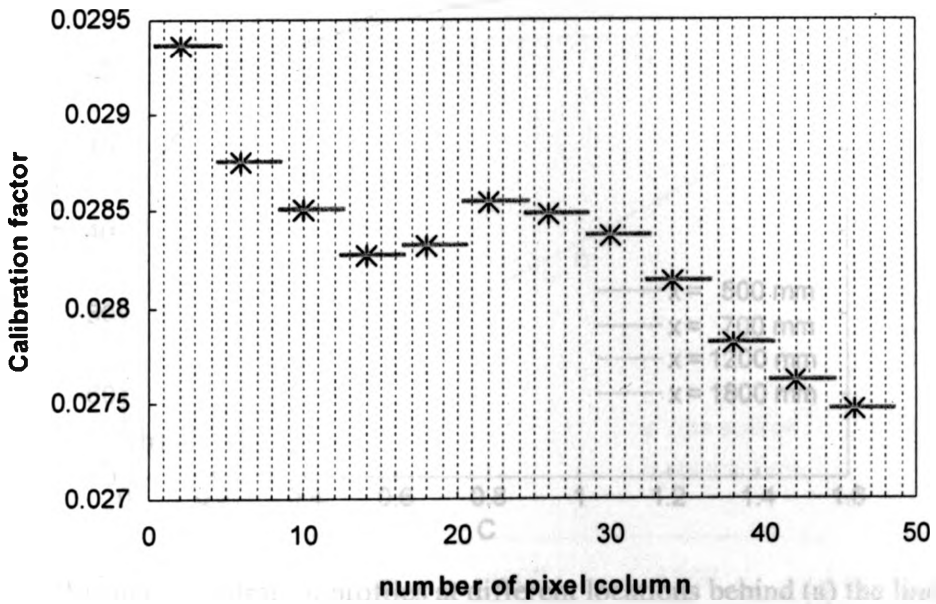

Figure 3.18: Extension of the calibration factors. Symbol cross (x) represents measured calibration factors, and the lines represents the extension of the calibration factors within consecutive pixel columns.

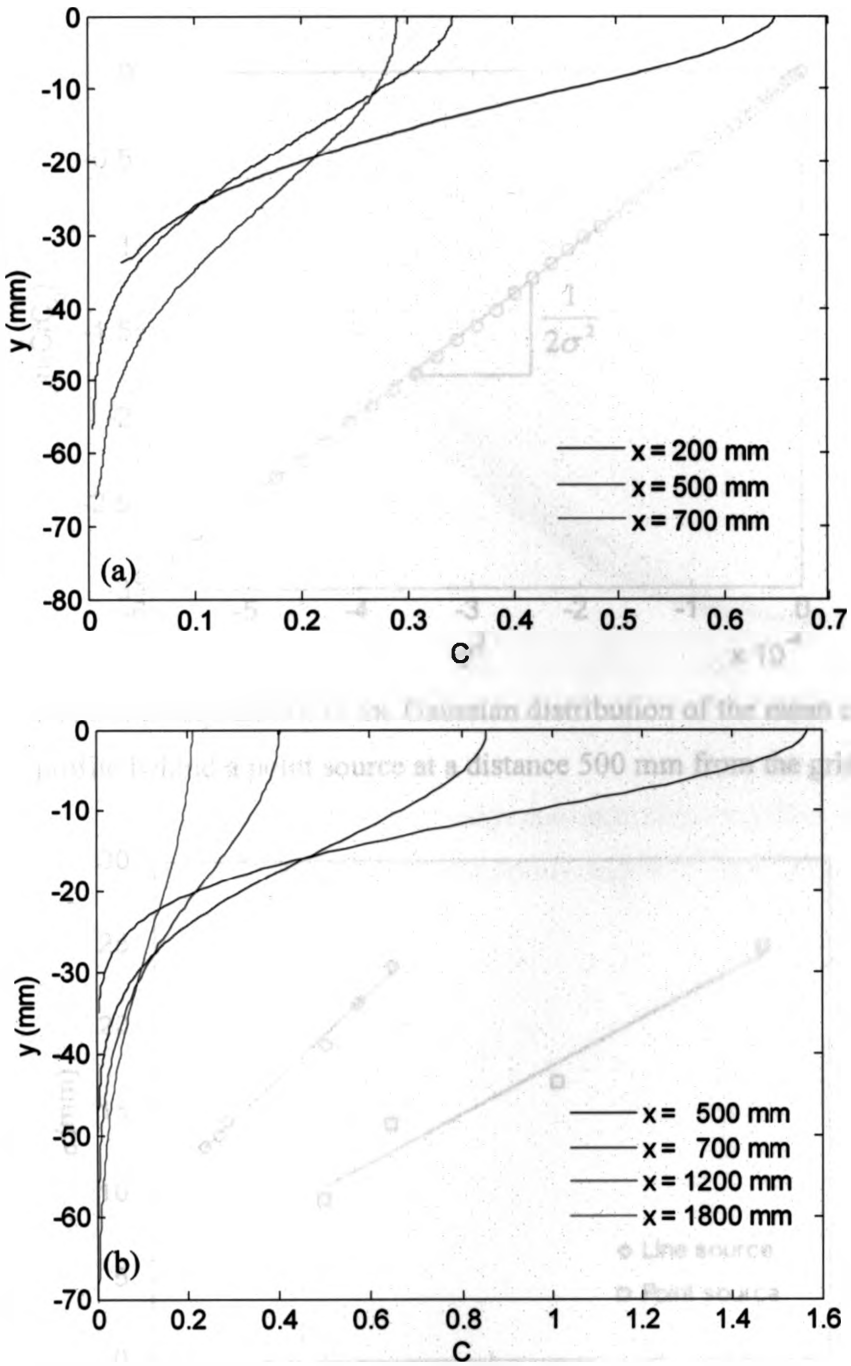

Figure 3.19: Mean concentration profiles at different locations behind (a) the line source, (b) the point source.

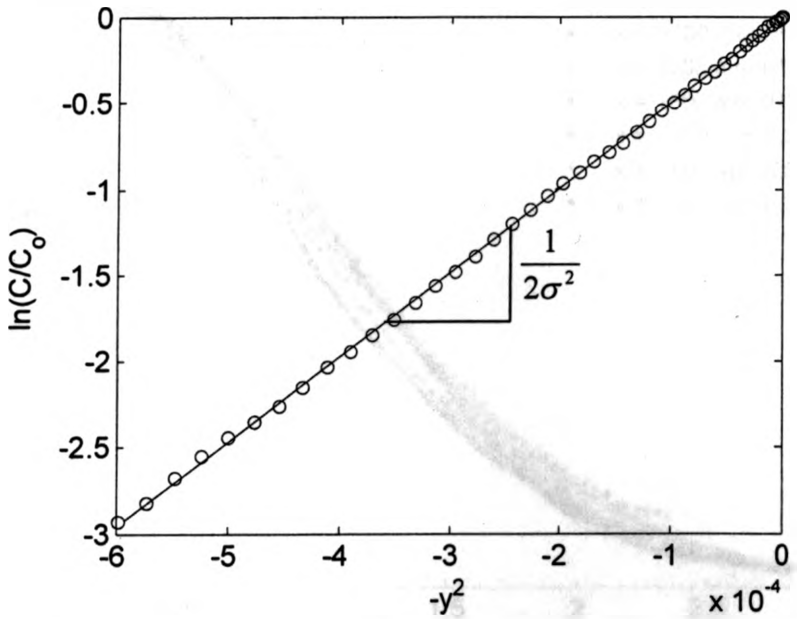

Figure 3.20: The least-squares fit to the Gaussian distribution of the mean concentration profile behind a point source at a distance 500 mm from the grid.

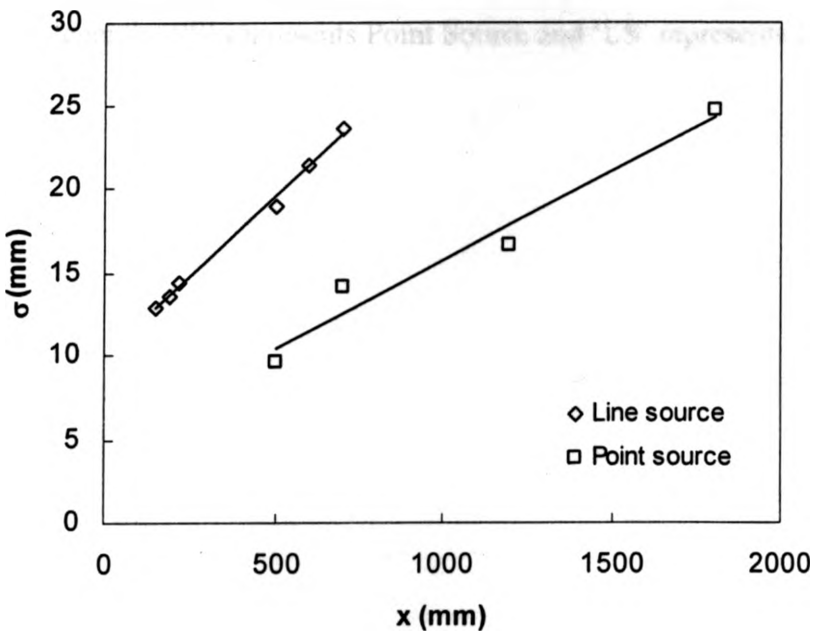

Figure 3.21: Variation of spatial variance with downstream distance.

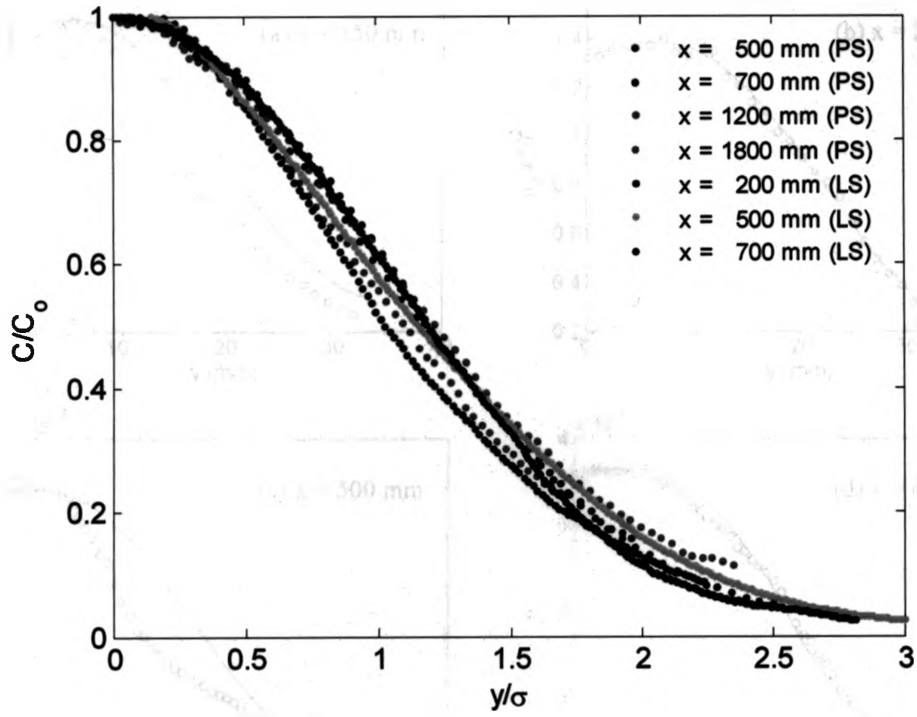

Figure 3.22: Normalized vertical profiles of mean concentration for different downstream locations. In the legends 'PS' represents Point Source and 'LS' represents Line Source.

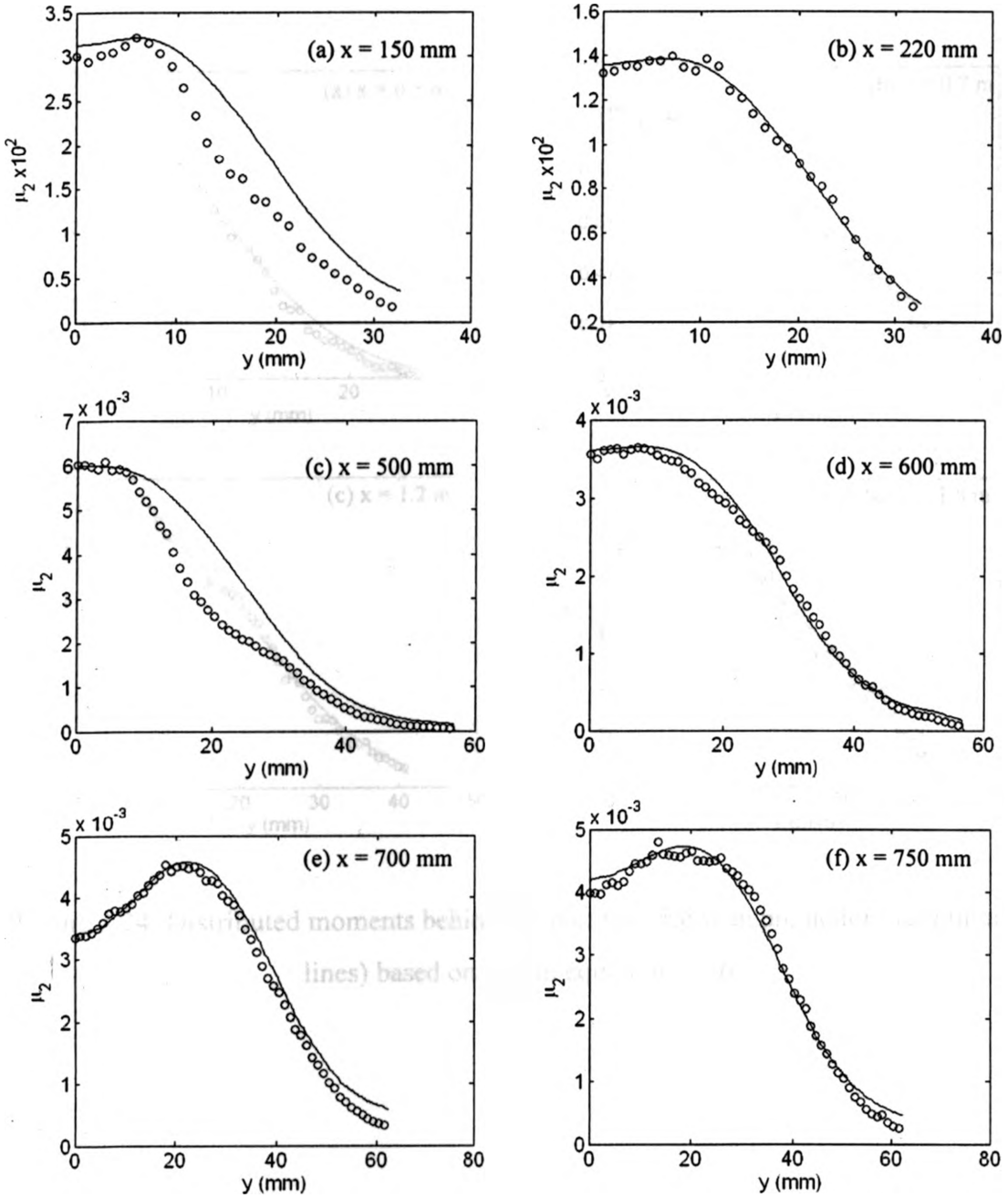

Figure 3.23: Distributed moments behind the line source with predictions (continuous lines) based on α-β in equation (2.36).

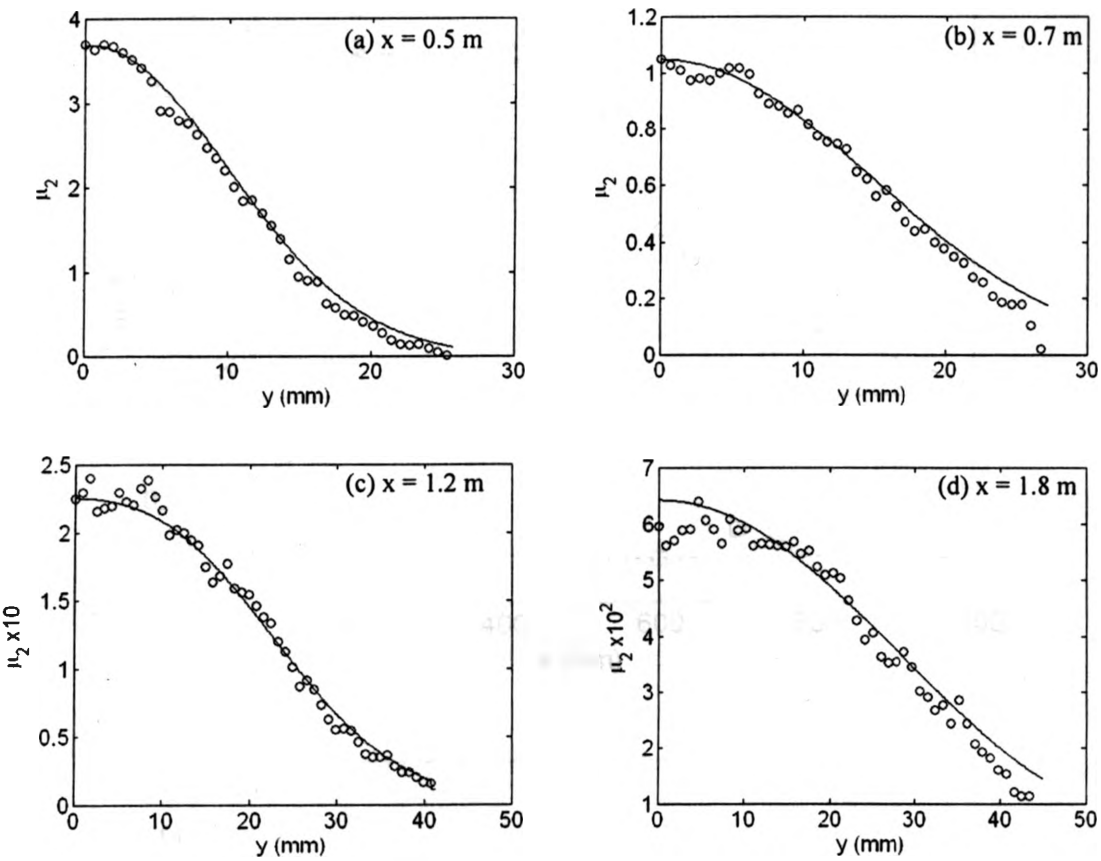

Figure 3.24: Distributed moments behind the point source with predictions (continuous lines) based on α-β in equation (2.36).

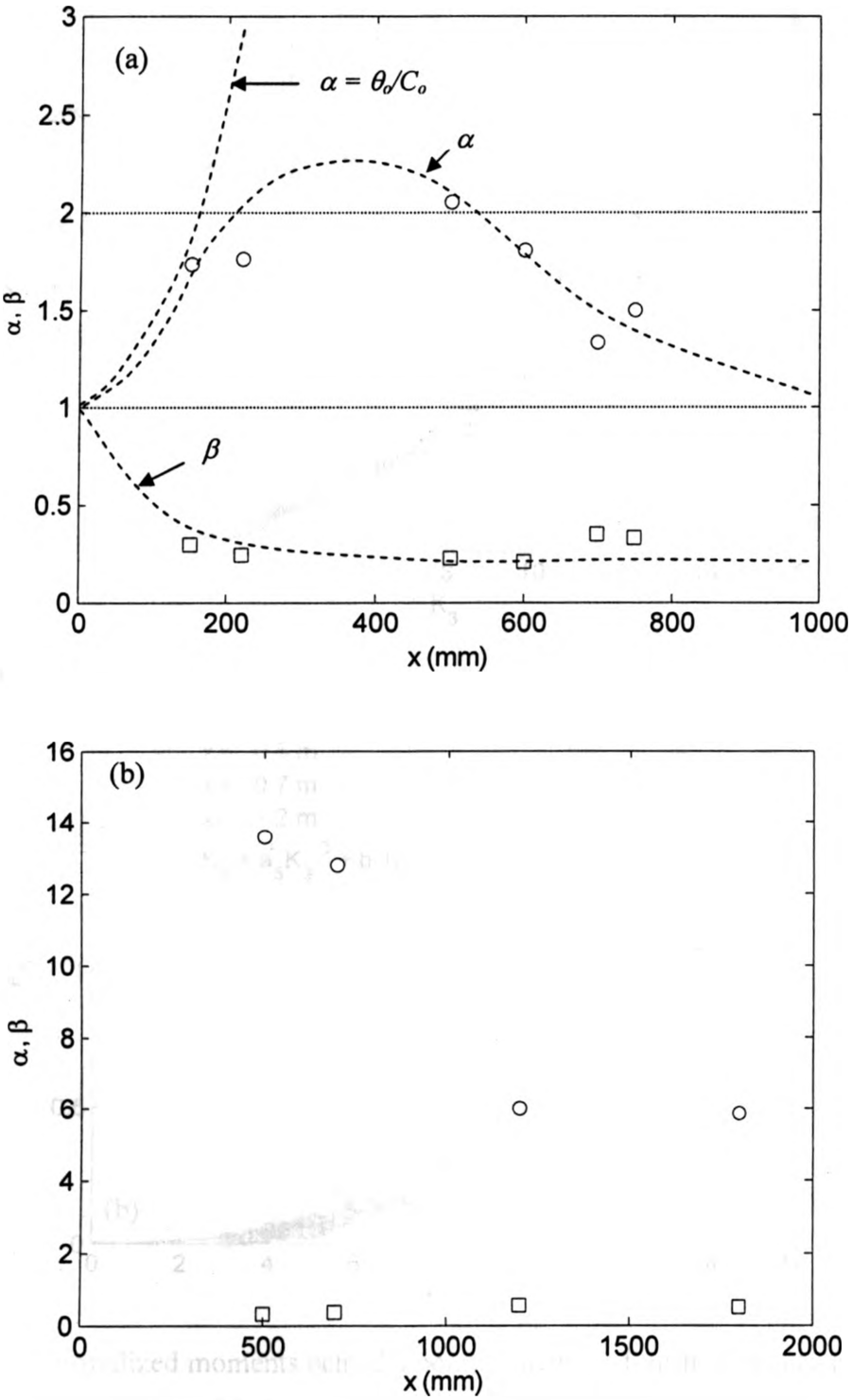

Figure 3.25: Development of α (o), β (□) with distance behind (a) a line source, (b) a point source. Dotted lines are the qualitative behavior suggested by Chatwin and Sullivan (1990).

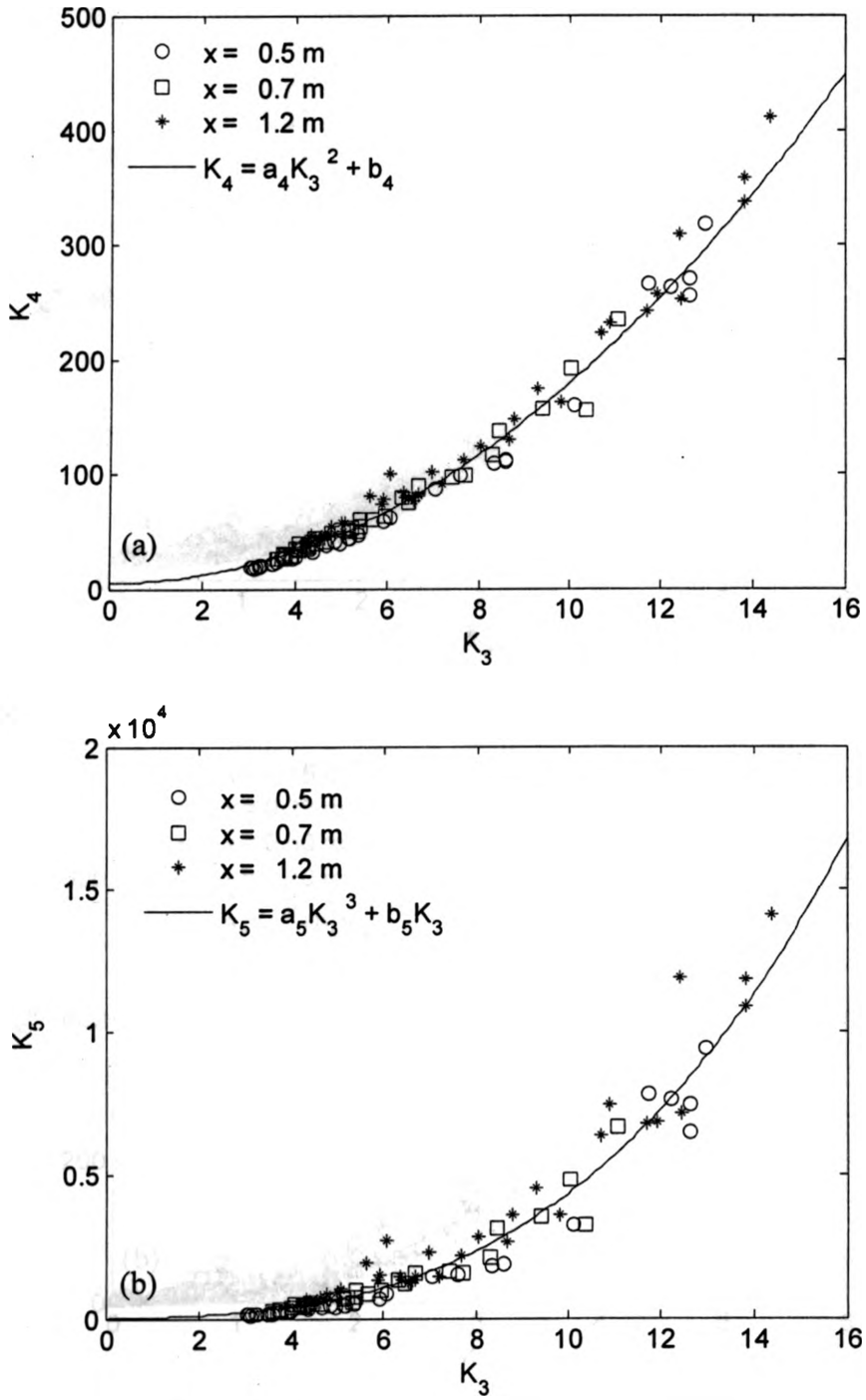

Figure 3.26: Normalized moments behind a point source; (a) fourth moments and (b) fifth moments. The solid lines represent the least squares fit of the equations shown to the legends using all the locations. (The ranges of the coefficients were calculated using individual location, such as $1.64 < a_4 < 1.78$; $1.45 < b_4 < 8.9$; $3.6 < a_5 < 4.1$; $3.2 < b_5 < 79.0$)

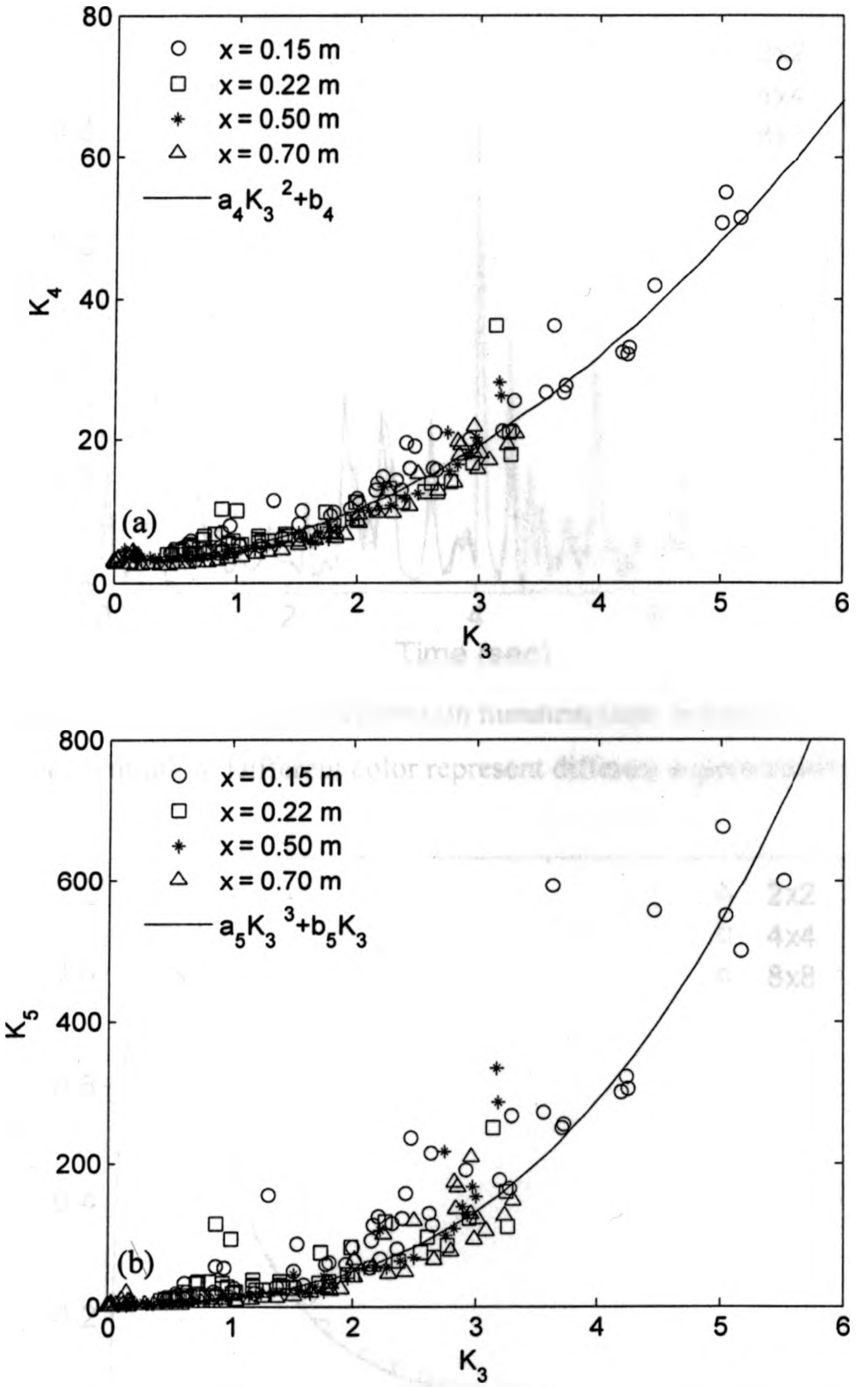

Figure 3.27: Normalized moments behind a line source; (a) fourth moments and (b) fifth moments. The solid lines represent the least squares fit of the equations shown to the legends using all the locations. (The ranges of the coefficients were calculated using individual location, such as $1.6 < a_4 < 1.95$; $2.7 < b_4 < 3.8$; $4.0 < a_5 < 5.6$; $4.3 < b_5 < 15.7$)

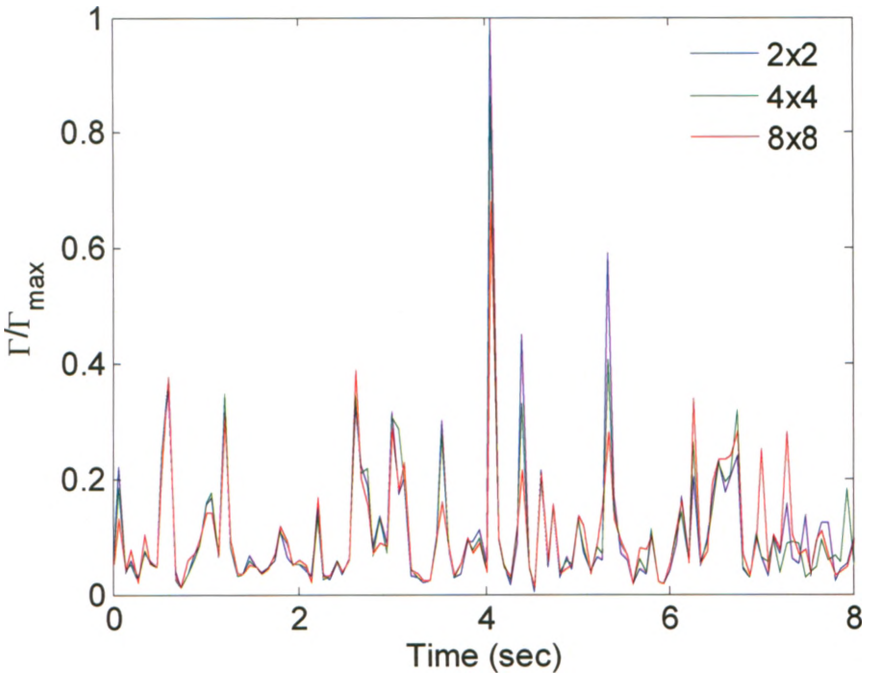

Figure 3.28: Time series of the concentration measurements normalized by the observed maximum concentration. Different color represent different supersampling dimensions.

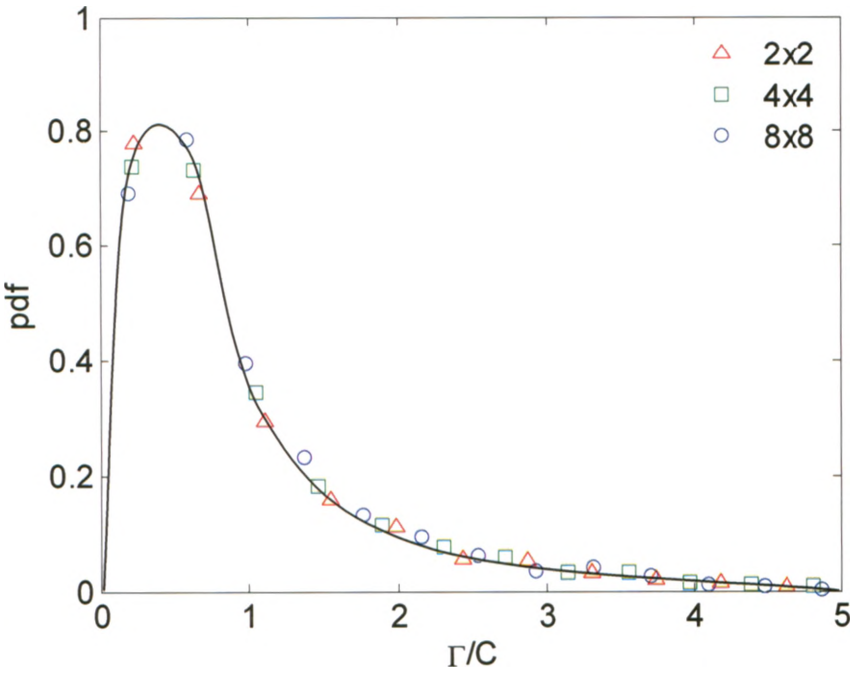

Figure 3.29: Probability density functions of the concentration measurements for different supersampling dimensions.

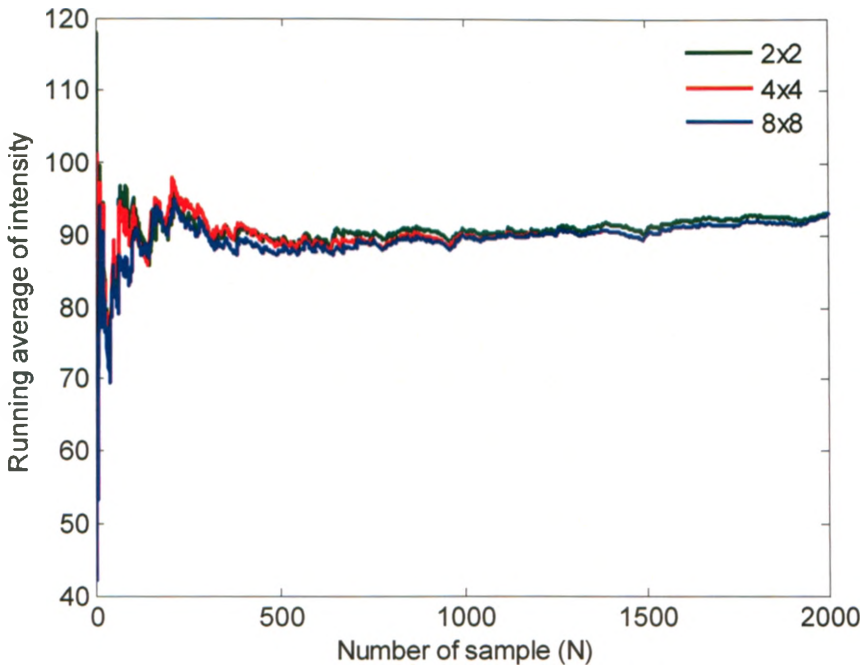

Figure 3.30: Convergence in ensemble average of concentration measurements for different supersampling dimensions.

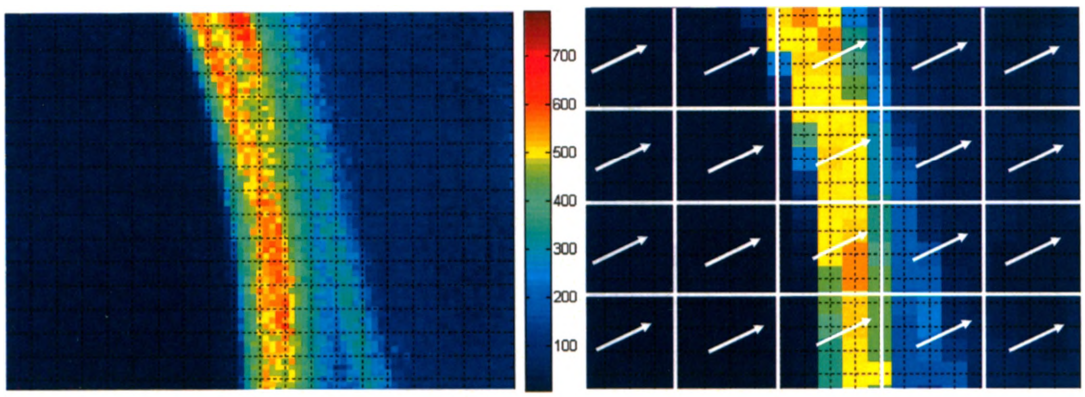

Figure 3.31: (a) A sample of a raw PLIF image showing a scalar filament; (b) the same image as (a) with averaged intensity over a 4 x 4 pixel array with a qualitative velocity map on it.

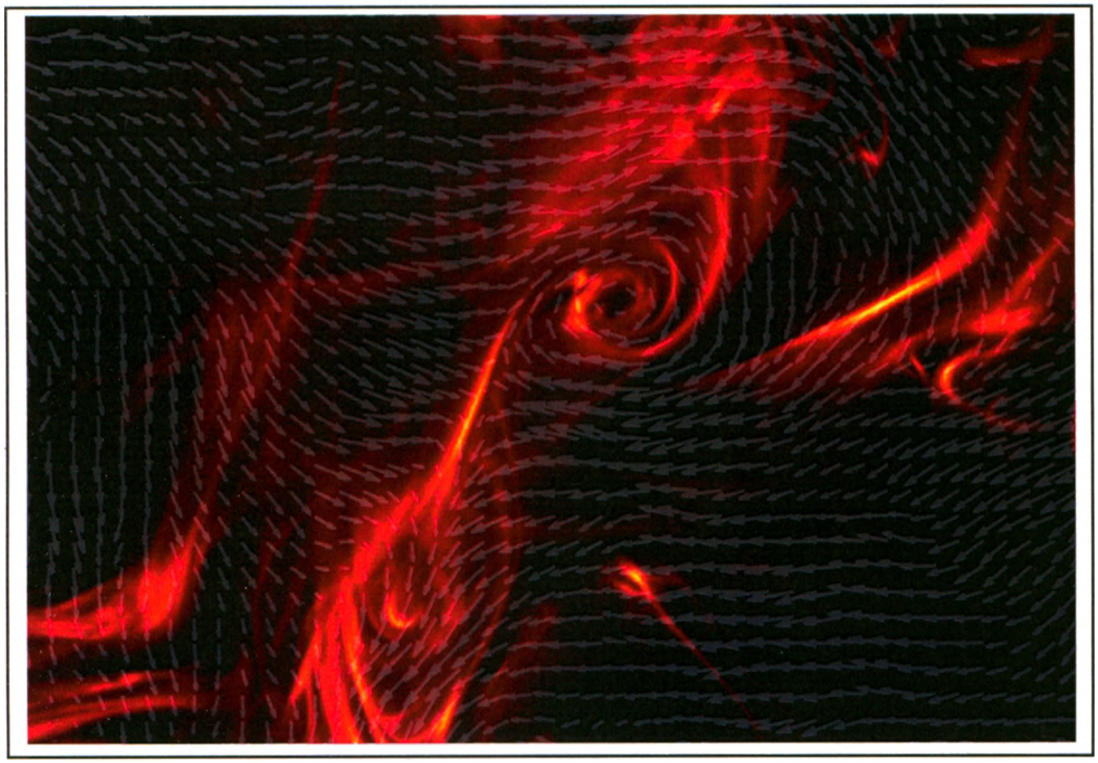

Figure 3.32: Simultaneous measurements of fluctuating velocity and concentration fields using PIV and PLIF.

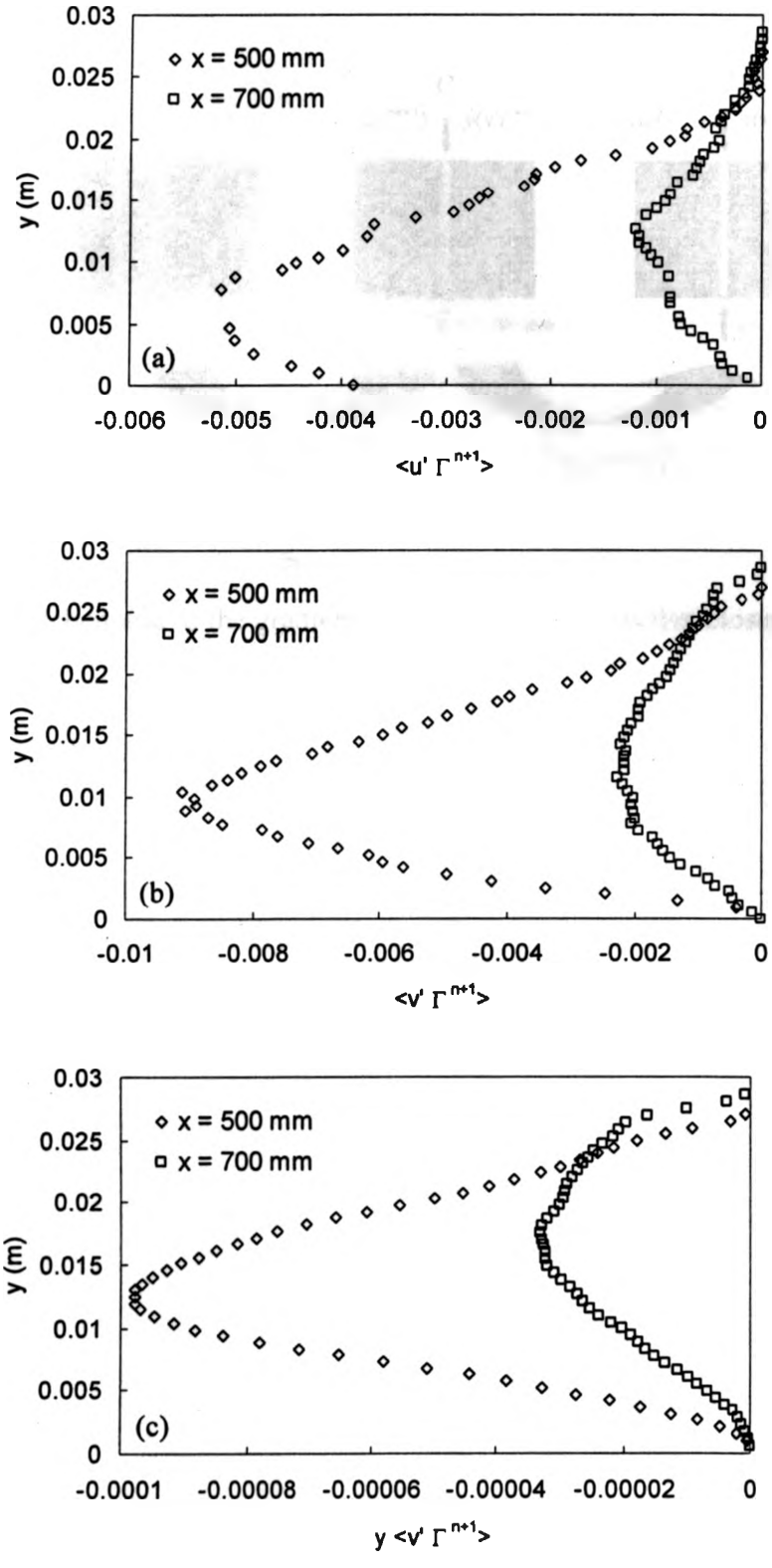

Figure 3.33: Concentration flux profiles fro $n = 1$ behind the point source; (a) $\langle u'\Gamma^{n+1}\rangle$, (b) $\langle v'\Gamma^{n+1}\rangle$; (c) $y\langle v'\Gamma^{n+1}\rangle$.

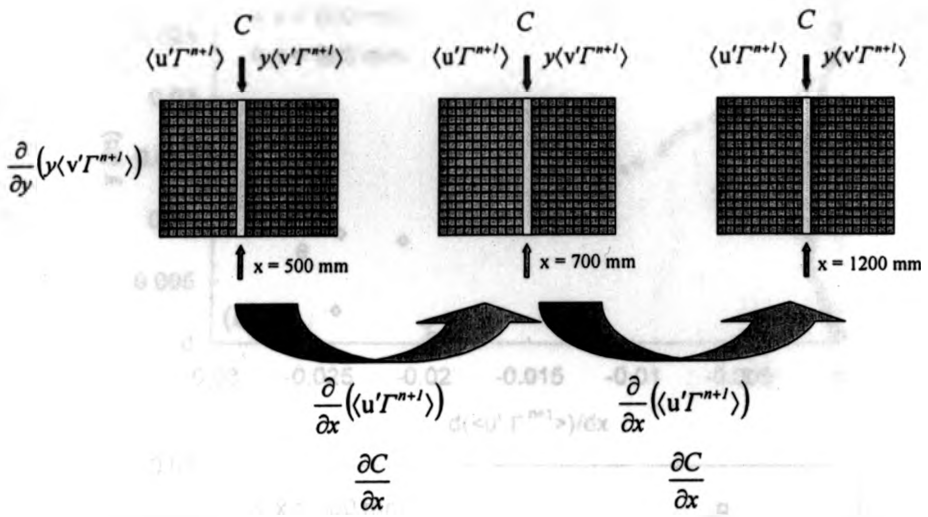

Figure 3.34: Schematic of the gradient calculation for convective closure validation.

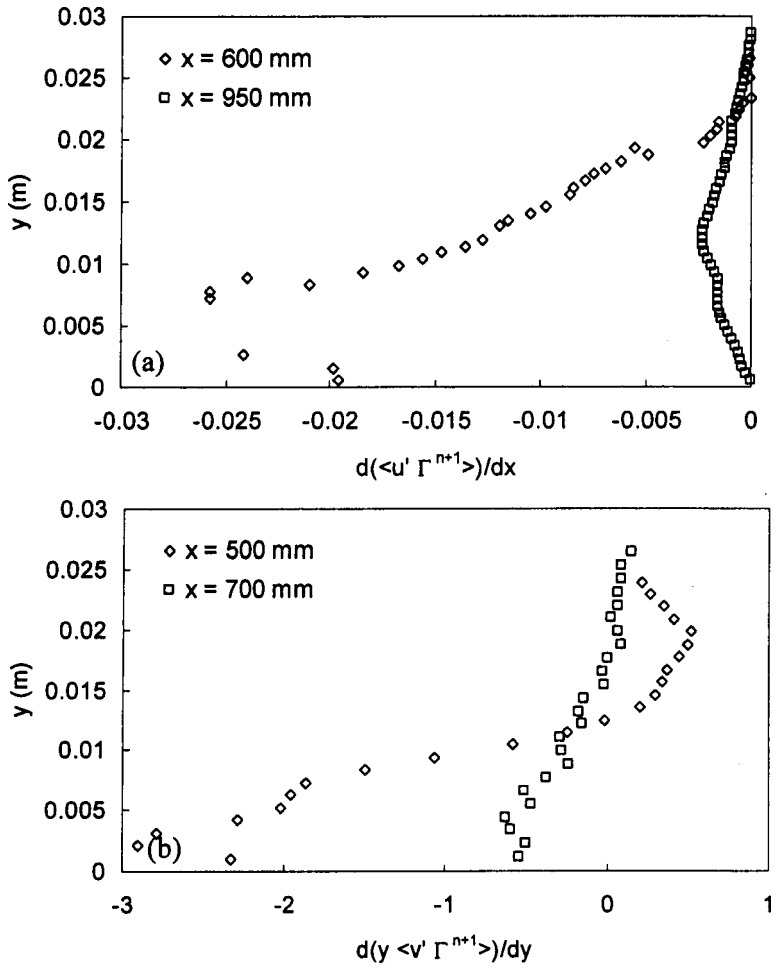

Figure 3.35: Gradients of concentration flux terms for $n = 1$ behind the point source.

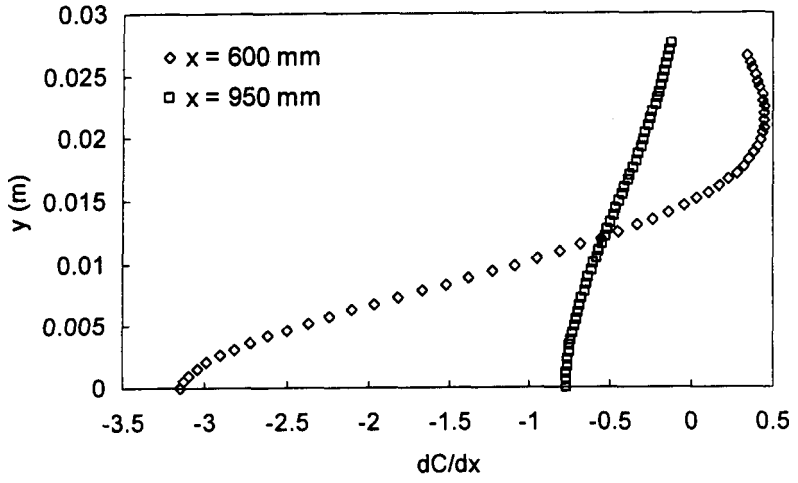

Figure 3.36: Streamwise gradients of mean concentration profiles behind the point source.

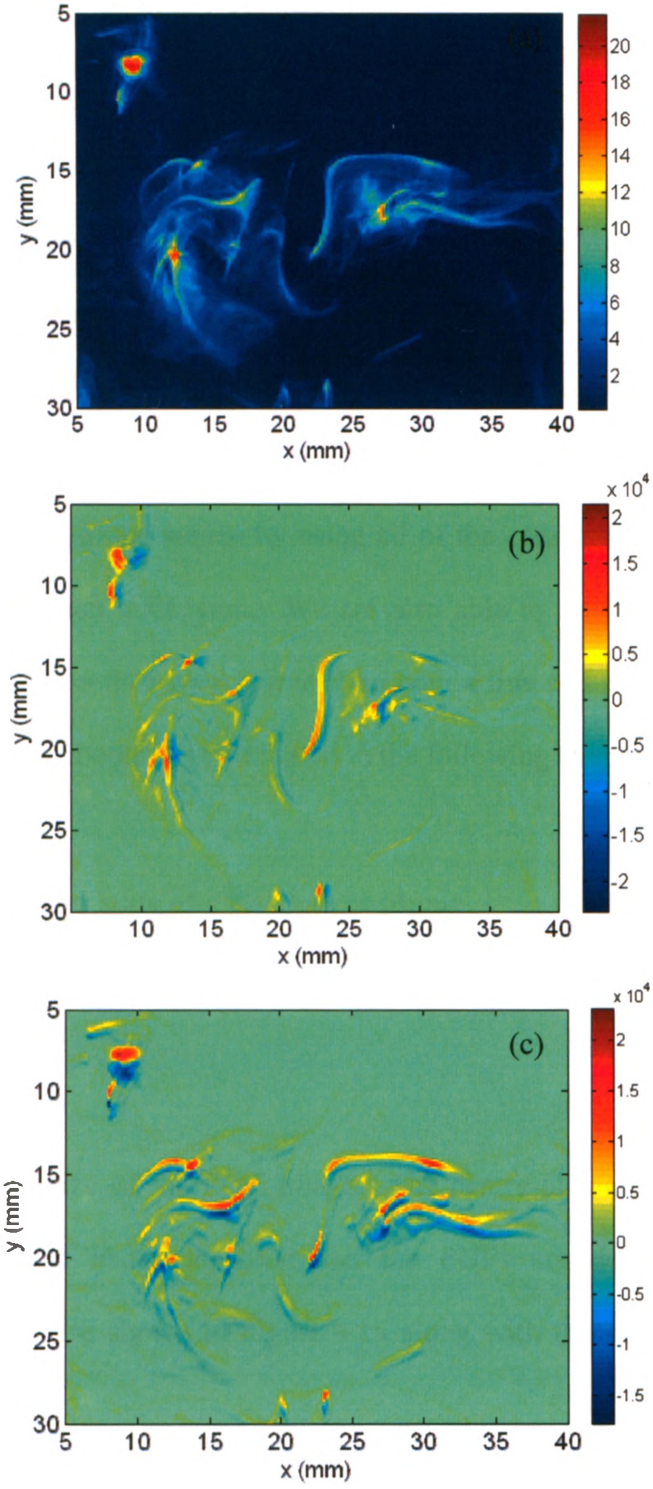

Figure 3.37: (a) concentration ($\mu g/l$), (b) $d\Gamma/dx$ and (c) $d\Gamma/dy$ of a single PLIF image.

Chapter 4: Experimental Results

4.1 Introduction

Although one would like to directly measure the EMF in a cloud, current technology does not enable this. For a cloud one would need the entire concentration field in each realization. For the equivalent in a steady plume one would require all of the values of concentration over an entire cross-section in each realization. Here, we are able to measure the EMF for a line source by using all of the concentration values on a line through the plume in each realization. We are also able to measure the simultaneous velocity and concentration through a plume from both a line and a point source. Results will be presented in this chapter and discussed in the following chapter.

4.2 Location, size and state of a line source plume

The location of the centre-of-mass in each realization is expressed as

$$\bar{y} = \frac{\sum y\Gamma dy}{\sum \Gamma dy}, \tag{4.1}$$

where, dy is the pixel size of the PLIF images. The centre-of-mass is calculated for a pixel column using the above equation and the PDFs are developed using 4000 realizations. The PDFs are shown in Figure 4.1a along with the reference Gaussian fit (continuous lines).

In Figure 4.1b, the PDFs of the variance of plume cross-section, as compiled in each realization, are shown. The variance is expressed as,

$$\sigma = \left(\frac{\sum (y - \bar{y})^2 \Gamma dy}{\sum \Gamma dy} \right)^{1/2}. \tag{4.2}$$

The PDFs in Figure 4.1b is also compared with the reference Gaussian fit. The values of spatial variance are governed by turbulent velocity scales comparable with the plume size, which for large Reynolds numbers, are statistically decoupled from the larger scales that govern in Figure 4.1a. In practical terms, one may wish to combine the centre-of-mass location and variance into one statistic – the probability of being in marked fluid, which is generally, to a good approximation, $\pi(x,t) = C(x,t)/\theta_o$, shown in Chapter 3 (Figure 3.24a), for an initial uniform concentration, θ_o. Sullivan and Ye (1995) provides such an analysis for the neutral atmospheric boundary layer.

In order to calculate the EMF, each PLIF image is considered as a two-dimensional array of concentration measurement. A vertical column is chosen from the same location of each PLIF image and for one realization is used to calculated the EMF (Figure 4.2) as

$$EMF(\theta) = \frac{\theta \sum \Delta y_i}{\overline{Q}}, \tag{4.3}$$

where $\overline{Q} = \frac{1}{N} \sum \left(\theta \sum \Delta y_i \right)$, $\Gamma < \theta \leq \Gamma + \Delta\Gamma$ and Δy is the pixel size. The $\Sigma \Delta y_i$ corresponds to the total number of pixels in the vertical pixel column that contain the concentration within the specific range given as θ. The mass fractions are averaged over number of realizations (N). Figure 4.3 shows the evolution of the EMF as one proceeds downstream. These relatively simple functions are very similar to those generated by a Gaussian strand model and shown in Sullivan and Ye (1997) and from point measurements in a line

source in grid turbulence in Sullivan and Ye (1993). The effect of molecular diffusion in reducing contaminant concentration is clearly in evidence in Figure 4.3 as the area under the EMF migrates to lower values of concentration as one goes downstream. The most important scales for the concentration reduction are near the conduction cut-off length (i.e., the Batchelor scale) that are much smaller than scales contributing to the centre-of-mass shown in Figure 4.1a and to the spatial variance shown in Figure 4.1b.

In Figures 4.4, the root-mean-square (RMS) values are shown at each concentration interval for the EMF. The RMS values are relatively small when one considers the fact that the EMF realizations are taken over one thin line through the plume. One would expect even relatively smaller values for a point source plume or cloud when all the values of concentration over the entire cross-section of the plume or throughout the cloud, respectively, are used in each realization.

In Figure 4.5, the EMF functions are compared with a simple Beta distribution as suggested in Schopflocher et al. (2007). Here a less demanding procedure is used to fit the Beta distribution function wherein a scale larger than the anticipated maximum is chosen and only the first two moments of the EMF are used. Example of scale choices of $2C_o$ and $3C_o$ are shown in Figures 4.5. Although the simple Beta function does not provide a convincing close fit to the data, taking into account the measurement error, the simple Beta function may be an appropriate representation in a practical point of view. That is, precise source and flow details are not likely to be available for an accidental release of contaminant. Unfortunately, as discussed in Chapter 3, one does not have

sufficient confidence in measured higher moments to investigate the Generalized Pareto Density function application to this range, as discussed in Chapter 2.

One further application on the curves in Figures 4.5 is that the Beta function found from the average values of the first and second moments (see Table 5.1), formerly used for the Beta function fit, provides an almost similar representation. It would appear that when concentration values are normalized with C_o an approximately self-similar result is obtained. This result also appears to be applicable from the figures in Schopflocher et al. (2007), which were indirectly derived from the α–β measurements as discussed in Chapter 2. In Figure 4.6, the measured value of the EMF moments are compared with the exponential fits. In Section 5.2, power law fits are also discussed.

4.3 Convective closure approximation

The appropriate terms for the convective closure approximations (equations (2.53) and (2.54) in Chapter 2) are shown in Figures 4.7 - 4.12 for three lower order moments at three locations behind a point source and a line source. Although there is some inevitable scatter around the linear dependence in the figures, particularly as n increases, the trends appear to validate the assumptions made. The diagrams with higher n values (>3) are not shown because of the larger experimental uncertainties involved in the calculation of the products in (2.53). The slopes, $S/U(\theta_o^*)^n$, of the straight lines in Figures 4.6 - 4.12 are shown on Figures 4.13. At all locations it is clear that the logarithm of the slope is linearly dependent on moment order n. The value of the local concentration scale θ_o^* is determined from Figure 4.13a and those

values are compared in Figure 4.14 with the centreline mean concentration values behind a point source. Here, the local concentration scale, θ_o^*, is shown from the point source measurements only. For the line source measurements, the calculated terms of (2.53) within one measurement plane do not change significantly, and on the other hand, the change between two measurement planes is significantly high, which results a discrepancy in measuring θ_o^*. Figure 4.14 indicates a variation of the form $\theta_o^* = 14.94\, e^{-0.84x}$ with downstream distance, where x is in meters.

The exact expression for the moments when $\kappa = 0$ is $m_{n+1} = \theta_o^n C$ for the uniform source concentration θ_o. When modified to account for $\kappa \neq 0$ by the use of a local concentration scale (depends on distance only) and proportionality factor, B_n, also only a function of distance, we have

$$m_{n+1} = B_n \left(\theta_o^+\right)^n C, \tag{4.4}$$

which will be discussed in Chapter 5.

Measured values of the moments (Table 4.1) along the centreline are shown in Figures 4.15 and appear to be of the form (4.4) at each station. It is clear in the figures that at each station the logarithm of the moments depends linearly on n. The local concentration scales (θ_o^+) found from the slopes in Figures 4.15 are plotted with downstream distance in Figure 4.16 and are found to follow an exponential form with the distance ($\theta_o^+ = 13.34\, e^{-1.21x}$ for the point source and $\theta_o^+ = 0.94\, e^{-1.58x}$ for the line source). Power law fits of local concentration scales are also discussed in Section 5.2.

Table 4.1: Summary of centreline absolute moments

	x (m)	C_o (μg/l)	m_2/C_o^2	m_3/C_o^3	$m_4//C_o^4$	α	β	θ_o^+ (μg/l)
Line Source	0.15	0.71	1.07	1.20	1.42	1.72	0.81	0.82
	0.19	0.65	1.04	1.13	1.29	1.79	0.8	0.72
	0.22	0.56	1.02	1.14	1.22	1.9	0.8	0.62
	0.5	0.34	1.04	1.27	1.50	2.5	0.19	0.38
	0.6	0.32	1.07	1.22	0.95	1.84	0.21	0.35
	0.7	0.29	1.07	1.23	1.41	1.38	0.34	0.32
	0.75	0.28	1.02	1.37	1.63	1.4	0.35	0.32
Point Source	0.5	1.69	2.08	8.33	49.77	13.6	0.32	8.17
	0.7	0.91	2.15	9.58	72.48	12.8	0.33	5.26
	1.2	0.40	2.56	12.97	121.48	6	0.53	2.75
	1.8	0.23	1.51	9.04	75.04	5.85	0.5	1.63

Figures 4.17 and 4.18 show the distributed measured moments as a function of mean concentration near the centreline, where the linear dependence shown in the figure is consistent with (4.4) particularly for the point source measurements (Figure 4.17) and for the line source measurements it behaves linearly up to one spatial variance distance (Figure 4.18).

4.4 Dissipative closure approximation

The terms of the dissipative closure approximation solution (equation (2.56) in Chapter 2) are plotted for the first order of moment in Figure 4.19. The gradient terms in the dissipative solution are calculated using each scale case ($r = dx = dy$) varying from the highest experimental resolution at a particular location up to the scale larger than η. The proportionality constant, B, for different r scales are calculated from the linear plots (Figure 4.19) as

$$B = \frac{\left[\langle \Gamma^{n-1} \left(\frac{\partial \Gamma}{\partial x} \right)^2 \rangle + \langle \Gamma^{n-1} \left(\frac{\partial \Gamma}{\partial y} \right)^2 \rangle \right] \eta_B{}^2}{\langle \Gamma^{n+1} \rangle}, \tag{4.5}$$

and are averaged over space. The results are shown in Figure 4.20 with r/η, where, the Batchelor (η_B) scale at a particular location is assumed to be constant (using equation A8) but changes with location as in Table 3.1. Figure 4.20 shows two distinct self-similar regimes within the Batchelor scale and the Integral scale, separated by the Kolmogorov scale. The dimensions (i.e., the slope of the self-similar zone) were calculated for each zone from the point source measurements and it was found that the dimension in the *K*-zone has a tendency to follow the -5/3 slope for the first order of moment ($n = 1$). That is, it appeared to be similar to the scaling of the passive scalar spectrum in the inertial-convective regime (i.e., the Kolmogorov -5/3 slope). A different dimension of scaling is observed in the line source measurements in the *K*-zone, which is believed to be the result of low Reynolds number flow and coarse experimental resolutions. Figure 4.21 shows the scaling for different orders of moment. The scaling of the proportionality constant in the *K*-range (viscous-convective regime) is used to extrapolate the constants at the η_B scale. Figure 4.22 is plotted using the extrapolated proportionality constants at the Batchelor scale, B (η_B), with distances downstream.

The resolution in the measurements behind the line source is of the order of the Kolmogorov length scale, which hinders one from having a proper scaling in the *B*-zone. An attempt is made here to draw a relationship between the dimensions (D_K and D_B) in the *K*-zone and the *B*-zone. Figures 4.23 show the variation of the dimensions in the *K*-

zone and the B-zone with Taylor micro-scale Reynolds number. It does not appear that the dimensions vary strongly with Taylor micro-scale Reynolds number (Re_λ), at least at low Reynolds numbers obtained in the present study. However, the trends in Figure 4.23b show an inverse dependence of D_B on Re_λ powered by one fifth. A scaling is developed in order to predict D_B by using Re_λ and D_K based on the point source measurements, that is,

$$D_B = 0.071 \frac{D_K^{2.7}}{\mathbf{Re}_\lambda^{0.2}} + 0.65, \tag{4.6}$$

which is shown in Figure 4.24, and the coefficients are determined based on the best fit straight line. It has been assumed that a similar scaling would exist in measurements behind the line source. Using the scaling in (4.6) Figures 4.25 are constructed, where the proportionality constants (B) in B-zone are plotted against different scale r. The figures also show the measured B values in K-zone for three moments. In order to get a proper scaling between the K-zone and the B-zone, one would need to have a flow with higher Reynolds number than the present study. However, the attempt that is made here sheds light on dealing with the scaling between two self-similar zones.

4.5 EMF along a radius of an axisymmetric plume

An attempt is also made here to calculate the EMF functions along a radius of a plume behind the point source. The concentration measurements of the point source that were used for closure validations are used here. The EMF function with the root-mean-square (RMS) values at each concentration interval are shown in Figure 4.26. Figure 4.27 shows the self-similar EMF functions when an appropriate scale ($10C_o$) has been chosen.

A Beta distribution function using the average moments of the normalized EMF functions is shown also in the figure.

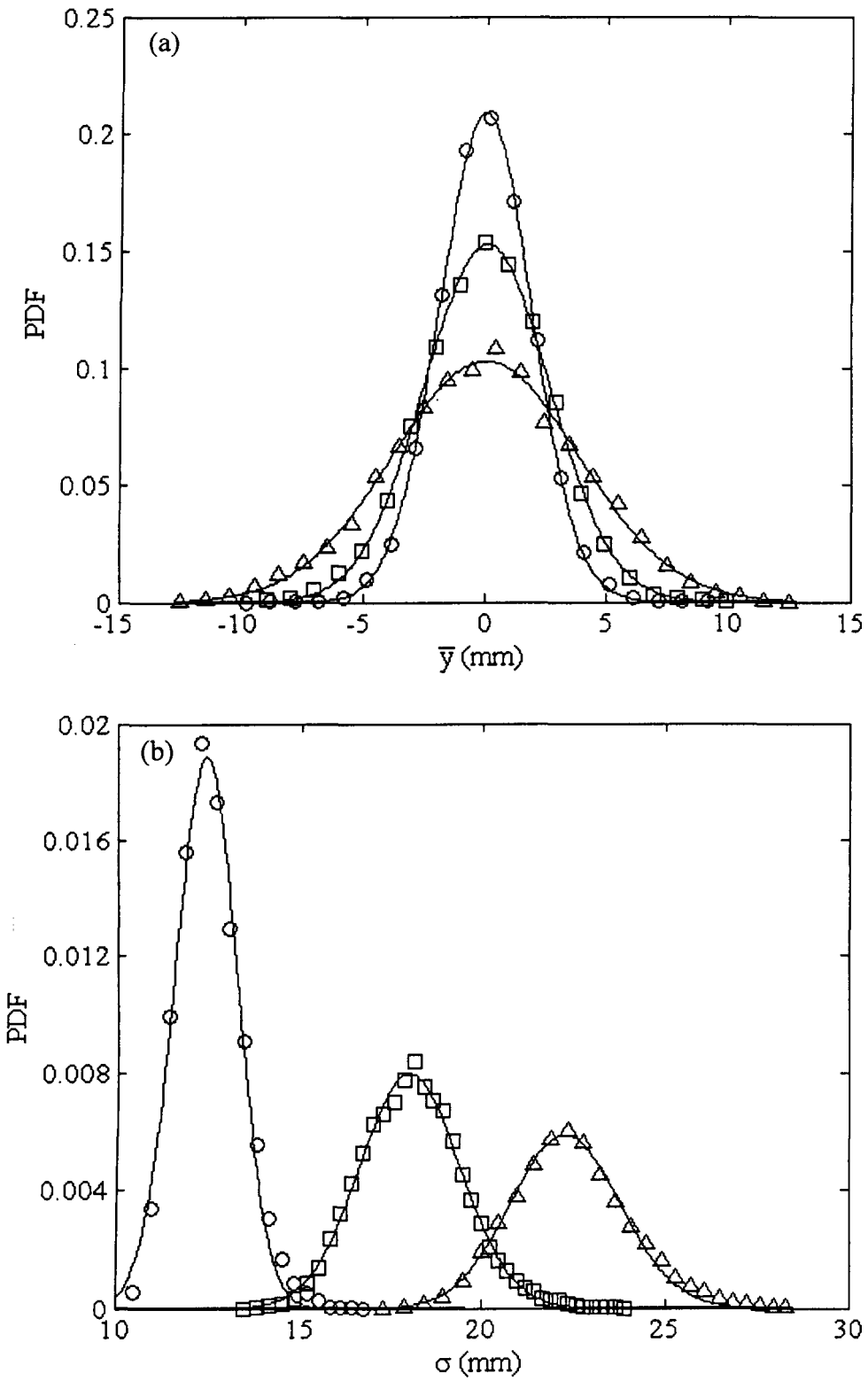

Figure 4.1: (a) PDF of the location of centre-of-mass; (b) PDF of the spatial variance, (o) x = 0.15 m, (□) x = 0.5 m, (Δ) x = 0.7 m. (Continuous lines are best fit Gaussian curves).

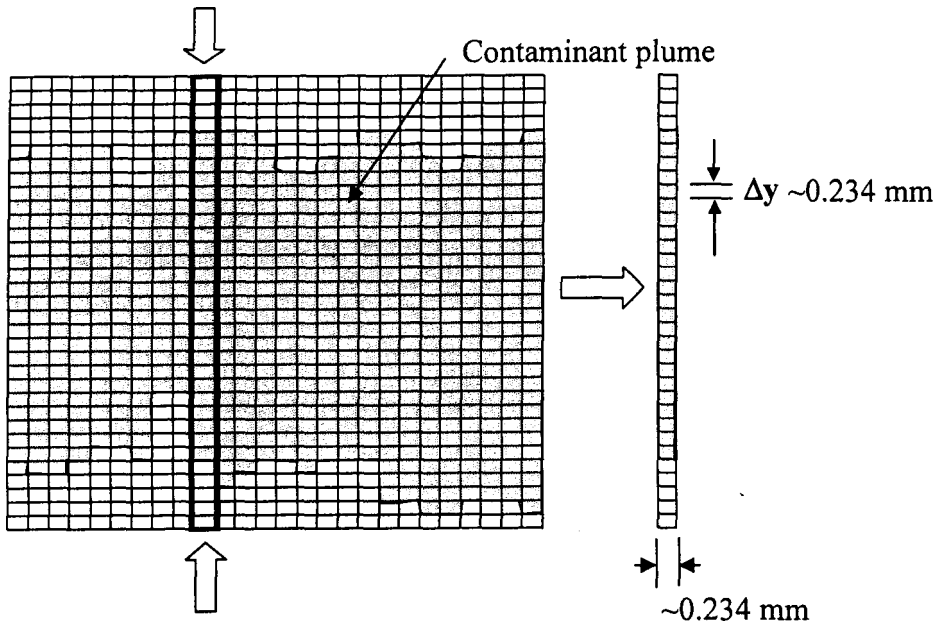

Figure 4.2: Schematic of the EMF calculation from the centreline measurements of a point source plume (an example of the pixel size at x = 0.15 m location is shown here).

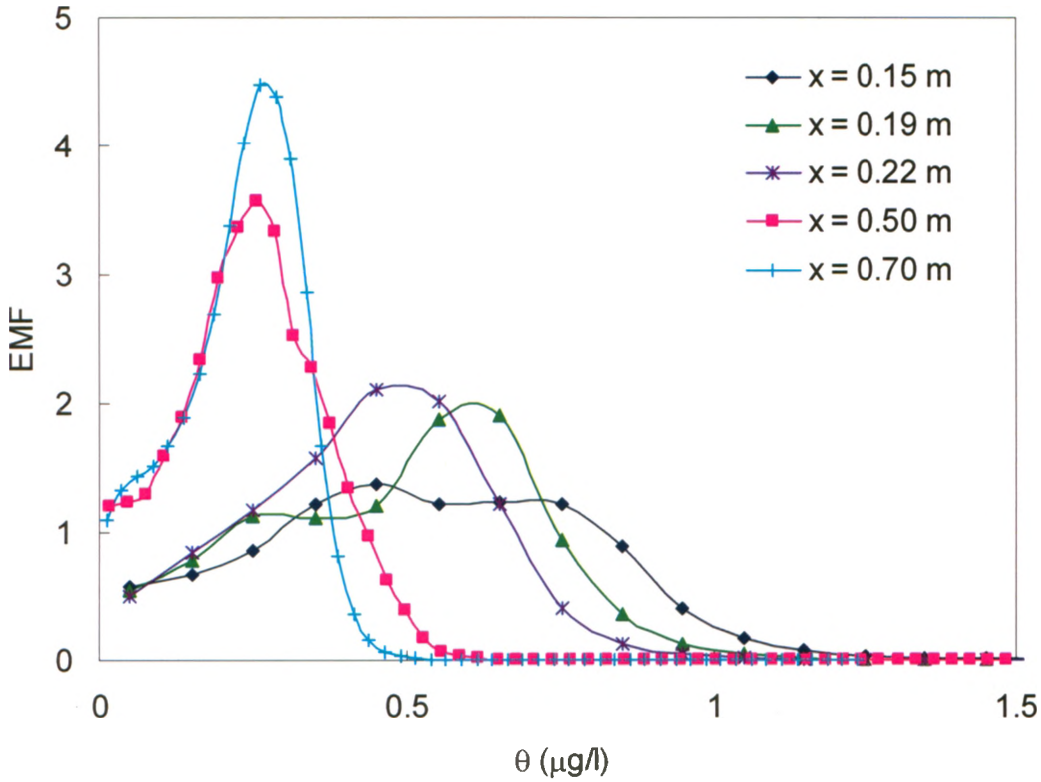

Figure 4.3: Expected Mass Fraction (EMF) with downstream distances behind the line source. The EMF migrates to lower values of concentration downstream distance.

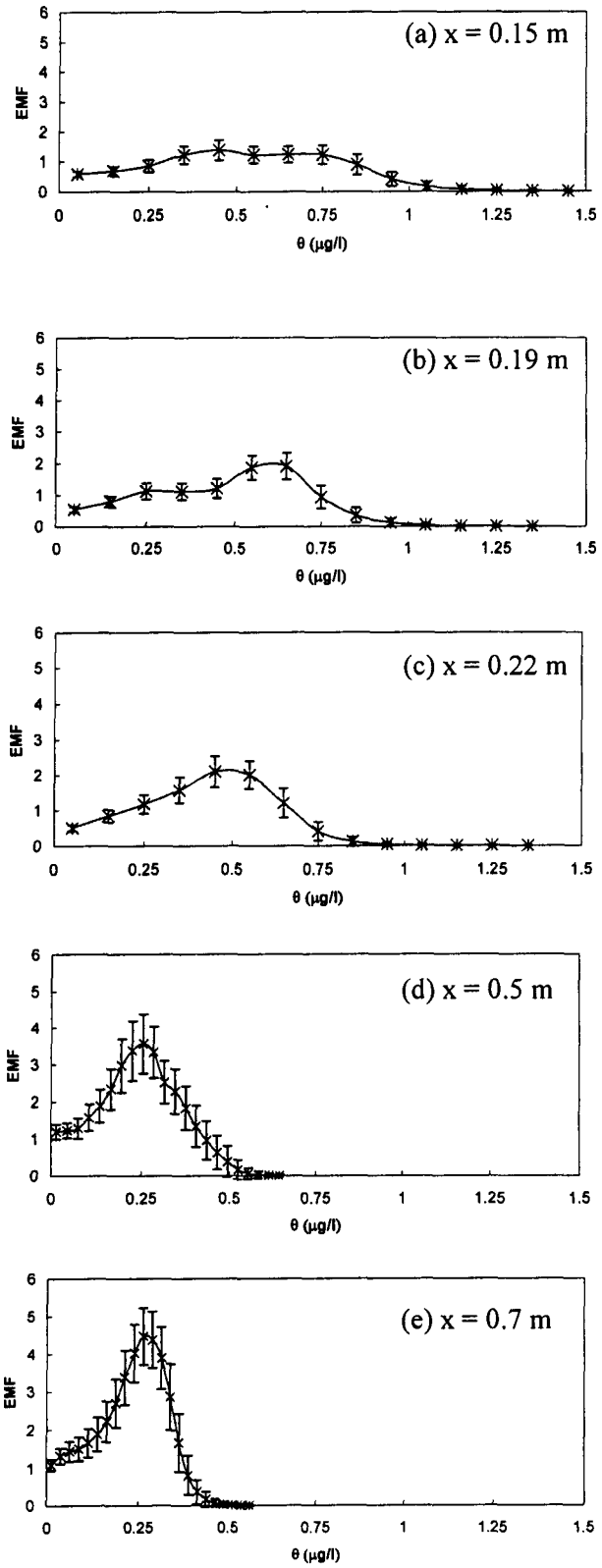

Figure 4.4: EMF functions behind the line source are plotted for different distances, vertical bars are standard deviations.

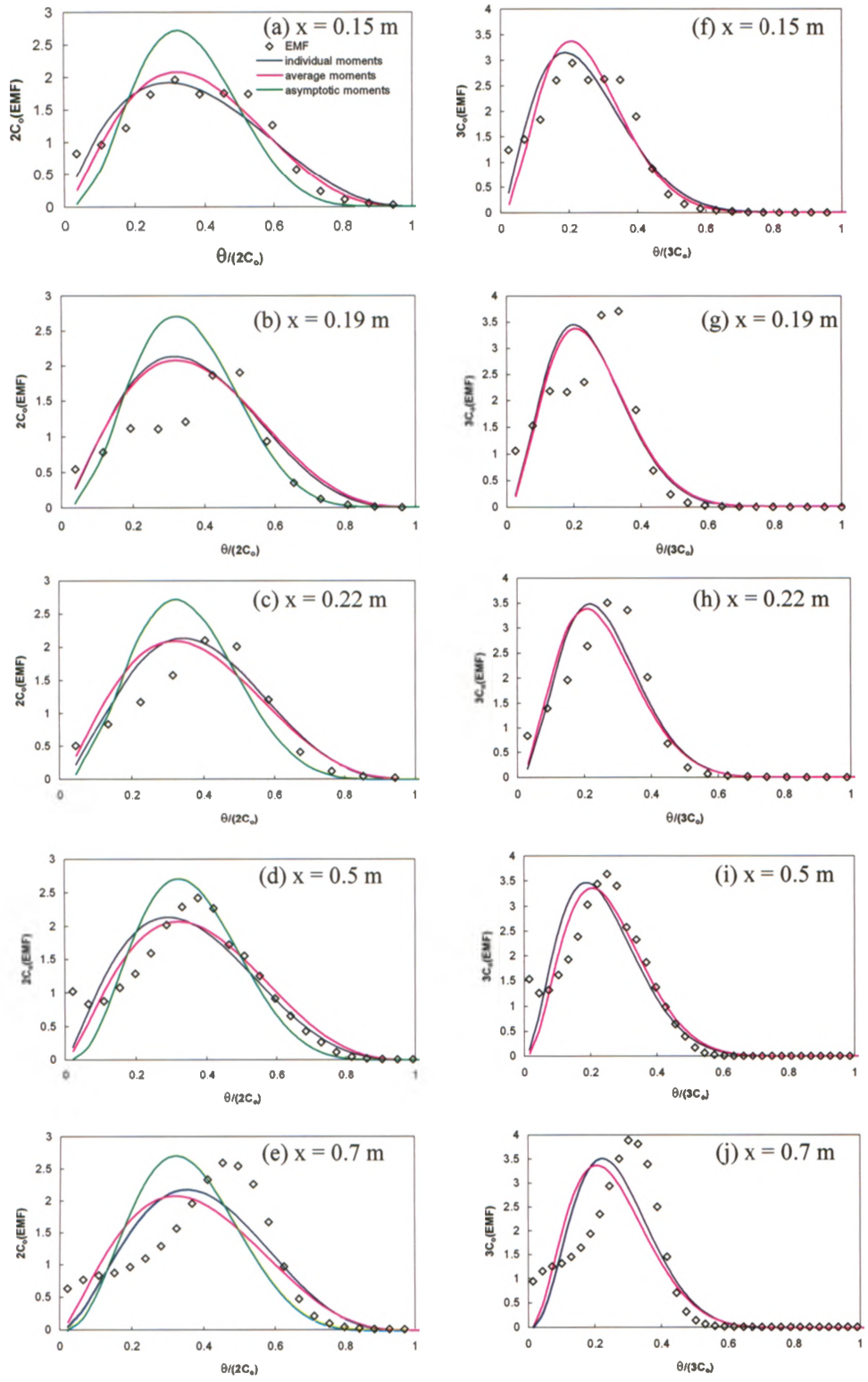

Figure 4.5: Representation of Beta functions behind the line source in order to predict the EMF. The blue lines are the Beta function using individual moments, the red lines are drawn using moments that are averaged over five locations, and green lines are asymptotic solutions using (5.25).

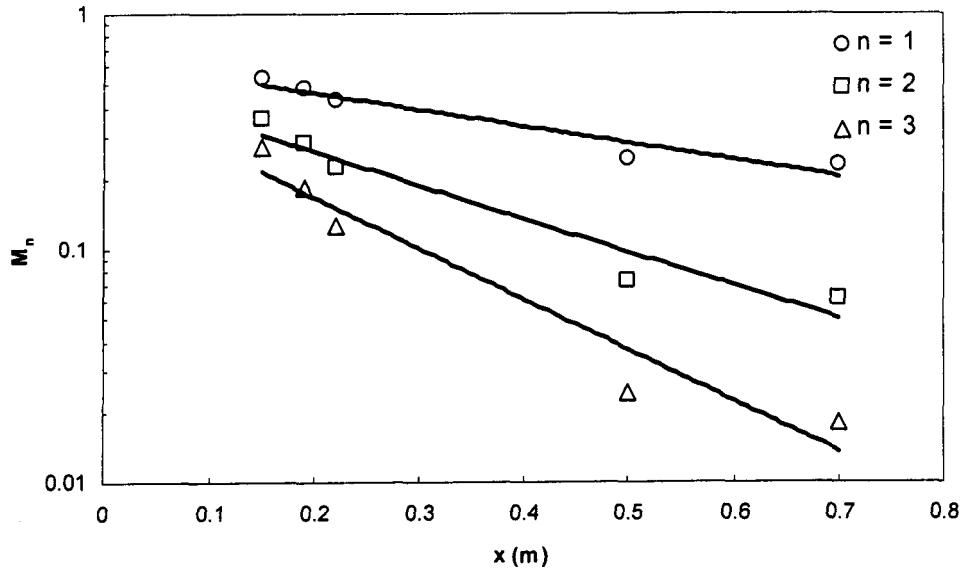

Figure 4.6: EMF moments are compared with distances behind the line source. The solid lines are the exponential fits. A 'power law' representation is also discussed in Section 5.2.

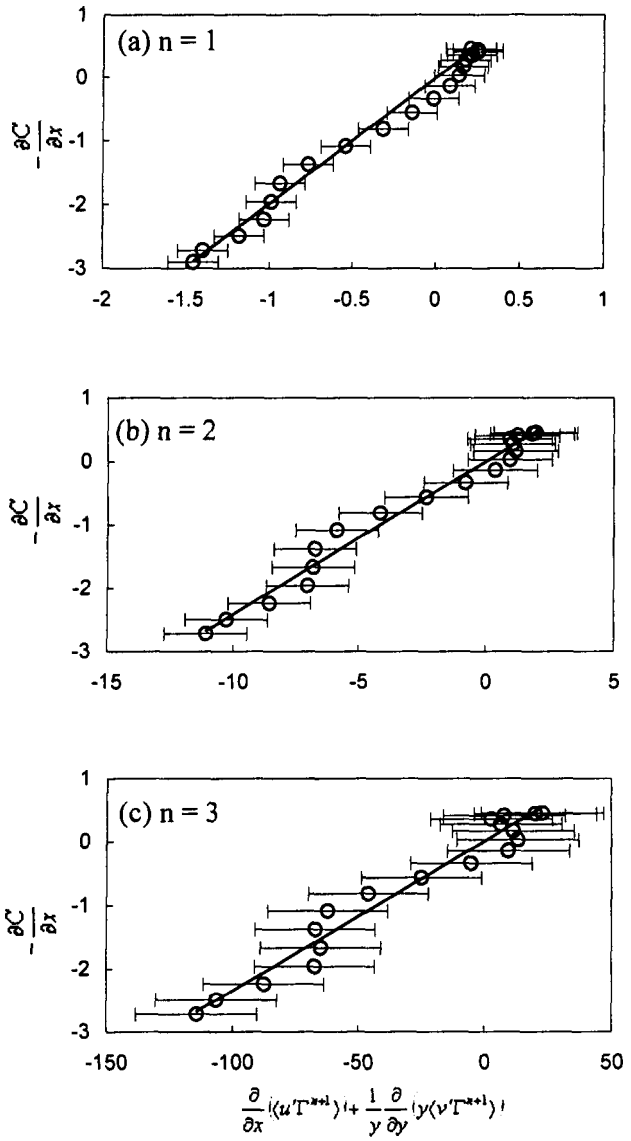

Figure 4.7: Convective closure approximations behind a point source at a distance 0.6 m downstream (horizontal bars are calculated errors).

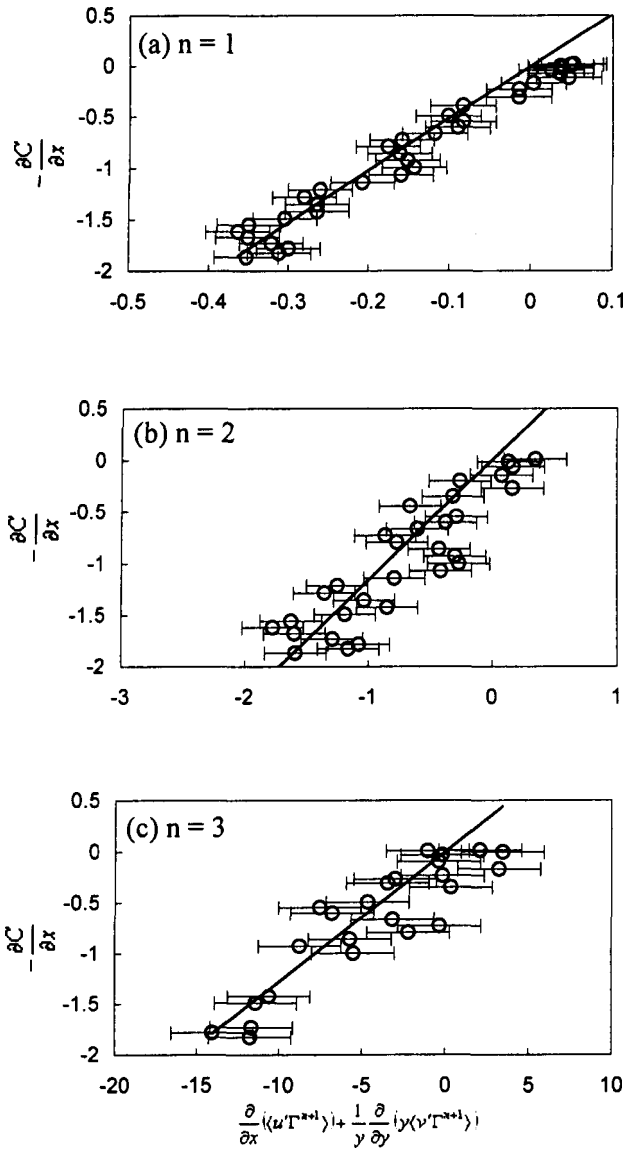

Figure 4.8: Convective closure approximations behind a point source at a distance 0.95 m downstream (horizontal bars are calculated errors).

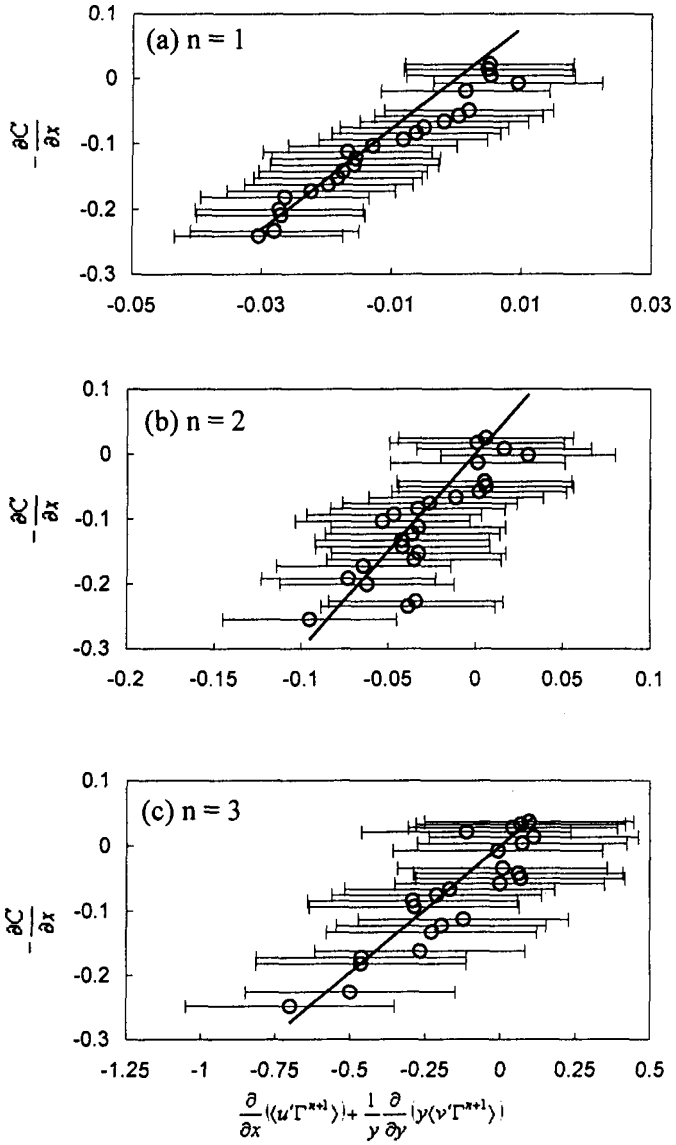

Figure 4.9: Convective closure approximations behind a point source at a distance 1.5 m downstream (horizontal bars are calculated errors).

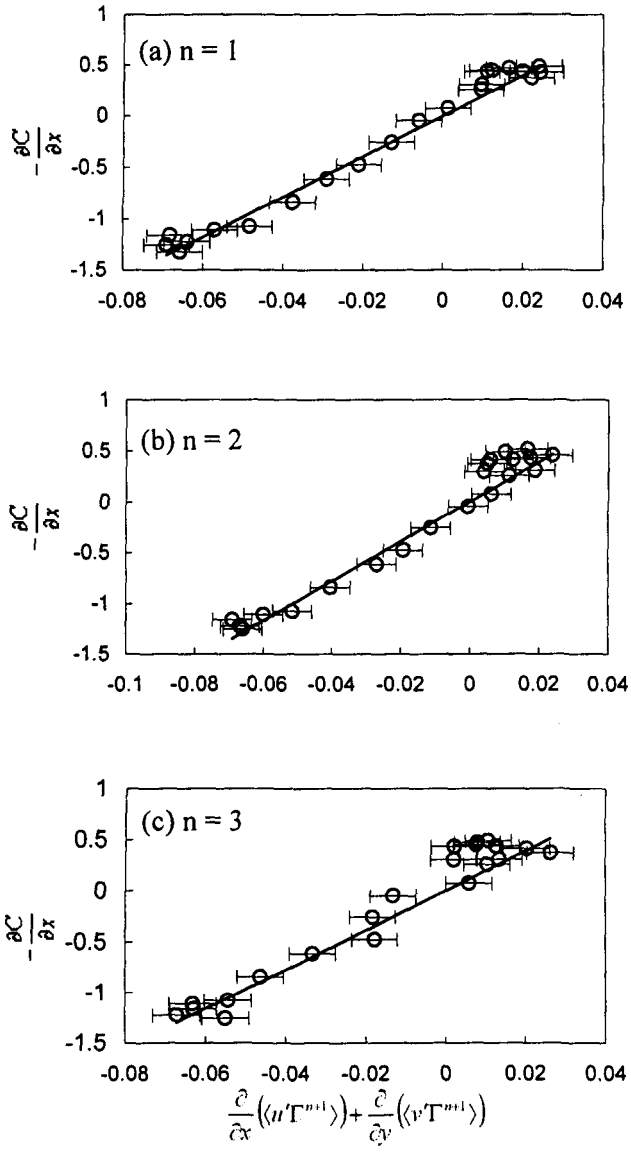

Figure 4.10: Convective closure approximations behind a line source at a distance 0.17 m downstream (horizontal bars are calculated errors).

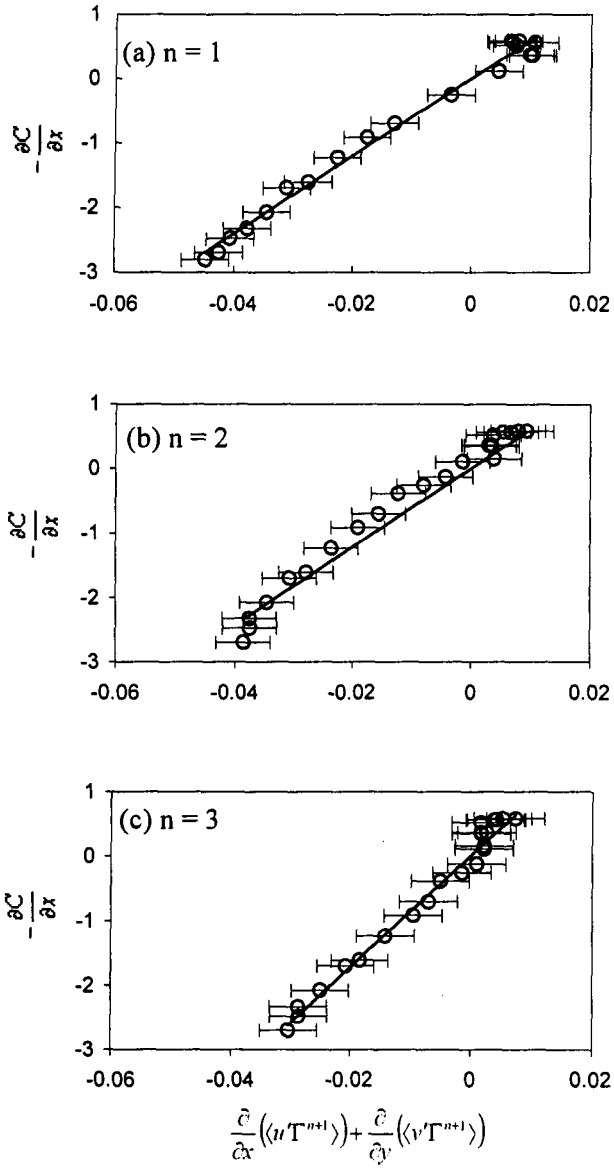

Figure 4.11: Convective closure approximations behind a line source at a distance 0.20 m downstream (horizontal bars are calculated errors).

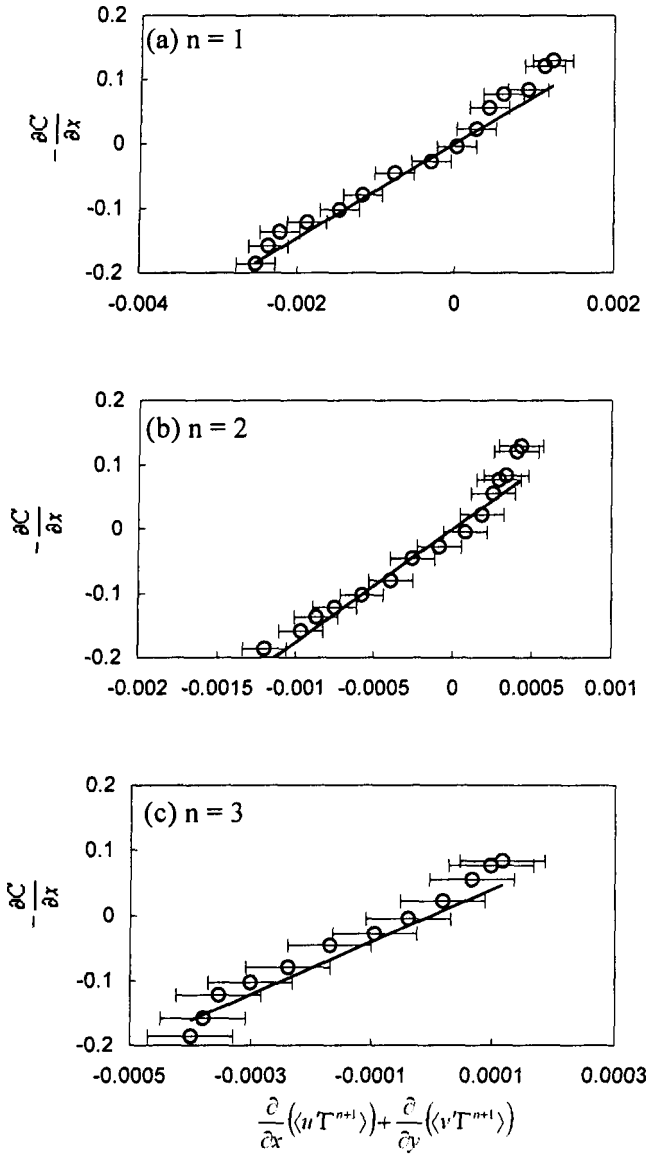

Figure 4.12: Convective closure approximations behind a line source at a distance 0.75 m downstream (horizontal bars are calculated errors).

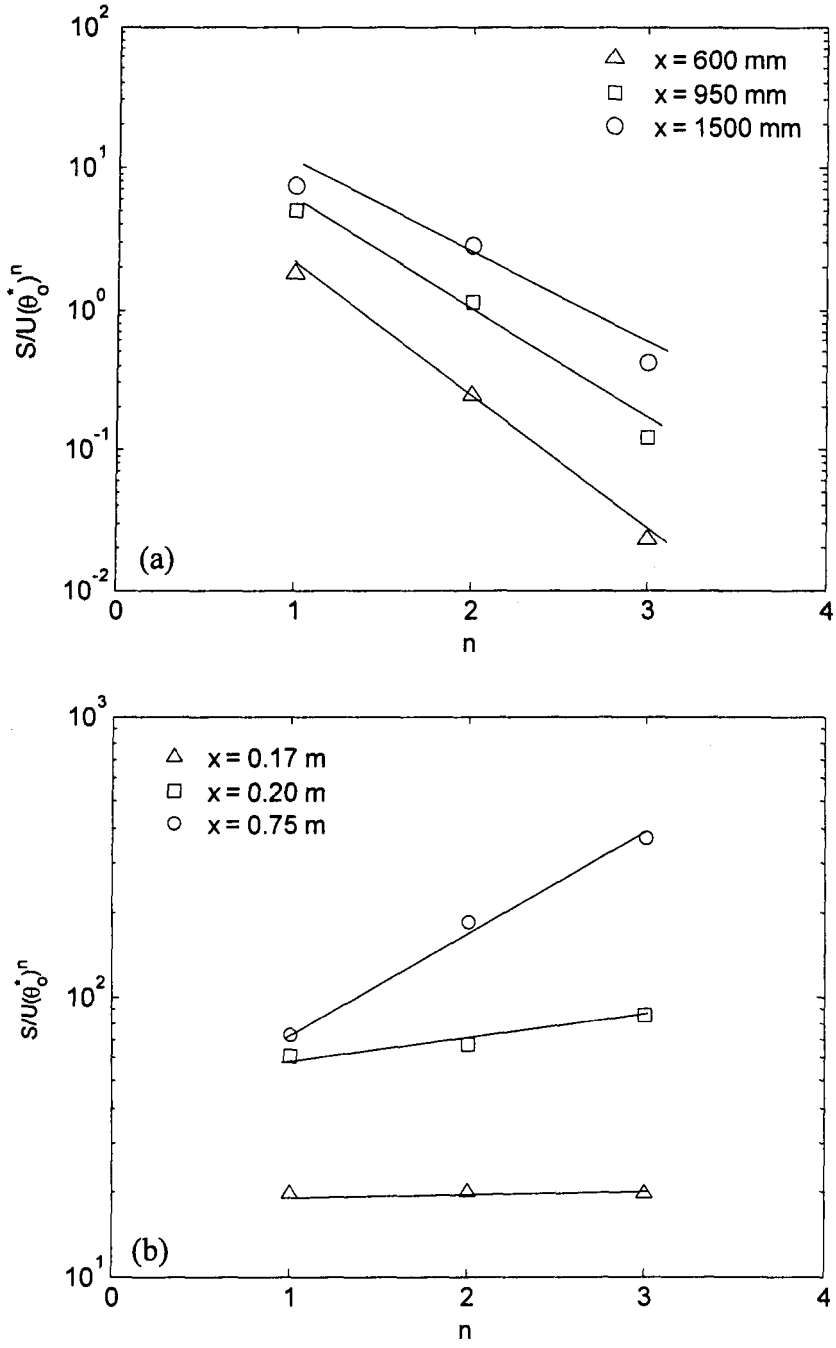

Figure 4.13: Variation of $S/U(\theta_o^*)^n$ with the order of moment behind (a) the point source, (b) the line source .

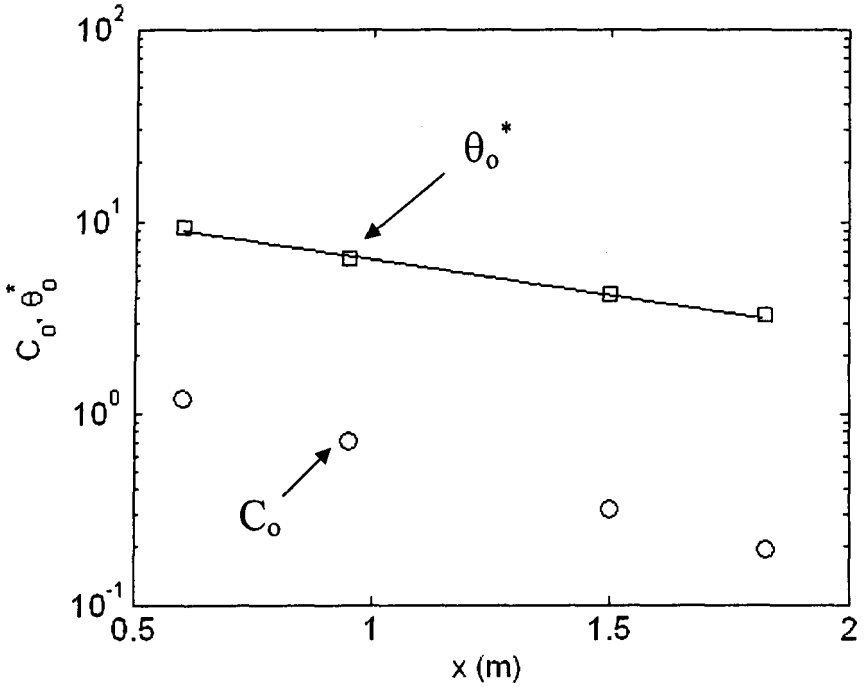

Figure 4.14: Variation of local mean concentration (○) and local concentration scale (□) with downstream distances behind the point source.

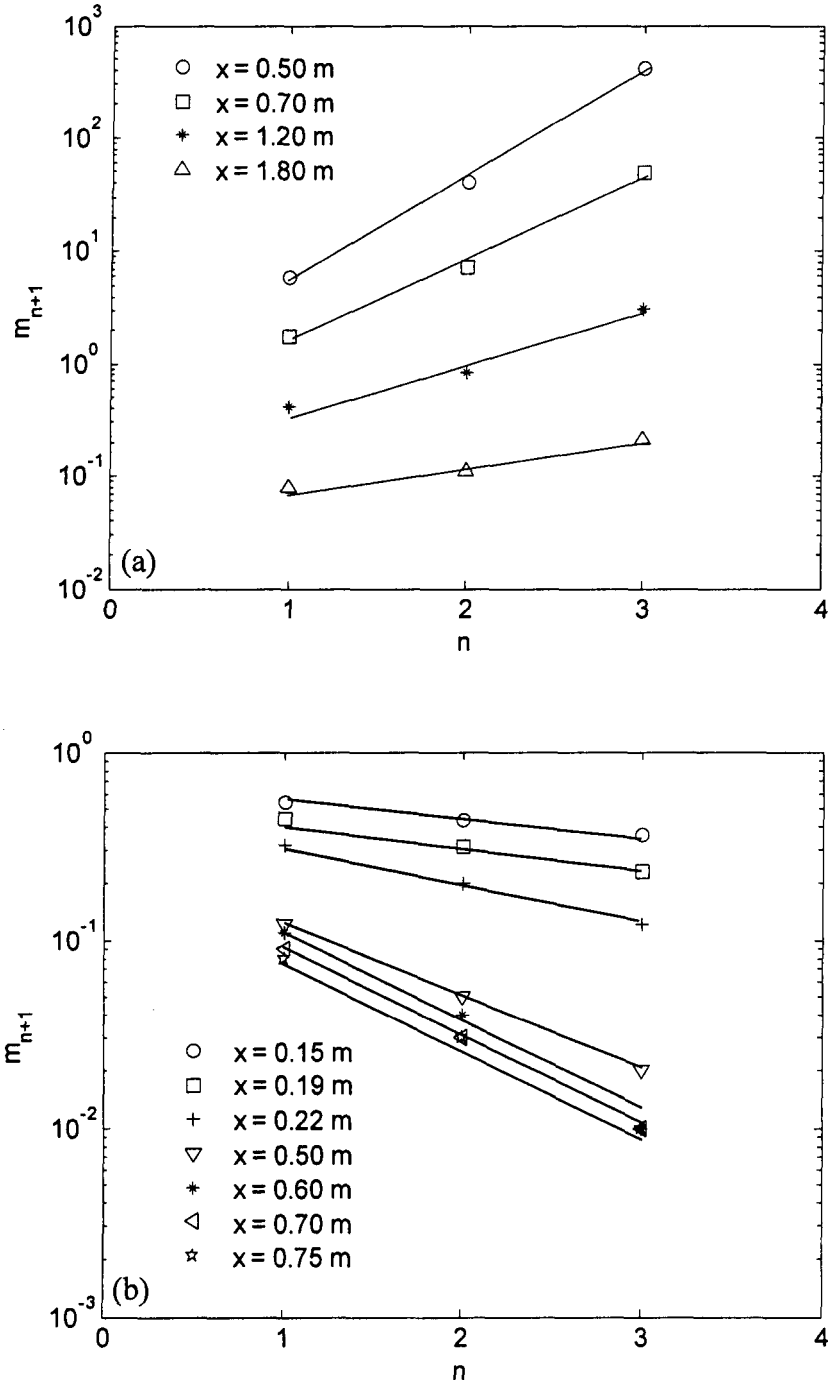

Figure 4.15: Variation of centreline absolute moments with the moment order behind (a) the point source; (b) the line source.

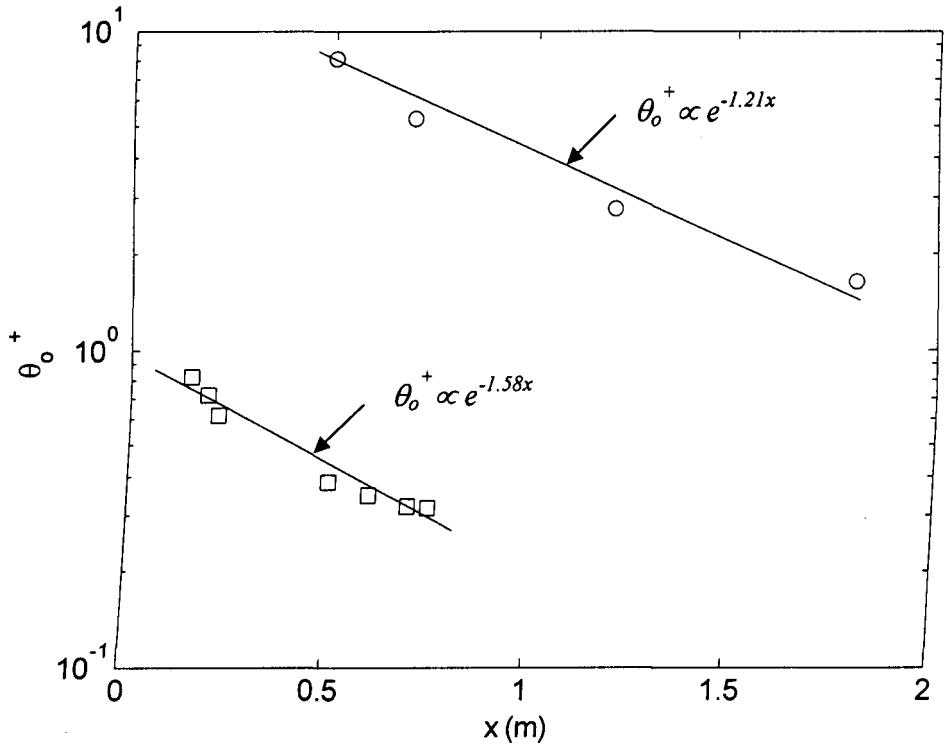

Figure 4.16: Variation of θ_o^+ with downstream distance behind the point source (o) and the line source (□). The solid lines are the exponential fits. In Section 5.2, 'power law' fits are also discussed.

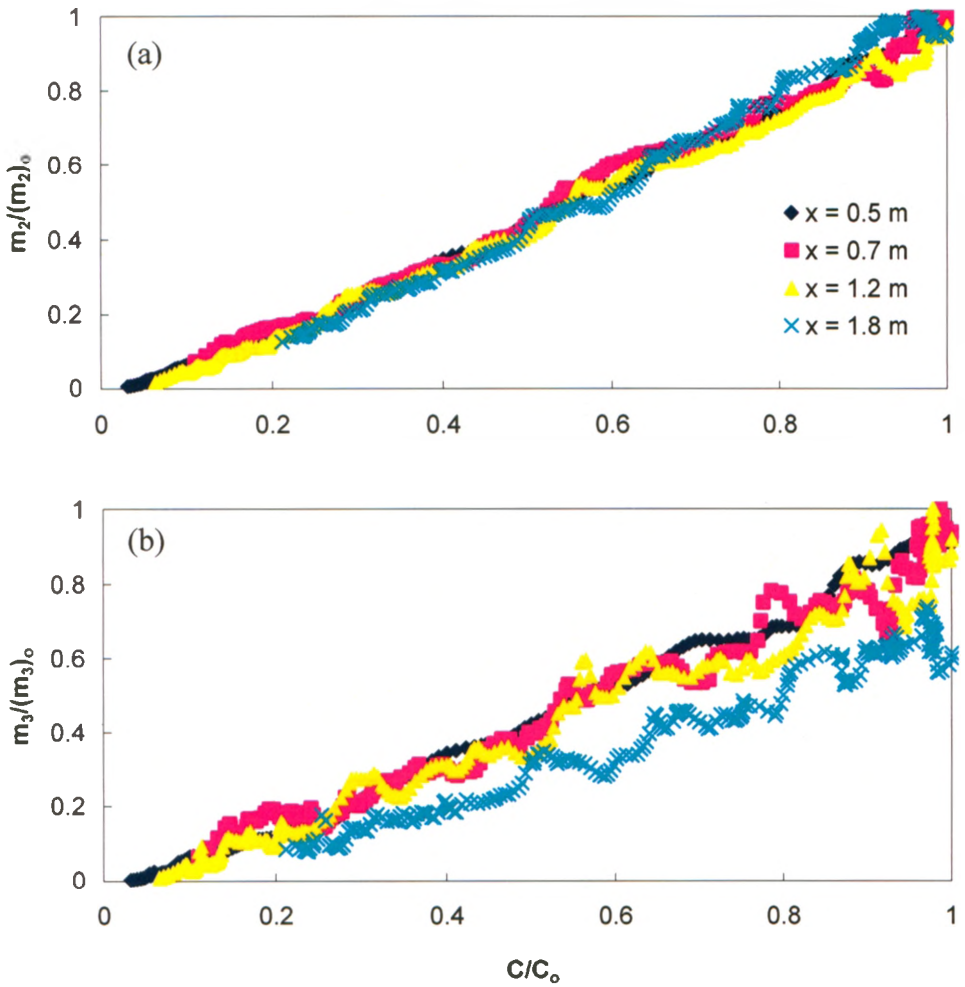

Figure 4.17: The distributed moments as a function of the mean concentration behind the point source. Both the axes are normalized by the centreline values.

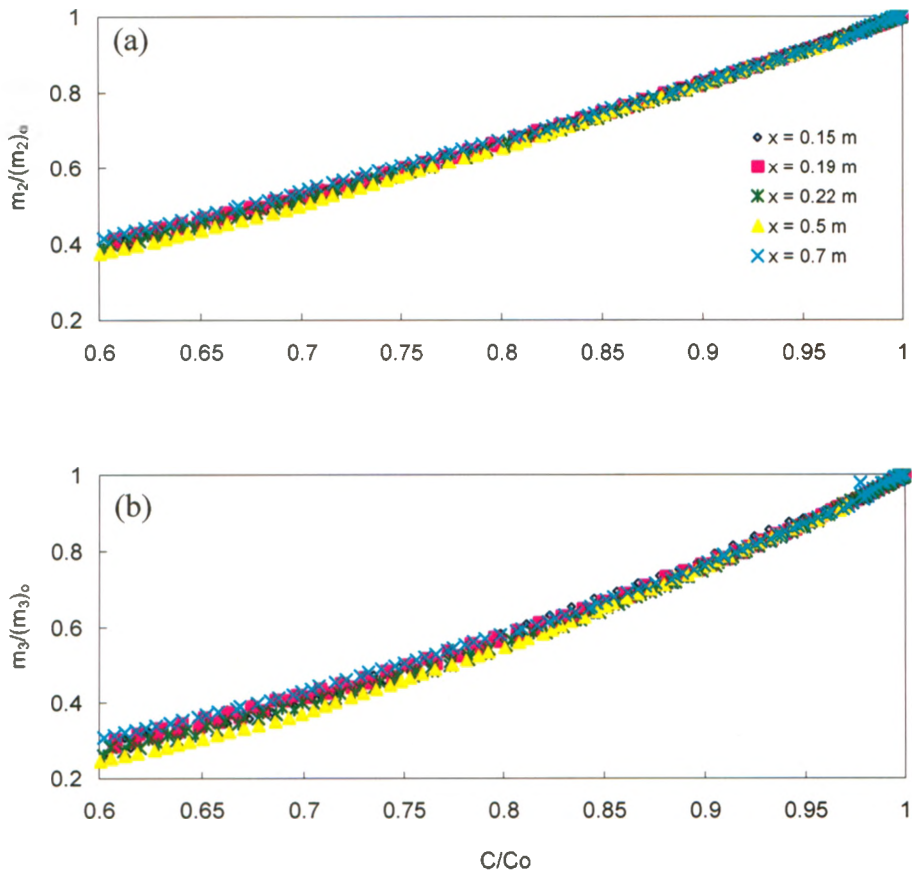

Figure 4.18: The distributed moments as a function of the mean concentration behind the line source. Both the axes are normalized by the centreline values.

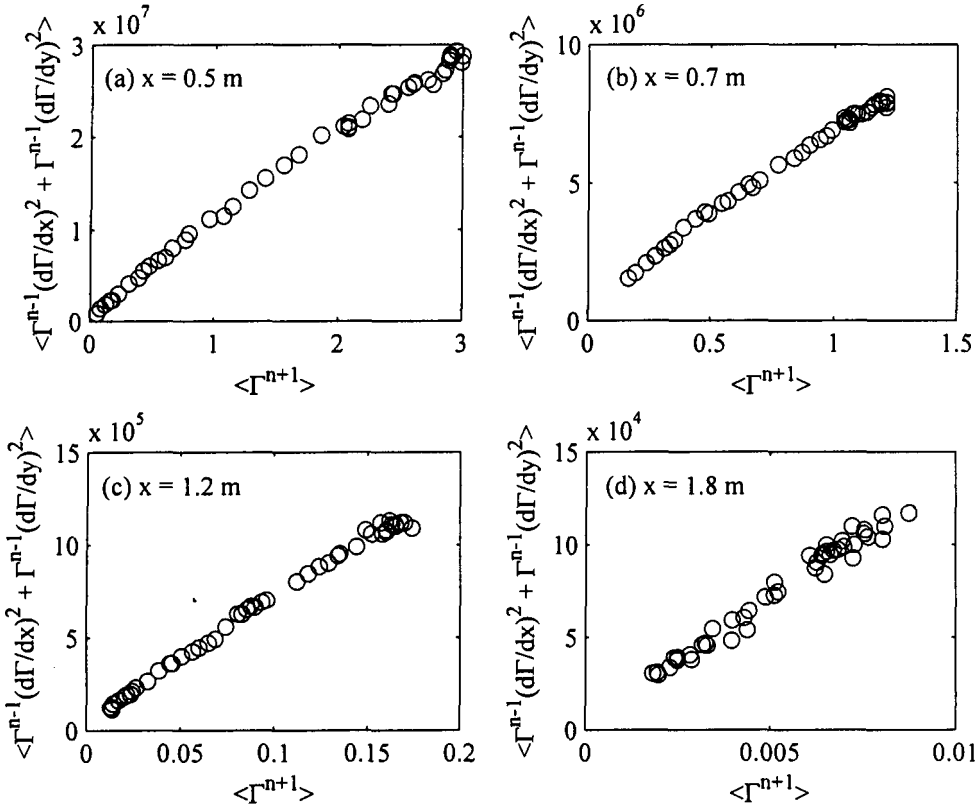

Figure 4.19: Dissipative closure approximation for $n = 1$ at four downstream distances behind the point source. Linear trends in the figure appear to validate the dissipative closure approximation.

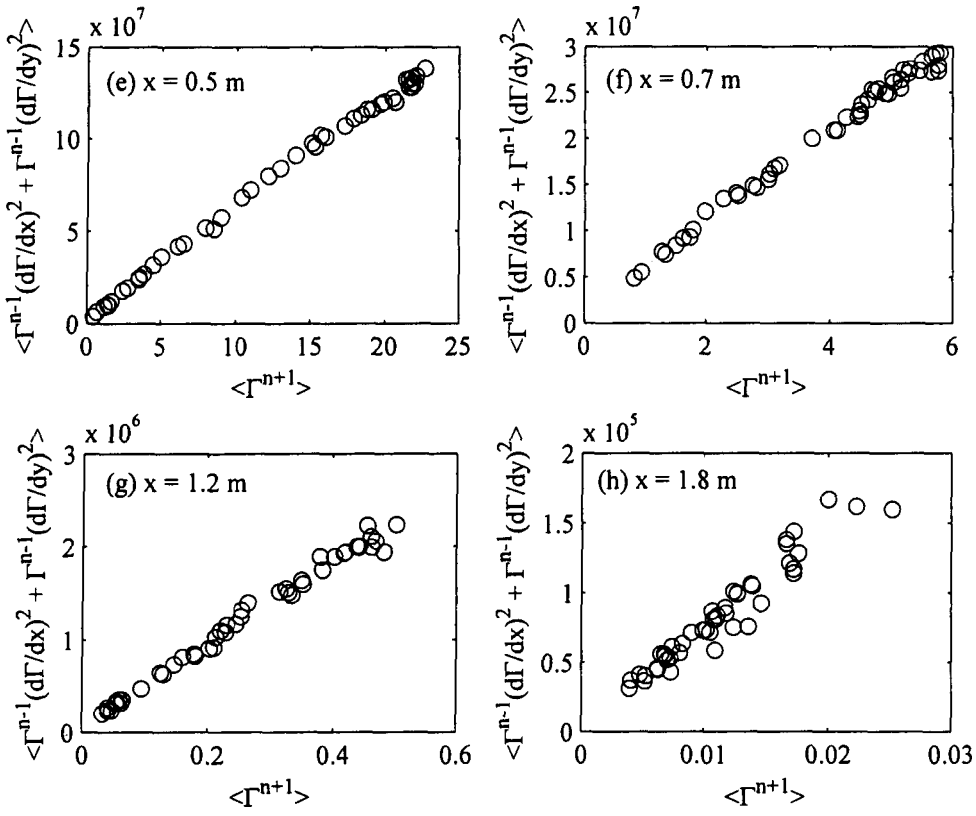

Figure 4.19 (continued): Dissipative closure approximation for $n = 2$ at four downstream distances.

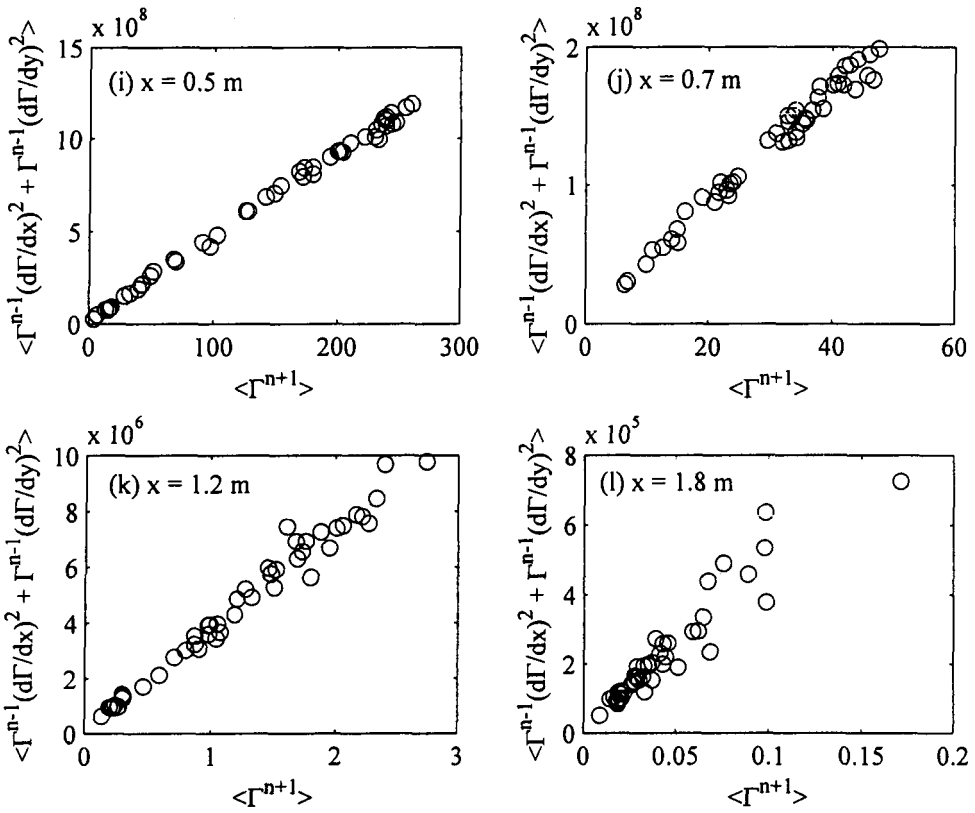

Figure 4.19 (continued): Dissipative closure approximation for $n = 3$ at four downstream distances.

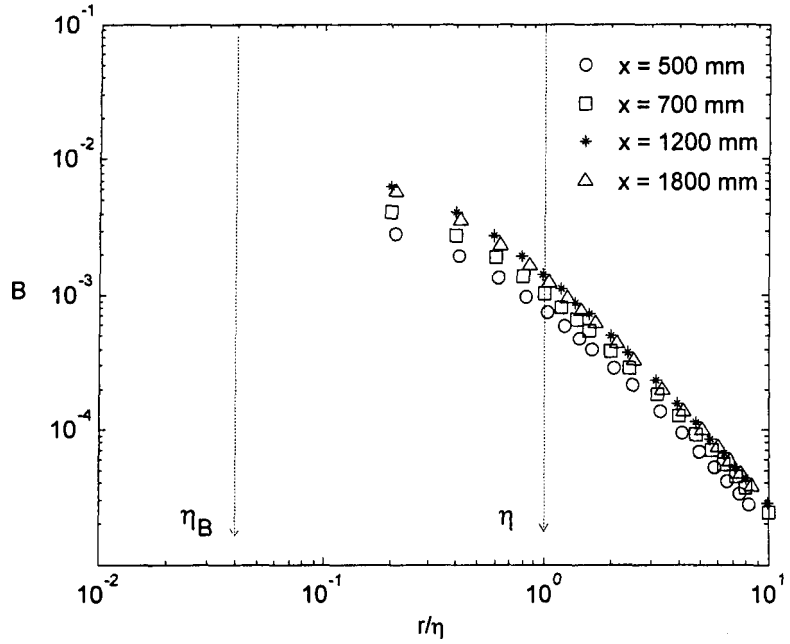

Figure 4.20: Variation of the proportionality constant (B) behind the point source with increasing scale r for n = 1, which show two distinct self-similar zones separated by the Batchelor scale and the Kolmogorov scale.

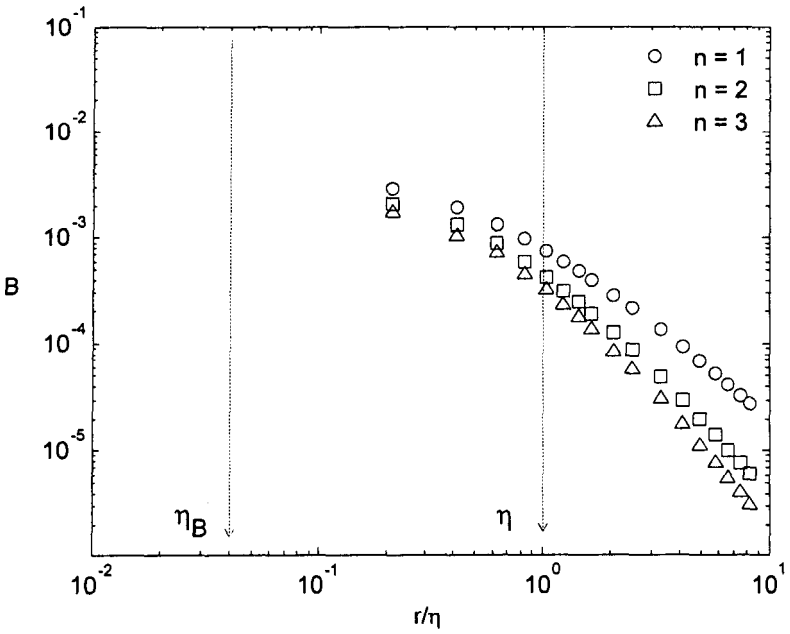

Figure 4.21: Variation of the proportionality constant for different moment order at a downstream distance of 500 mm behind the point source.

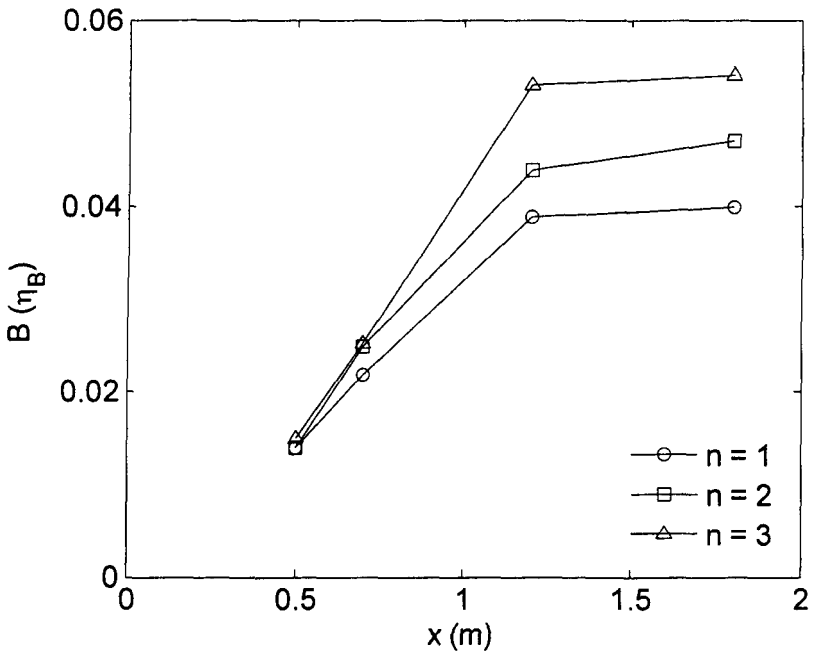

Figure 4.22: Variation of the constant, B, at the Batchelor scale (after extrapolation) with distance downstream behind the point source. This shows a plateau in the far field.

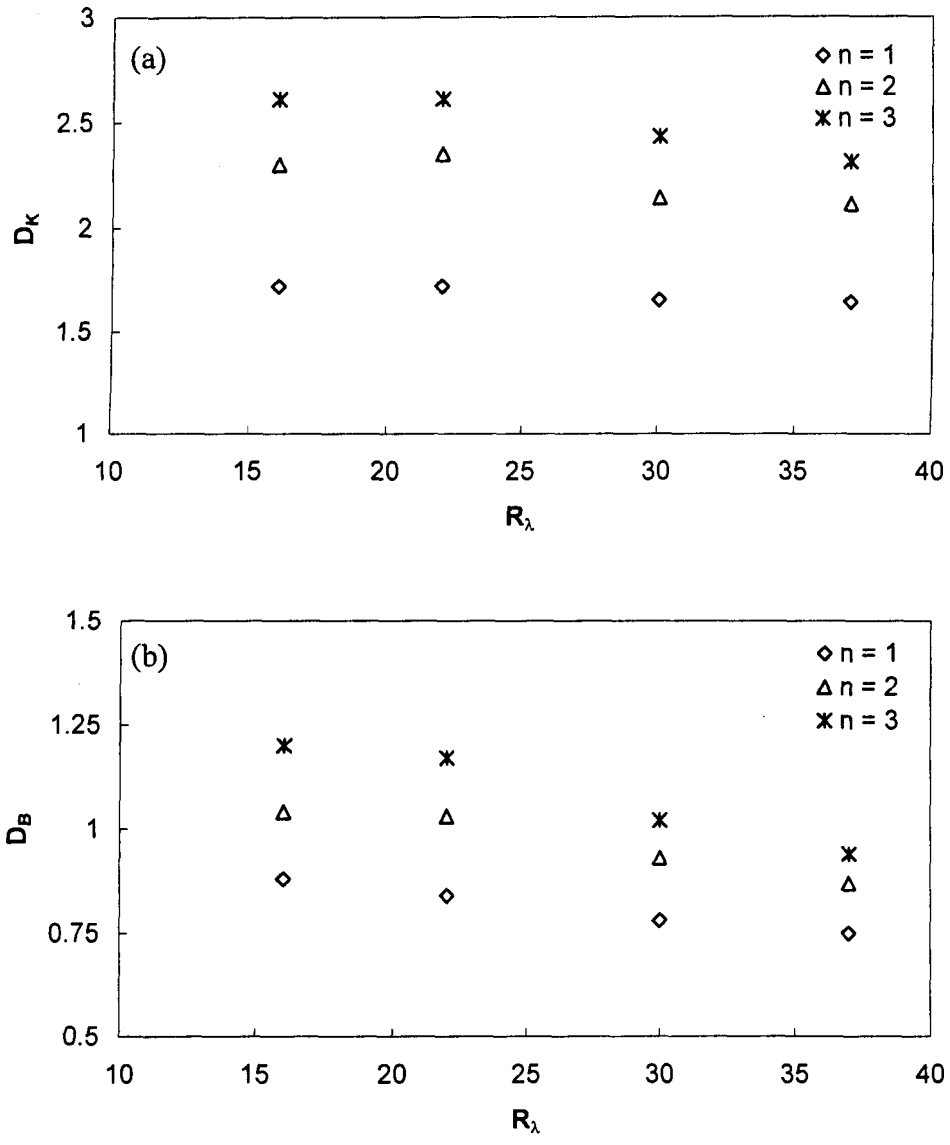

Figure 4.23: Variations of the dimensions of (a) the *K*-zone and (b) the *B*-zone with Taylor micro-scale Reynolds number.

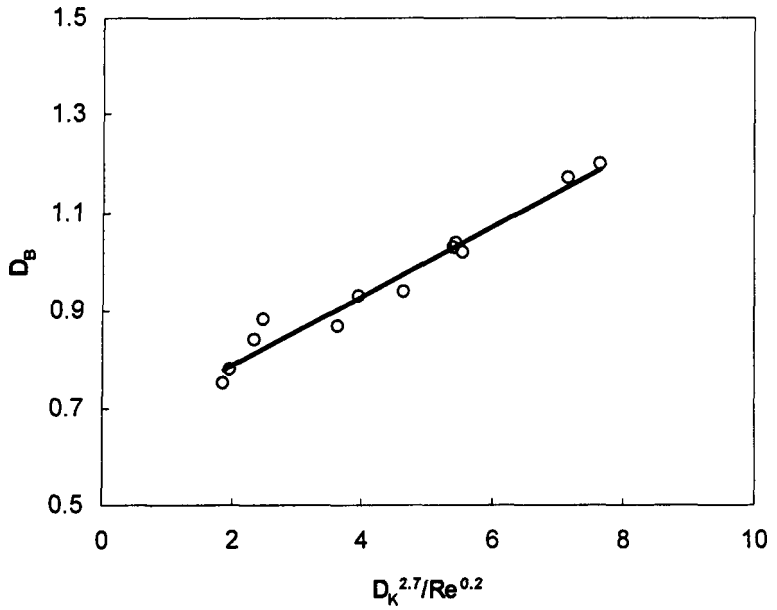

Figure 4.24: Least-square fit of the prediction based on dimension in the *K*-zone and Taylor micro-scale Reynolds number.

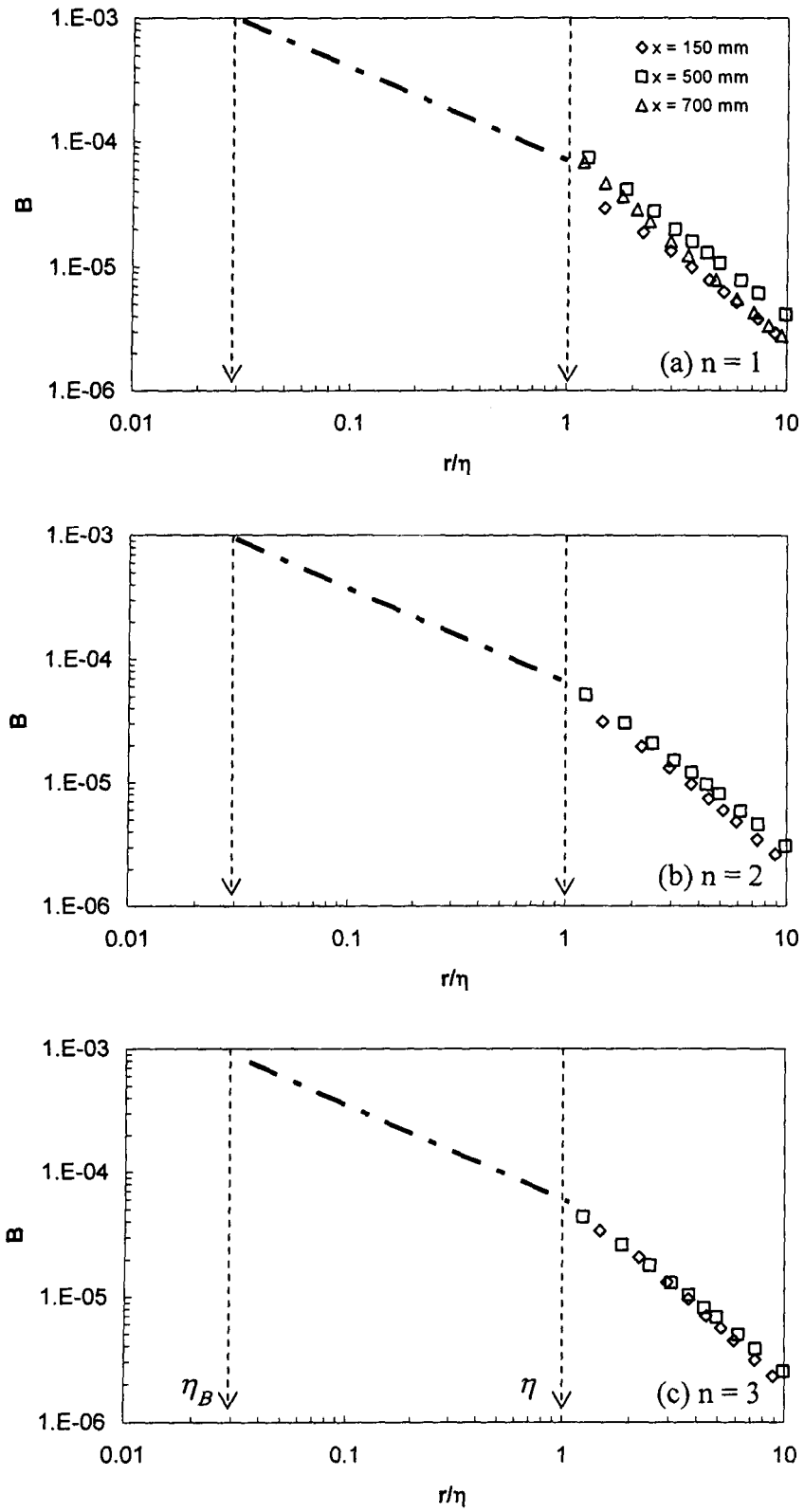

Figure 4.25: Distribution of the predicted B values at the B-zone (broken line) along with the B values in the K-zone measured behind a line source.

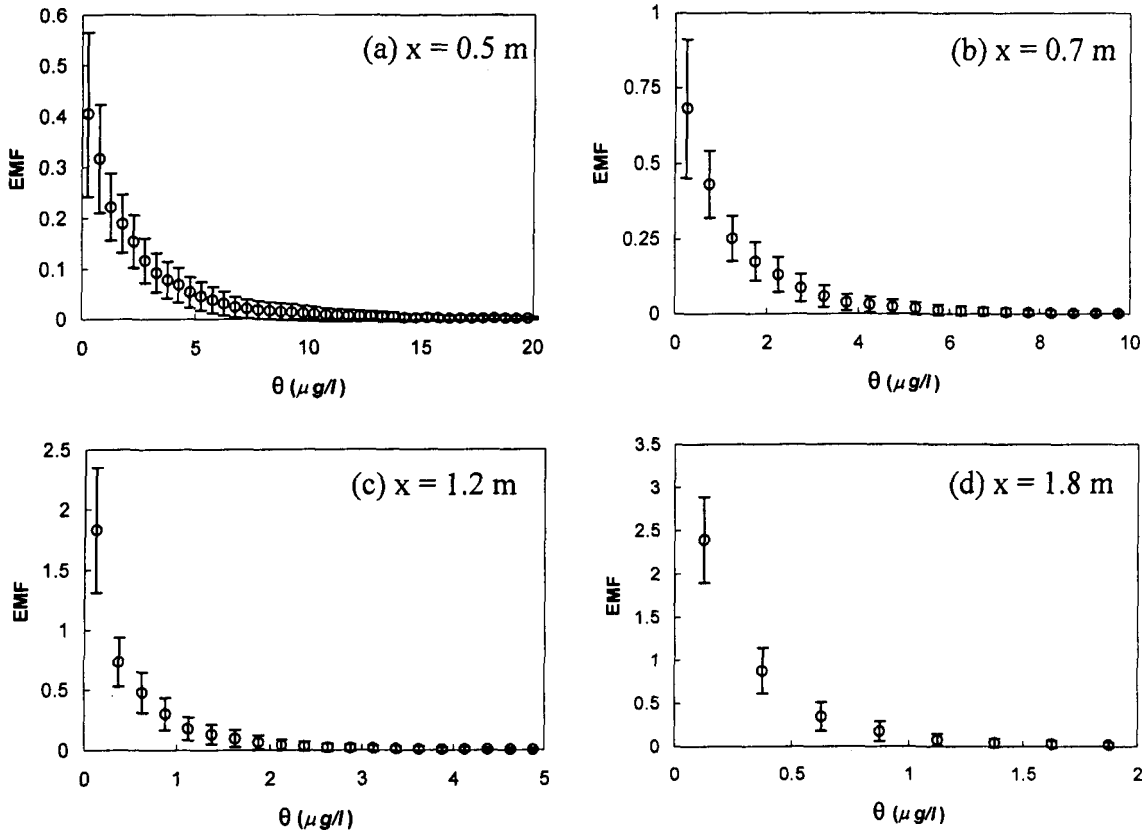

Figure 4.26: EMF behind a point source, vertical bars are the standard deviation.

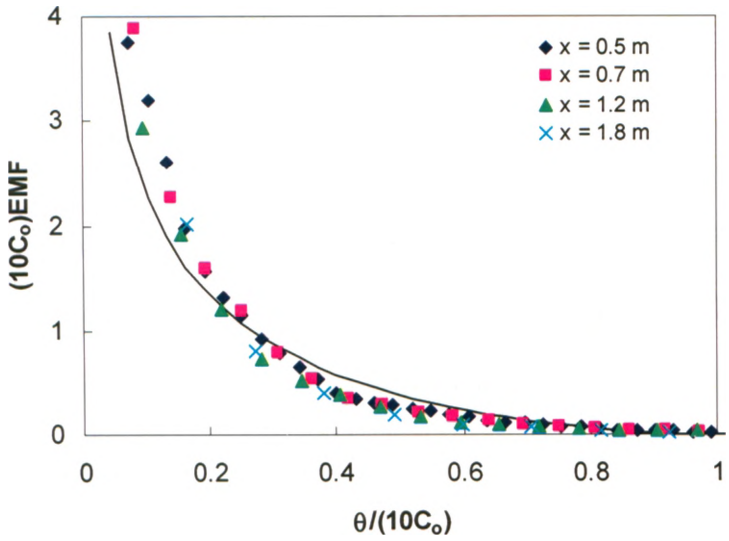

Figure 4.27: Self-similar EMF functions behind a point source (continuous line is the Beta distribution).

Chapter 5: Discussion of the Experimental Results

5.1 Introduction

It would appear from the results shown in Chapter 4 that the EMF is, to a reasonable approximation, represented by a simple, approximately self-similar function when the concentration is scaled with the centreline mean concentration. It would also appear that the distributed moments result from the convection across the plume, by plume-scale convective turbulent motions, are of an equivalent dominant local concentration scale. This construct leads to the apparently successful validation of the convection closure approximation. Further, this construct is consistent, when the equivalent local concentrations are in strands of a conduction cut-off size, with the apparently successful validation of the dissipative closure approximation. In this chapter, an attempt is made to elucidate the underlying physical explanation of the experimental observations in Chapter 4.

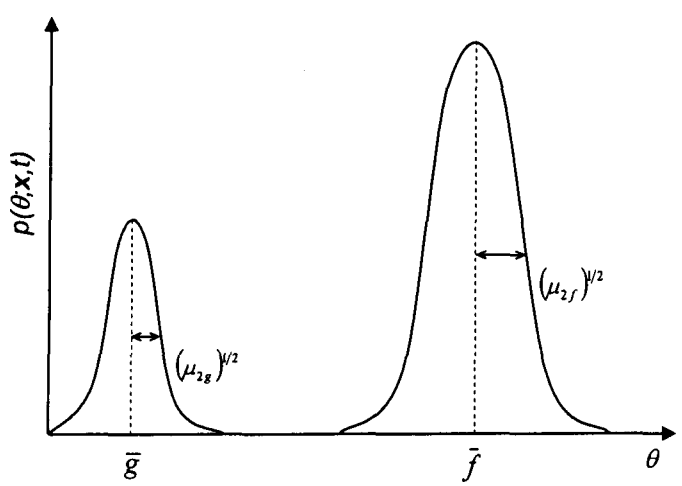

Figure 5.1: A sketch of the PDF in terms of the source and non-source PDFs.

5.2 PDF and Moments

In general the PDF can be expressed (Chatwin and Sullivan, 1989) as

$$p(\theta;\mathbf{x},t)=(1-\pi(\mathbf{x},t))g(\theta;\mathbf{x},t)+\pi(\mathbf{x},t)f(\theta;\mathbf{x},t), \tag{5.1}$$

where $f(\theta;\mathbf{x},t)$ and $g(\theta;x,t)$ are the probability density functions of source and non-source fluid, respectively, and $\pi(x,t)$ is the probability of being in source-fluid when $\kappa = 0$ (see Figure 5.1).

We note that in the evolution of $p(\theta;x,t)$, changes in $f(\theta;\mathbf{x},t)$ and $g(\theta;x,t)$ (that is the transfer from source to non-source fluid) only takes place through molecular diffusivity, κ, and changes in π occur via turbulent convective motion and these changes are strictly independent of κ. The first few moments are:

$$\left.\begin{aligned} C &= (1-\pi)\bar{g}+\pi\bar{f}, \\ m_2 &= (1-\pi)(\bar{g}^2+\mu_{2g})+\pi(\bar{f}^2+\mu_{2f}), \\ m_3 &= (1-\pi)(\bar{g}^3+\mu_{3g}+3\bar{g}\mu_{2g})+\pi(\bar{f}^3+\mu_{3f}+3\bar{f}\mu_{2f}), \end{aligned}\right\} \tag{5.2}$$

where $\bar{g}$, $\bar{f}$, μ_{ng} and μ_{nf} are the mean and central moments of g and f, respectively. Near the source, $(1-\pi)\bar{g} << \pi\bar{f}$ and one can neglect the contributions from g, which results in

$$\left.\begin{aligned} C &= \pi\bar{f}, \\ m_2 &= \left(1+\frac{\mu_{2f}}{\bar{f}^2}\right)\bar{f}C, \\ m_3 &= \left(1+\frac{\mu_{3f}+3\bar{f}\mu_{2f}}{\bar{f}^3}\right)\bar{f}^2C. \end{aligned}\right\} \tag{5.3}$$

One can note by comparison the approximation,

$$m_{n+1} = B_n\left(\theta_o^{+}\right)^n C, \tag{5.4}$$

from the previous chapter, where the exact $\kappa = 0$ result of $m_{n+1} = \theta_o^{\,n} C$ is modified to account for the $\kappa \neq 0$ effects on the representative strand concentration now given by the local concentration scale, θ_o^{+}, and the introduction of the proportionality factor, B_n. Here, θ_o^{+} and B_n are functions of time only for a cloud, or distance downstream for a steady source.

It is interesting to note the expression for moments given in Mole et al. (2008), which derives from (2.36) in Chapter 2,

$$m_2 = \beta(\alpha\beta C_o)C\left[1+\left(\frac{1}{\beta}-1\right)\left(\frac{1}{\beta}+1\right)\frac{C}{\alpha C_o}\right],$$

$$m_3 = \beta(\alpha\beta C_o)^2 C\left[\lambda_3{}^2+3\left(\frac{1}{\beta}-1\right)\frac{C}{\alpha C_o}+\left(\frac{1}{\beta}-1\right)^2\left(\frac{1}{\beta}+2\right)\left(\frac{C}{\alpha C_o}\right)^2\right], \tag{5.5}$$

$$\vdots$$

which become, for a $\beta \sim 1$ near-source approximation,

$$m_{n+1} = \beta(\alpha\beta\lambda_{n+1}C_o)^n C. \tag{5.6}$$

Values of the λ_n are observed to be close to unity in Schopflocher et al. (2007). It was shown in Sullivan and Ye (1996) that if $\lambda_n = 1$ in (2.36) then the corresponding PDF is

$$p(\theta) = (1-\hat{C})\delta(\theta-\theta_1)+\hat{C}\delta(\theta-\theta_2), \tag{5.7}$$

where $\hat{C} = C/\alpha C_o$, $\theta_1 = (1-\beta)C$ and $\theta_2 = \theta_1 + \alpha\beta C_o$. The two-delta function PDF in (5.7) represents the background concentration as an equivalent concentration at θ_1 and the source concentration as an equivalent 'strand' concentration, θ_2. That is, the μ_{ng}, $\mu_{nf} \to 0$

in (5.2). It is interesting to observe in Sullivan and Ye (1996) and Ye (1995) that where there was a prominent bimodal PDF, the two-delta function generally agreed in both location and relative size with the two humps. Also, in Schopflocher and Sullivan (2002) similar agreement of the two-delta solution was found when the PDF was separated into a 'strand' PDF and 'background' PDF.

The near-source ($\beta \sim 1$) moment approximation from (5.7) is

$$m_{n+1} = \beta(\alpha\beta C_o)^n C \,. \tag{5.8}$$

A comparison of (5.4) and (5.6) suggests that

$$B_n = \beta\lambda_{n+1}{}^n \quad \text{and} \quad \theta_o^+ = \alpha\beta C_o \,. \tag{5.9}$$

And from (5.3)

$$\theta_o^+ = \bar{f}\,,$$

$$B_1 = \left(1 + \frac{\mu_{2f}}{\bar{f}^2}\right) \text{ and} \tag{5.10}$$

$$B_2 = \left(1 + \frac{\mu_{3f} + 3\bar{f}\mu_{2f}}{\bar{f}^3}\right).$$

Observations in Mole et al. (2008) that the parameters of the generalized Pareto density function, that describes the high-concentration range, do not appreciably vary over the flow cross-section, suggest that $f(\theta;\mathbf{x},t)$ remains reasonably unchanged across the plume. That is, a basic pattern of strand concentrations are convected by large-scale turbulent motions over the entire cross-section. This notion also has some support from

observations on the strand-background PDF decomposition shown in Schopflocher and Sullivan (2002). The distributed moments shown in Figure 4.17 and Figure 4.18 in Chapter 4 appear to support this contention, where the distributed measured moments are shown as a linear function of mean concentration near the centreline.

The moments of the EMF from (5.4) are

$$M_n = B_n\left(\theta_o^+\right)^n, \tag{5.11}$$

and from (5.3), neglecting the variation of $f(\theta;\mathbf{x},t)$ over the plume cross-section, are

$$\left.\begin{aligned} M_1 &= \left(1+\frac{\mu_{2f}}{\bar{f}^2}\right)\bar{f}, \\ M_2 &= \left(1+\frac{\mu_{3f}+3\bar{f}\mu_{2f}}{\bar{f}^3}\right)\bar{f}^2. \end{aligned}\right\} \tag{5.12}$$

Table 5.1 Summary of the EMF moments behind the line source

x (m)	M_1/C_o	M_2/C_o^2	M_3/C_o^3	θ_o^+/C_o	$\alpha\beta$	β
0.15	0.744	0.698	0.755	1.15	1.39	0.81
0.19	0.740	0.668	0.669	1.11	1.43	0.8
0.22	0.773	0.716	0.737	1.11	1.52	0.8
0.5	0.703	0.612	0.598	1.12	0.46	0.19
0.7	0.784	0.728	0.735	1.10	0.46	0.34
Average	0.749	0.684	0.699	1.13	-	-

If we set $\bar{f} = \gamma C_o$, $\gamma = 1.13$, $M_1 = \left(1+\frac{\mu_{2f}}{\bar{f}^2}\right)\gamma C_o$, then,

$$\left.\begin{aligned} 1+\frac{\mu_{2f}}{\bar{f}^2} &= \frac{0.749}{1.13} = 0.663, \\ 1+\frac{\mu_{3f}+3\bar{f}\mu_{2f}}{\bar{f}^3} &= \frac{0.684}{(1.13)^2} = 0.536. \end{aligned}\right\} \tag{5.13}$$

The important practical point here is the small variation of M_1/C_o and M_2/C_o^2 on the entire experimental range over which the mean concentration has been reduced by more than a factor of 100. A similar observation appears in Schopflocher et al. (2007) where $1.1 < M_1/C_o < 1.5$ and $1.3 < M_2/C_o^2 < 2.9$. These estimates were made using measured α and β values and the difference in spatial resolution in experiments may have contributed to the difference in measured moments.

As one goes downstream when $\pi f << (1-\pi)g$ in (5.2) the roles of f and g are reversed. In this range the moments are

$$\left.\begin{aligned} C &= (1-\pi)\bar{g} \\ m_2 &= \left(1+\frac{\mu_{2g}}{\bar{g}^2}\right)\bar{g}C \\ m_3 &= \left(1+\frac{\mu_{3g}+3\bar{f}\mu_{2g}}{\bar{g}^3}\right)\bar{g}^2 C \end{aligned}\right\} \tag{5.14}$$

As in the discussion above, if one anticipates, one pattern of non-source fluid to be convected across the plume reasonably unchanged and identify the dominant concentration scale from (5.4) to be $\theta_o^+ = \bar{g}$ and with proportionality factors

$$\left.\begin{aligned} B_1 &= \left(1+\frac{\mu_{2g}}{\bar{g}^2}\right), \\ B_2 &= \left(1+\frac{\mu_{3g}+3\bar{g}\mu_{2g}}{\bar{g}^3}\right), \end{aligned}\right\} \tag{5.15}$$

and,

$$\left.\begin{aligned} M_1 &= \left(1+\frac{\mu_{2g}}{\bar{g}^2}\right)\bar{g}, \\ M_2 &= \left(1+\frac{\mu_{3g}+3\bar{g}\mu_{2g}}{\bar{g}^3}\right)\bar{g}^2. \end{aligned}\right\} \tag{5.16}$$

One can note from (5.5) that

$$\left.\begin{aligned} M_1 &= C_o\left(\alpha\beta^2+\frac{1-\beta^2}{\sqrt{2}}\right), \\ M_2 &= C_o{}^2\left(\alpha^2\beta^3\lambda_3{}^2+3\beta^2(1-\beta)\frac{\alpha}{\sqrt{2}}+\frac{(1-\beta)^2(1+2\beta)}{\sqrt{3}}\right), \end{aligned}\right\} \tag{5.17}$$

when, for the Gaussian mean concentration functions in this experiment,

$$\int C^n dA = \frac{C_o{}^{n-1}}{\sqrt{n}}Q \tag{5.18}$$

is used. The comparison in Table 5.1 of M_1/C_o and $M_2/C_o{}^2$ values for the small values of β is quite reasonable considering measurement inaccuracies in values of $0.19 < \beta < 0.35$. In Figure 4.6, the measured value of the EMF moments are compared with the exponential fits

$$\left.\begin{aligned} M_1 &= 0.64\,e^{-1.62x}, \\ M_2 &= 0.50\,e^{-3.29x}, \\ M_3 &= 0.45\,e^{-5.02x}. \end{aligned}\right\} \tag{5.19}$$

That is, the form $M_n = B_n(e^{-dx})^n$ and the B_n are a reasonable approximation to the values in Table 5.1 that is $B_n = (M_n/C_o^n)/(\theta_o^+/C_o)^n$ provides the average values $B_1 = 0.663$, $B_2 = 0.536$ and $B_3 = 0.498$. The n dependence of the exponential is also quite reasonable. It is also interesting to compare the local concentration scale $\theta_o^+ = 0.94e^{-1.58x}$ shown in Figure 4.16 with the $e^{-1.62x}$ given for M_1. That is, from (5.11) $M_1 = B_1\theta_o^+$ such that $B_1 = 0.64$ and $\theta_o^+ = 0.94e^{-1.62x}$.

It is to be noted that at least a good fit of the EMF moments are given by 'power-law' as

$$\left.\begin{aligned} M_1 &= 0.17\,x^{-0.6}\,, \\ M_2 &= 0.056\,x^{-1.2}\,, \\ M_3 &= 0.008\,x^{-1.85}\,. \end{aligned}\right\} \qquad (5.20)$$

For the local concentration scales, $\theta_o^+ = 0.26x^{-0.6}$ for the line source and $\theta_o^+ = 3.42x^{-1.26}$ for the point source were found. The same desirable features for the exponents and coefficients, as were true for the exponential fits, are obtained with the 'power-law' fits.

5.3 The Closure Approximations

It appears in Figures 4.7 – 4.12 and Figure 4.19 that both the convective and dissipative closure approximations are validated for the point source experiments. For the convective approximation a dominant local concentration scale, θ_o^*, which changes relatively slowly as one goes downstream, is rapidly convected across the flow by

turbulent convective motion as shown in Figure 4.13. For the range of experiments considered here, θ_o^* appears to decay exponentially as $\theta_o^* = 15e^{-0.84x}$ with downstream distance in Figure 4.14 for the point source and too slowly to monitor for the accuracy achieved with the line source. The local concentration scale, as given in (5.4), and measured directly from the centreline moments, is also shown in Figure 4.16 to decay exponentially as $\theta_o^+ = 13.35e^{-1.21x}$ for the point source. Since the mean concentration decays as $C_o \sim x^{-p/2}$, where p (= *1, 2, 3*) is the dimension of the Gaussian concentration function, the ratio θ_o^+/C_o will inevitably go through a maximum as one goes downstream (although this may occur too close to the source to be observable in the present experiments), and hence, parallel the evolution of the maximum value of concentration discussed in Mole et al. (2008). This dependence suggests a quantitative, but minor, structural modification to the solution given in Sullivan (2004) wherein θ_o^+ simply replaces θ_o in (2.58).

In principle, the function θ_o^+ is calculated using (5.12) and (2.34) using the dissipative closure approximation. Alternatively, one could calculate the α and β as done in Clarke and Mole (1995), Labropulu and Sullivan (1995) and Moseley (1991). In the dissipative closure approximation (2.56), the background threshold concentration Γ_t is set to zero. This is seen to be an appropriate consideration here for the near-source ($\beta \sim 1$) experiments and consistent with the discussion in § 5.2 where the contribution from the non-source PDF $g(\theta;x,t)$ is neglected. The solution to (2.34) using the closure approximation, with B and η_B independent of x is

$$\left.\begin{aligned} M_n &= M_n(o)e^{\{-n(n+1)y\}}, \\ &= M_n(o)\left\{e^{-(n+1)y}\right\}^n, \\ &= M_n(o)\left\{e^{-2y}\left(1-(n-1)y+\frac{(n-1)^2}{2}y^2+\cdots\right)\right\}^n, \end{aligned}\right\} \tag{5.21}$$

where $y = \left(\kappa B/U\eta_B{}^2\right)x$. For $y << (n\text{-}1)^{-1}$ (in the present experiments the largest value of y is about 0.63)

$$M_n = M_n(o)\left\{e^{-2y}\right\}^n. \tag{5.22}$$

That is, $\theta_o^{+} = e^{-2y}$ when (5.22) is compared with (5.11). In the present experiments, the Batchelor scale varies with downstream distance (Table 3.1) and it would appear in Figure 4.20 that the B does as well (B also appears to depend on n). It may also be relevant to introduce a threshold concentration, Γ_t, as was done in Smith (2004). Equation (5.21) can be modified to account for the downstream variation of $B/\eta_B{}^2$ by expanding in a Taylor series referred to the release position such that (5.22) becomes

$$M_n = B_n\left\{e^{-2y}\right\}^n, \tag{5.23}$$

where $y = (\kappa B/U\eta_B{}^2)_o x$, and

$$B_n = M_n(o)\exp\left[-n(n+1)\frac{\kappa}{U}\left\{\left(B/\eta_B{}^2\right)_o{}'\frac{x^2}{2}+\left(B/\eta_B{}^2\right)_o{}''\frac{x^3}{6}+\cdots\right\}\right], \tag{5.24}$$

where ' represents the first derivative, '' represents the second derivative, and subscripts 'o' represents the source location. One is, however, encouraged by the consistency of the ratio M_n/C_o^n observed in Table 5.1. Using the values of U = 0.2 m/s, κ = 8 x 10^{-10} m^2/s, η_B = 0.016 & 0.025 mm and B = 0.015 & 0.055 the point source experimental range of $y = (\kappa B/U\eta_B{}^2)x$ is calculated and found to be between 0.12 and 0.63. Since we do not have

a very good measurement of B for the line source measurements, we have assumed the same values of B from the point source data in order to calculate y for line source. Therefore, using $U = 0.1$ m/s, $\eta_B = 0.01$ & 0.016 mm as a range and the same B values (0.015 & 0.055) as the point source measurements, y is found to be between 0.18 to 1.2. In order to estimate the exponent constant, ζ, evolved in equation (5.22) (as $e^{-2y} \sim e^{-\zeta x}$, x is the distance in meters downstream from the grid), by using the values of y, which provides an estimate of $0.5 < \zeta < 0.7$ for the point source and $2.4 < \zeta < 3.4$ for the line source measurements. However, the constant, ζ, should be analogous to the measured exponent constants shown in Figure 4.16, where $\zeta = 1.21$ for the point source and $\zeta = 1.58$ for the line source.

In the α-β description of (2.36), the $\alpha(x)$ is initially unity, reaches to a value, greater than 2, and ultimately returns asymptotically to a value slightly greater than unity. The $\beta(x)$ is initially unity and monotonically falls to zero. Values of λ_n are typically greater than, however, close to unity. The EMF moments, for the Gaussian mean concentration profile of the line source (5.17) can be written as

$$\left.\begin{aligned} \frac{M_1}{C_o} &= \frac{1}{\sqrt{2}} + \beta^2\left(\alpha - \frac{1}{\sqrt{2}}\right), \\ \frac{M_2}{C_o^{\,2}} &= \frac{1}{\sqrt{3}} + \alpha^2\beta^3\lambda_3^{\,2} + \frac{3}{\sqrt{2}}\alpha\beta^2(1-\beta) + \frac{\beta^2}{\sqrt{3}}(2\beta - 3), \end{aligned}\right\} \qquad (5.25)$$

and as $\beta \to 0$, $M_1/C_o \sim 1/\sqrt{2}$ and $M_2/C_o^{\,2} \sim 1/\sqrt{3}$. These asymptotic moments are reasonably close to the values shown in Table 5.1. The Beta functions, using the asymptotic normalized moments, are shown in Figure 4.5 for comparison.

It is interesting to note, in comparison with (5.20), the special form

$$M_n(\tau) = M_n(o)e^{-n\tau}; \qquad \tau = \frac{t\kappa}{\overline{\eta}_B^{\,2}}, \tag{5.26}$$

where t is the time and $\overline{\eta}_B$ is a representative average strand length scale comparable with η_B, found in Sullivan and Ye (1997) The result in (5.26) is for a model of the concentration field texture that consisted of widely separated strands with the Gaussian concentration distribution across them. In (5.26) the simple replacement of $x = Ut$ and $\overline{\eta}_B = \eta_B/\xi$, where ξ is a constant, facilitates the comparison of (5.26) and (5.23).

The α-β moment prescription (2.36) has received experimental validation over a variety of flow and source configurations of continuous scalar contaminant released in steady flows. In Chatwin and Sullivan (1990), analysis was provided for a wide range of flows including jets, wakes, and plumes in homogeneous turbulence and both smooth-walled and rough-walled boundary-layers. Additional confirmation was given in Moseley (1991) and Ye (1995) with reference to data from line and point source plumes, homogeneous shear flows, buoyant jets as well as data from a cross-flow when a buoyant jet is inserted into a smooth-walled boundary-layer. For the most part, the distributed second moments have been used for validation. Other notable data sources used to test the applicability of the α-β prescription include Stapountzis et al. (1986), Karnik and Tavoularis (1989) and Papantonio and List (1989). The direct validation in the atmospheric boundary-layer (or even for a cloud in the laboratory) would require measured, distributed moments, which are not available.

The expressions for the normalized moments have the advantage that they can be verified using an isolated fixed-point measurement. That prescription, normally using kurtosis and skewness, has been validated in the atmospheric boundary-layer over different stability classes (Mole and Clarke 1995; Lewis et al. 1997) and for clouds of different densities in the laboratory including the presence of fences in the flow; some with crenellation, some without (Chatwin and Robinson, 1997). A remarkable feature of the measurements is the very narrow range of observed values of the coefficients. Chatwin and Robinson (1997) presented a table of the results for the aforementioned cloud experiments where $1 < a_4 < 3$ and $1 < b_4 < 3$. This range essentially covers the field experiments in the atmospheric boundary-layer as well and the present experimental values are shown in Chapter 3.

In Schopflocher and Sullivan (2005), it was established that the result given in (2.37) for the normalized moments derives from the α-β moment prescription given in (2.36); that is the observation of (2.37) validates (2.36). This connection is also discussed in Mole et al. (2008). In that paper, the well-controlled measurements of a plume diffusing in grid turbulence were examined and the slight variations of the coefficients were observed to be consistent with the α-β prescription.

We notice that if (4.4) were to apply everywhere, using (2.33) and $\theta_o^+ = \gamma C_o$ will yield

$$\frac{m_{n+1}}{C_o^{n+1}} = B_n \gamma^n = \frac{M_n}{C_o^n}. \tag{5.27}$$

That is, the moments of the EMF (as shown in Table 5.1) are directly given by the centre-line moments shown in Table 4.1. With the introduction of a factor, Ω^n, to take into account the fact that a representative 'local concentration scale' would be less than the centreline when integration over the flow cross-section is carried out, (5.27) is modified to be

$$\frac{M_n}{C_o^{\,n}} = \Omega^n \frac{m_{n+1}}{C_o^{\,n+1}}. \tag{5.28}$$

The values of m_2/C_o^2 and m_3/C_o^3 in Table 4.1 are essentially constant and provide the factor, upon comparison with the values M_1/C_o and M_2/C_o^2 shown in Table 5.1, of Ω = 0.749/1.05 = 0.713 and Ω^2 = 0.664/1.22 = 0.54; where average values of m_2/C_o^2 and m_3/C_o^3 from Table 4.1 and M_1/C_o and M_2/C_o^2 from Table 5.1 are used. Thus one can expect a reasonable approximation for the EMF using the centre-line moments and one empirical factor, Ω. The factor, Ω, will no doubt vary to some extent with different flow and source configurations. The extent of the Ω variation needs to be the subject of future experimentation.

5.4 Summary

The objective of this study is to provide a relatively simple and robust procedure for assessing the evolution of a contaminant concentration field. Consistent with that approach the use of two empirical constants to determine the non-dimensional moments and hence the Beta function or other simple function representation of the EMF is appropriate. The values of M_1/C_o and M_2/C_o^2 shown in Table 5.1 over the distance in the present study show remarkably little change in value.

Chapter 6: Conclusions and Recommendations

6.1 Conclusions

This experimental investigation was undertaken in a relatively simple turbulent flow in order to directly measure the Expected Mass Fraction (EMF) for the first time, as well as to validate the two closure approximations that govern in the evolution of the moments of the probability density function of a scalar concentration. One real advantage of this choice is that the results can be compared with theoretical and experimental results established for a line source of a passive scalar in grid turbulence. In particular, Sawford and Sullivan (1995) established that the α-β description of the lowest four distributed central moments was valid for 16 measuring stations along a 2.6 m wind tunnel flow. Further, using those α-β parameters Schopflocher et al. (2007) showed that the EMF was well described by a simple Beta function. In the present study, it has been verified experimentally that indeed a simple function is not only appropriate, but the function is self-similar when concentrations are normalized with the centreline concentration. That is, the α-β moments appear to generate a reasonable EMF function. In fact, the asymptotic results appear to provide a reasonable approximation even for the near-source measurements investigated in the present study. Thus, the result of the self-similar EMF and favorable comparison with that of Schopflocher et al. (2007) that was derived from the α-β description of the moments, is fully expected to apply to the atmospheric boundary-layer. It has also been shown that a reasonable approximation for the EMF moments is possible by using the centreline moments and an empirical factor, Ω, which could be dependent on different flow and source configurations.

Measurements of scalar concentration are difficult due to the requirement of a spatial resolution smaller than the conduction cut-off length which is 10^{-3} to 10^{-5} m in the most flows. The surfaces of the scalar concentration, where diffusion happens, possess fractal scaling (i.e., self-similar). The concept of fractal scaling inspired us to deal with the under-resolved dissipation calculation in the context of this study. Two distinct self-similar zones were found and are known as the *B*-zone and the *K*-zone. The dimensions (i.e., slopes of the self-similar zones) were calculated for each zone from the point source measurements and it was found that the dimension in the *K*-zone has a tendency to follow the -5/3 slope. That is, it appeared to be similar to the scaling of the passive scalar spectrum in the inertial-convective regime (i.e., the Kolmogorov -5/3 slope) for the first order of moment.

The effect of molecular diffusivity is brought into the convective closure approximation by introducing a representative 'local concentration scale' instead of the source concentration, θ_o, which can be measured directly from the centreline moments. It has been observed in attempting to use the dissipative closure approximation that the results are sensitive to the physical parameters and, in particular, the dependence of B on the distance and order of moments. So, although in principal the moments of the EMF (2.34) could be solved for the lowest two moments $M_1(x)$ and $M_2(x)$, the uncertainties in the estimates of B and η_B would confound the result. Hence, it would appear preferable to empirically determine the exponent constant, ζ, for the first two moments of the EMF.

6.2 Recommendations

An attempt should be taken to measure the cross-sectional plane of a plume coming out of a point source by introducing a mirror at far downstream of the source at an angle of 45 degree to the flow. This will provide the entire cross-section of the plume and the EMF calculations based on the entire cross-section. It would also be good to investigate a line source within a laboratory turbulent boundary layer flow. Although a direct confirmation with field data will be difficult, one would be encouraged by the relative-diffusion analysis of Munro et al. (2003) on the Lidar field measurements of Mikkelson et al. (1995) and in particular of the prospect of the utilization of a scanning beam as provided in Bennett et al. (1992). The spatial resolution (of about 0.5 m) of the Lidar measurements is a drawback; however, it may be possible to use an extrapolative scheme as described in Chapter 2 to mitigate this impediment.

Atmospheric dispersion models are the tools to predict the concentrations of a pollutant downstream of the source. Such models are employed to determine whether an industrial facility will be in compliance with, for example, the National Ambient Air Quality Standard (NAAQS) in United States and other countries (Stathopoulos et al. 2008). The dispersion models, which have been approved by Environmental Protection Agency (EPA), mostly use the Gaussian equations, are appropriate for the far distances. The ASHRAE model is reliable for predicting dispersion at near fields (Stathopoulos et al. 2008). These models are capable of predicting the average concentration at a location downstream of the source using the meteorological data, which gives a vague sense of the contaminant distribution since the average concentration does not really say anything

about the molecular level concentration reduction (molecular diffusion). The average concentration could be misleading for toxic and flammable chemicals or odor in the atmosphere because of the large concentration peaks that are many standard deviations beyond average concentrations. These large concentration peaks are usually ignored in the dispersion models of any hazardous chemical. The present study should be considered as a step forward for the commercial dispersion models in predicting the distribution of the contaminant cloud in mass fraction by using the average concentration at a location downstream of the source that can be calculated using the dispersion models. Therefore, an initiative needs to be taken to make this study (for example, using the far-field asymptotic result following (5.25) as an approximation) as an add-on to the dispersion models.

REFERENCES

Abernethy, R. B. and Benedict, R. P. (1985). "Measurement uncertainty: a standard methodology." ISA Transactions, 24(1), 75-79.

AbuOmar, M.M., 2002. "Experimental study of the flow around surface-mounted pyramids". PhD Thesis, The University of Western Ontario, Ontario, Canada.

Arcoumanis, C., McGuirk, J.J., and Palma, J.M.L.M. (1990). "On the use of fluorescent dyes for concentration measurements in water flows." *Experiments in Fluids*, 10(2-3), 177-180.

Banning, R., (1997). "Spectral analysis methods for Poisson sampled measurements". *IEEE Transactions on Instrumentation and Measurement*, 46(4), 882-887.

Bara, B. M., Wilson, D. J., and Zelt, B.W. (1992). "Concentration fluctuation profiles from a water channel simulation of a ground-level release." *Atmospheric Environment.* A 26, 1053-1062.

Barrett, T. K. (1989). "Nonintrusive optical measurements of turbulence and mixing in a stably-stratified fluid". PhD thesis, University of California, San Diego.

Batchelor, G.K. (1949). "Diffusion in a field of homogeneous turbulence – Eulerian analysis". *Australian Journal of Scientific Research*, 2, 437.

Batchelor, G.K. (1952). *Proc. Camb. Phil. Soc.* 48, 345-362.

Batchelor, G.K., (1953). The theory of homogeneous turbulence. Cambridge University Press.

Batchelor, G. K. (1959) "Small scale variation of convected quantities like temperature in turbulent fluid. Part 1. General discussion and the case of small conductivity", *J of Fluid Mechanics*, 5, 113-133.

Batchelor, G.K. (1964). "Diffusion from sources in a turbulent boundary layer". *Archiwum Mechaniki Stosowanej* 3, 16, 661-670.

Bearman, P.W. and Morel, T., (1983). "Effect of free stream turbulence on the flow around bluff bodies". *Progress in Aerospace Sciences.* 20(2-3), 97-123.

Bell, J.H. and Mehta, R.D., (1989). "Boundary-layer predictions for small low-speed contractions". *AIAA Journal.* 27(3), 372-374.

Benedict, L.H., Nobach, H., and Tropea, C., (2000). "Estimation of turbulent velocity spectra form laser Doppler data". *Measurement Science Technology*. 11, 1089-1104.

Bennett, M., Sutton, S., and Gardiner, D. R. C. (1992). "An analysis of Lidar measurements of buoyant plume rise and dispersion at five power stations". *Atmos. Environ.* 26, 3249–3263.

Catrakis, Haris J. (2000). "Distribution of scales in turbulence." *Physical Review E.* 62(1), 564-578.

Chatwin, P. C. (1968). "The dispersion of a puff of passive contaminant in the constant stress region." *The Quarterly Journal of the Royal Meteorological Society*, 94(401), 350-360.

Chatwin, P.C. (1990). "Hazards due to dispersing gases." *Environmetrics*. 1, 143-162.

Chatwin, P. and Robinson, C. (1997). "The moments of the PDF of concentration for gas clouds in the presence of fences". *Il Nuovo Cimento.* 20(3), 361–383.

Chatwin, P. C. and Sullivan, P. J. (1989). "The Intermittency Factor of Scalars in Turbulence". *Physics of Fluids*. A 1, 761–763.

Chatwin, P.C. and Sullivan, P.J. (1990). "A simple and unifying physical interpretation of scalar fluctuation measurements from many turbulent shear flow". *Journal of Fluid Mechanics*, 212, 533-556.

Chatwin, P.C. and Sullivan, P.J. (1993). "The structure and magnitude of concentration fluctuations". *Boundary-Layer Meteorology*, 62, 269-280.

Clarke, L. and Mole, N. (1995). "Modelling the evolution of moments of contaminant concentration in turbulent flows". *Environmetrics*. 6(6), 607–617.

Coleman, H.W. and Steele, W. (2009). "Experimentation, validation, and uncertainty analysis for engineers". John Wiley & Sons, Inc, 2nd Edition, New York.

Corriveau, A.F. and Baines, W.D. (1993). "Diffusive mixing in turbulent jets as revealed by pH indicator". *Experiments in Fluids*, 16, 129-136.

Corrsin, S. (1951) "On the spectrum of iso-tropic temperature fluctuations in an iso-tropic turbulence", *J. of Applied Physics*, 22, 469-473.

Crimaldi, J. P., Wiley, M. B., Koseff, J. R. (2002). "The relationship between mean and instantaneous structure in turbulent passive scalar plumes." *Journal of Turbulence*. 3(014),1–24.

Csanady G.T. (1973). "Turbulent diffusion in the environment". D. Reidel Publishing Company, Dordrecht, Holland.

Dahm, W.J., Southland, K.B. and Buch, K.A. (1991). "Direct, high resolution, four dimensional measurements of the fine scale structure of Sc >> 1 molecular mixing in turbulent flows". *Physics of Fluids*, A3, 5, 1115-1127.

Dasi, L. P. (2004) "The small-scale structure of passive scalar mixing in turbulent boundary layers", PhD Thesis, Georgia Institute of Technology, Atlanta GA, USA.

Dasi, L. P., Schuerg, F., and Webster, D. R. (2007) "The geometric properties of high-Schmidt-number passive scalar iso-surfaces in turbulent boundary layers", *J. of Fluid Mechanics*, 588, 253-277.

Daviero, G.J., Roberts, P.J.W., and Maile, K. (2001). "Refractive index matching in large-scale stratified experiments." *Experiments in Fluids*. 31(2),119–126.

Davies, J. K. W. (1989). "The application of box models in the analysis of toxic hazards by using the probit dose-response relationship." *Journal of Hazardous Materials*. 22, 19–329.

Derksen, R.W. and Sullivan, P.J. (1990). "Moment approximation for probability density functions". *Combustion and Flame*, 81, 378-391.

Dewey, R. and Sullivan, P. J. (1977). "The asymptotic stage of longitudinal turbulent dispersion within a tube." *Journal of Fluid Mechanics*. 80(2), 293-303.

Fackrell, J. E. and Robins, A. G. (1982). "Concentration fluctuations and fluxes in plumes from point sources in a turbulent boundary layer." *J. Fluid Mech.* 117, 1–26.

Ferrier, A.J., Funk, D.R., and Roberts, P.J.W. (1993). "Application of optical techniques to the study of plumes in stratified fluids". *Dynamics of Atmospheres and oceans*, 20, 155-183.

Frederiksen, R. D., Dahm, W. J. A., and Dowling, D. R. (1996) "Experimental assessment of fractal scale-similarity in turbulent flows. Part 1. One-dimensional intersections", *J. of Fluid Mechanics*, 327, 35–72.

Frederiksen, R. D., Dahm, W. J. A., and Dowling, D. R. (1997) "Experimental assessment of fractal scale-similarity in turbulent flows. Part 2. Higher-dimensional intersections and non-fractal inclusions." *J. of Fluid Mechanics*, 338, 89-126.

Griffiths, R. F. (1991). "The use of probit expressions in the assessment of acute population impact of toxic releases." *Journal of Loss Prevention in the Process Industries*. 4, 49–57.

Gurka, R. (2003). "Coherent structures in turbulent flows". P.hD. thesis, The Technion-Israel Institute of Technology, Israel.

Hall, D.J., Waters, R.A., Marsland, G.W., Upton, S.L. and Emmott, M.A. (1991). "Repeat variability in instantaneously released heavy gas clouds – some wind tunnel model experiments". *Report LR 804, Warren Spring Laboratory, (PA)* Department of Trade and Industry, U.K.

Heagy, W.K. and Sullivan, P.J. (1996). "The expected mass fraction". *Atmospheric Environment*, 30, 35-47.

Hinze, J.D. (1959). "Turbulence". McGraw-Hill Book Co., New York.

Holmes, J.D., (2004). "Trajectories of spheres in strong winds with application to wind-borne debris". *Journal of Wind engineering and Industrial Aerodynamics*. 92(1), 9-22.

Host-Madsen, A. and Caspersen, C., (1995). "Spectral estimation for random sampling using interpolation". Signal Process. 46, 297-313.

Hurst, D. and Vassilicos, J.C. (2007). "Scalings and decay of fractal-generated turbulence". *Physics of Fluids*, 19, 035103.

Karnik, V. and Tavoularis, S. (1989). "Measurements of heat diffusion from a continuous line source in a uniformly sheared turbulent flow". *J Fluid Mech.* 20, 233–261.

Kopp, G.A. and Keffer, J.F., (1996). "Coherent structures in two uniformly distorted plane turbulent wakes." *Physics of Fluids*, 8(10), 2706.

Labropulu, F. and Sullivan, P. J. (1995). "Mean-square values of concentration in a contaminant cloud". *Environmetrics*. 6(6), 619–625.

Larose, D. T. (2006). "Data mining methods and models". John Wiley and Sons. 2nd edition.

Lavertu, T. M., Mydlarski, L., and Gaskin, S. J. (2008). "Differential diffusion of high-Schmidt-number passive scalars in a turbulent jet". *J. Fluid Mech.* 612, 439–475.

Lewis, D.M. and Chatwin, P.C. (1995). "The treatment of atmospheric dispersion data in the presence of noise and baseline drift". *Boundary-Layer Met.* 72, 53–85.

Lewis, D. M., Chatwin, P. C., and Mole, N. (1997). "Investigation of the collapse of the skewness and kurtosis exhibited in atmospheric dispersion data". *Il Nuovo Cimento.* 20(3), 385–397.

Lumley, J.L. and McMahon, J.F. (1967). "Reducing water tunnel turbulence by means of honeycomb." *Journal of Basic Engineering*. 89, 764-770.

Mandelbrot, B. B. (1983) "The Fractal Geometry of Nature". Freeman, New York.

Mehta, R.D., (1984). "Turbulent flow through screens". *AIAA Journal*, 84- 0538.

Mehta, R.D., (1985). "A turbulent boundary layer perturbed by a screen". *AIAA Journal*, 23, 1335-1342.

Mehta, R.D. and Bradshaw, P., (1979). "Design rules for small low speed wind tunnels". *Aeronautical Journal*. 83 (827), 443-449.

Melling, A, (1997). "Tracer particles and seeding for particle image velocimetry". Measurement Science and Technology. 8(12), 1406-1416.

Menevau, C. and Sreenivasan, K. R. (1990) "Interface dimension in intermittent turbulence", *Physical Review A*, 41, 2246-2248.

Mikkelsen, T., Jørgensen, H. E., Thykier-Nielsen, S., Lund, S. W., and Santabarbara, J. M. (1995). "Final data and analysis report on: High-resolution in plume concentration fluctuations measurements using Lidar remote sensing technique". Technical Report No. Risø-R-852(EN), Risø National Laboratory, Roskilde, Denmark.

Mohamed, M.S. and LaRue, J.C. (1990). "The decay power law in grid-generated turbulence". *Journal of Fluid Mechanics*, 219, 195-214.

Mole, N. (1995). "The α-β model for concentration moments in turbulent flows." *Environmetrics*. 6, 559–569.

Mole, N. and Clarke, E. D. (1995). "Relationships between higher moments of concentration and of dose in turbulent dispersion." *Boundary-Layer Meteorology*. 73, 35–53.

Mole, N., Schopflocher, T.P., and Sullivan P.J. (2008). "High concentration of a passive scalar in turbulent dispersion." Journal of Fluid Mechanics. 604, 447-474.

Moseley, D.J. (1991). "A closure hypothesis for contaminant fluctuation in turbulent flow." M.Sc. Thesis, The University of Western Ontario.

Munro, R. J., Chatwin, P. C. and Mole, N. (2003). "Some simple statistical models for relative and absolute dispersion." *Boundary-Layer Metorology*. 107, 253–271.

Mylne, K.R. and Mason, P.J. (1991). "Concentration fluctuation measurements in a dispersing plume at a range of up to 1000m'. *Q.J.R. Meteorol. Soc.* 117, 253-271.

New Wave. (1997). Laser Manual. United States.

Obukhov, A. M. (1949) "Structure of the temperature field in a turbulent flow", *Izv. Akad. Nauk SSSR, Ser. Fiz.* 6(1-2), 59-63.

Oldershaw, R. L. (1989) "The self-similar cosmological model: Introduction and empirical tests", *International Journal of Theoretical Physics*, 28(6), 669-694.

Ozmidov, R.V. (1960). *Akademiia Nauk SSSR, Doklady Earth Sciences*, Section 126, 536-538.

Papantoniou, D. and List, E.J. (1989). "Large scalar structure in the far field of buoyant jets". *J. Fluid Mech.* 209, 151–190.

Pasquill, F. (1974). "Atmospheric diffusion". Ellis Horwood Ltd. Publisher, Chichester, U.K.

Pope, S. B. (1998). "The vanishing effect of molecular diffusivity on turbulent dispersion: implications for turbulent mixing and the scalar flux." *Journal of Fluid Mechanics*, 359, 299-312.

Pope, S.B., 2000. "Turbulent flows". Cambridge University Press.

Prasad, R. R. and Sreenivasan, K. R. (1990) "Quantitative three-dimensional imaging and the structure of passive scalar fields in fully turbulent flows", *J. of Fluid Mechanics*, 216, 1–34.

Raffel, M., Willert, C., and Kompenhans, J. (1998) "Particle image velocimetry: a practical guide", 2nd ed., Berlin: Springer.

Richardson, L. F. (1922) "Weather Prediction by Numerical Process". Cambridge University Press.

Richardson, L. F. (1926). *Peoc. Roy. Soc.* A 110, 709-737.

Richardson, L. F. and Stommel, H. (1948). *Journal of Meteorology*, 5, 238-240.

Robins, B.E., 1978. Water tunnel turbulence measurements behind a honeycomb. *Journal of Hydronautics*. 12(3), 122-128.

San Gil, I. (2000) "Fractal character of isoscalar surfaces in shear free turbulence and some effect of shear on the turbulence structure", PhD Thesis, Yale University.

Sawford, B.L. and Sullivan, P.J. (1995). "A simple representation of a developing contaminant concentration field". *Journal of Fluid Mechanics*. 289, 141-157.

Schopflocher, T.P. (1999). "The representation of the scalar concentration PDF in turbulent flows as a mixture." Ph.D. thesis, The University of Western Ontario, Canada.

Schopflocher, T. P. (2001). "An examination of the right-tail of the PDF of a diffusing scalar in a turbulent flow." *Environmetrics*. 12, 131–145.

Schopflocher, T.P., Smith, C.J., and Sullivan, P.J. (2007). 'Scalar concentration reduction in a contaminant cloud'. *Boundary Layer Meteorology*. 122. 683-700.

Schopflocher, T.P. and Sullivan, P.J. (1998). "A composite PDF of scalar concentration in turbulent flows." *Environmental Modelling and Software*. 13, 305-308.

Schopflocher, T. P. and Sullivan, P. J. (2002). "A mixture model for the PDF of a diffusing scalar in a turbulent flow". *Atmos. Environ.* 36, 4405–4417.

Schopflocher, T. P. and Sullivan, P. J. (2005). "The relationship between skewness and kurtosis of a diffusing scalar." *Boundary-Layer Meteorology*. 115, 341–358.

Schumacher, J. and Sreenivasan, K. R. (2005) "Statistics and geometry of passive scalars in turbulence", Physics of Fluids, 17, 125107.

Simon, L. and Fitzpatrick, J., (2004). "An improved sample-and-hold reconstruction procedure for estimation of power spectra from LDA data". *Experiments in Fluids*. 37, 272-280.

Smith, T.P. (2004). "Scalar concentration reduction in a contaminant clooud". Ph.D. thesis, The University of Western Ontario, Canada.

Sreenivasan, K. R. (1991) "Fractals and multifractals in fluid turbulence", *Annual Review of Fluid Mechanics*, 23, 539–600.

Sreenivasan, K. R. and Dhruva, (1998) "Is there scaling on high Reynolds turbulence", *Prog. Theor. Pys. Supp.*, 130, 103.

Sreenivasan, K. R., Ramsankar, R., and Meneveau, C. (1989) "Mixing, entrainment and fractal dimension of surfaces in turbulent flow", *Proc. R. Soc. London Ser.* A 421, 79-108.

Stapountzis, H., Sawford, B., Hunt, S. C. R., and Britter, R. F. (1986). "Structure of the temperature field downwind of a line source in grid turbulence". *J. Fluid Mech.* 165, 401–424.

Stathopoulos, T., Hajra, B., and Bahloul, A. (2008). "Analytical evaluation of dispersion of exhaust from rooftop stacks on buildings". IRSST Report No: R-576.

Sullivan, P.J. (2004). "The influence of molecular diffusion on the distribution moments of a scalar PDF". *Environmetrics,* 115, 173-191.

Sullivan, P. J. and Ye, H. (1993). "Further comments on 'Cloud-Averaged' concentration statistics". *Mathematics and Computer in Simulation.* 35, 263-269.

Sullivan, P. J. and Ye, H. (1995). "A prognosis for the sudden release of contaminant in an environmental flow". *Environmetrics.* 6(6), 627-636.

Sullivan, P. J. and Ye, H. (1996). "Moment Inversion for Contaminant Concentration in Turbulent Flows". *Can. Appl. Math. Quart.* 4(3), 301–310.

Sullivan, P.J. and Ye, H. (1997). "The need for a new measure of contaminant cloud concentration reduction". *Il Nuovo Cimento*, 20 (3), 413-423.

Sullivan, P.J. and Yip, H. (1985). "A solution-scheme for the convective diffusion equation". *ZAMP*, 36, 596-608.

Taylor G.I. (1921). "Diffusion by continuous movements". *Proc. London Math. Society*, 2, 196-212.

ten Berge, W. F., Zwart, A. and Appelman, L. M. (1986). "Concentration-time mortality response relationship of irritant and systemically acting vapours and gases." *Journal of Hazardous Materials.* 13, 301–309.

Tennekes, H. and Lumley, J. L. (1972). "A First Course in Turbulence". The MIT Press,

Topping, J. (1957). "Errors of observation and their treatment". The Institute of Physics, London.

Tropea, C., (1995). "Laser Doppler anemometry: recent developments and future challenges". *Measurement Science Technology.* 6, 605-619.

TSI Inc. (2008). Insight3G®, Shoreview, USA.

Veynante, D. and Candel, S.M., (1988). "Application of nonlinear spectral analysis and signal reconstruction to laser Doppler velocimetry". *Experiments in Fluids.* 6, 534-540.

Westerweel J. (1997). "Fundamentals of Digital Particle Image Velocimetry". *Measurements in Science and Technology*, 8, 1379-1392.

Wheeler, A.J. and Ganji, A.R. (1996). "Introduction to Engineering Experimentation". Prentice Hall, 1st Edition, New Jersey.

Wieghardt, K.E.G., (1953). "On the resistance of screens". *Aeronautical Quarterly.* 4, 186-192.

Ye, H. (1995). "A new statistic for the contaminant dilution process in turbulent flows." M.Sc. Thesis, The University of Western Ontario.

Appendix A: Estimation of Turbulence Properties

Defining the length or time scales that are characteristic of the different scales in a turbulent flow is of importance to understanding the process of energy production and dissipation in the flow. In some cases, a suitable scale can be defined by the physical constraints of the flow geometry, for example, in pipe flow the diameter of the pipe is of the order of the largest eddies in the flow. In other cases where the largest scale is not obvious from the flow geometry, an integral length scale (I_L) can be defined that is a measure of the longest connection or correlation distance between two points in the flow that are separated either by distance or time (Hinze 1975). The integral length scale of the velocity is defined by,

$$I_L \equiv \int_o^\infty R(r,t)dr\,, \tag{A1}$$

where, $R(x,t)$ is the autocorrelation function (Figure A1) defined by,

$$R(r,t) = \frac{\langle u'(x,t)u'(x+r,t)\rangle}{\langle u'(x,t)^2\rangle}, \tag{A2}$$

and r is the distance between two points. The Taylor microscale is the largest length scale at which fluid viscosity significantly affects the dynamics of turbulent eddies in the flow (Tennekes and Lumley 1972). The Taylor microscale (λ) is determined by,

$$\lambda = \left[\langle u'^2 \rangle \Big/ \langle (du'/dx)^2 \rangle \right]^{1/2}. \tag{A3}$$

The Reynolds number based on Taylor microscale is given by,

$$\mathbf{Re}_\lambda = \frac{\sqrt{\langle u'^2 \rangle}\,\lambda}{\nu}. \tag{A4}$$

The velocity measurements using PIV are used to compute the integral length scale.

The kinetic energy dissipation rate (ε) is defined by,

$$\varepsilon = 2\nu\left\{(s_{xx})^2 + (s_{yy})^2 + (s_{zz})^2 + 2(s_{xy})^2 + 2(s_{yz})^2 + 2(s_{zx})^2\right\} \tag{A5}$$

where, $s_{xx} = \frac{\partial u'}{\partial x}$, $s_{yy} = \frac{\partial v'}{\partial y}$, $s_{zz} = \frac{\partial w'}{\partial z}$, and

$$s_{xy} = \frac{1}{2}\left(\frac{\partial u'}{\partial y} + \frac{\partial v'}{\partial x}\right),\ s_{zx} = \frac{1}{2}\left(\frac{\partial u'}{\partial z} + \frac{\partial w'}{\partial x}\right),\ s_{yz} = \frac{1}{2}\left(\frac{\partial v'}{\partial z} + \frac{\partial w'}{\partial y}\right).$$

PIV measurements will permit one to compute only s_{xx} , s_{yy} and s_{xy}. The continuity equation for incompressible fluids is

$$\nabla \cdot \mathbf{u} = \frac{\partial u'}{\partial x} + \frac{\partial v'}{\partial y} + \frac{\partial w'}{\partial z} = 0, \tag{A6}$$

which is used to approximate the term s_{zz}. Both the terms s_{yz} and s_{zx} are approximated to be the same as the term s_{xy}. Taylor's frozen turbulence hypothesis assumes that spatial variations of the velocity are fixed and simply advected by the mean flow. This involves the use of a local isotropy assumption in order to calculate the average dissipation rate ($\bar{\varepsilon}$) by ensemble averaging in time. The Kolmogorov scale is calculated using the following expression,

$$\eta = \left(\frac{\nu^3}{\varepsilon}\right)^{1/4}. \tag{A7}$$

The Batchelor scale is calculated as

$$\eta_B = \eta\, Sc^{-1/2}, \tag{A8}$$

where the Schmidt number (Sc) for Rhodamine 6G is 1250 (Barrett 1989).

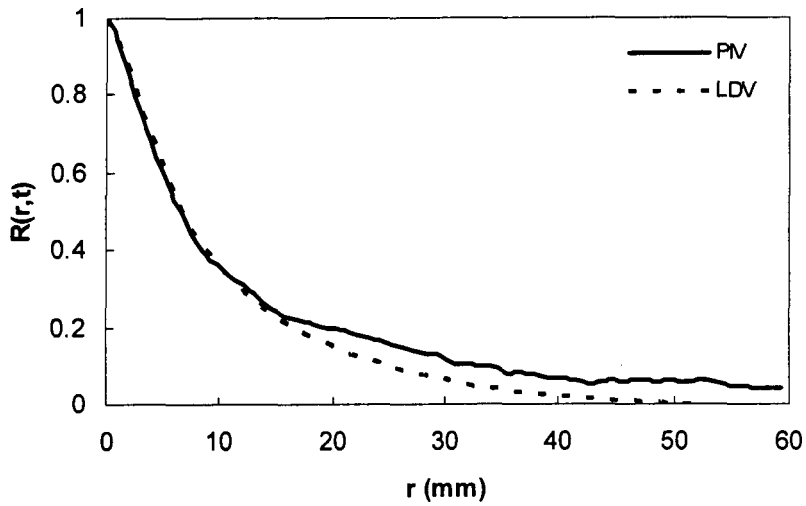

Figure A1: Autocorrelation function at a location 700 mm from the grid by using PIV and LDV.

Appendix B: Sources of Error and Uncertainty Analysis

B.1 Introduction

The errors in experiments have two components: a fixed (bias) error and a random (precision) error (Abernethy and Benedict 1995; Wheeler and Ganji 1996). Since a measurement can be influenced by several different bias errors the total uncertainty due to bias is estimated by using the root-sum-square (RSS) method as follows:

$$B_x = \pm\sqrt{B_1^{\,2} + B_2^{\,2} + B_3^{\,2} + \ldots + B_n^{\,2}}\,. \tag{B1}$$

As with the bias error, when there are several precision errors affecting a measurement, the combined precision error can be estimated as the RSS of the separate uncertainties:

$$P_x = \pm\sqrt{P_1^{\,2} + P_2^{\,2} + P_3^{\,2} + \ldots + P_n^{\,2}}\,. \tag{B2}$$

Once the bias and precision uncertainties have been obtained, the total uncertainty T of a measurement can be estimated by combining them as:

$$T_x = \sqrt{B_x^{\,2} + (tP_x)^2}\,, \tag{B3}$$

where, t is the value of the Student-t statistic for a chosen level of confidence. Student-t distribution is used in cases of small sample sizes, to estimate the confidence interval of the mean value of the sample for a specific confidence range and for the present study a value of 2 is used for a 95% confidence level.

B.2 Uncertainty propagation

In general, a quantity that is being measured is often a function of other measured quantities. The Taylor Series Method is applied here to evaluate the propagation of

uncertainties of the different variables into a determined quantity. If we consider a general case in which a quantity r is a function of j measured variables X_j,

$$r = f\left(X_1, X_2, \ldots X_j\right). \tag{B4}$$

The error in each measured quantity will affect the result by different amounts. The expression of the uncertainty of the quantity r was given by Coleman and Steele (2009) assuming that the variables X_j and their uncertainties are independent of each other,

$$T_r^2 = \left(\frac{\partial r}{\partial X_1}\right)^2 T_{X_1}^2 + \left(\frac{\partial r}{\partial X_2}\right)^2 T_{X_2}^2 + \ldots + \left(\frac{\partial r}{\partial X_j}\right)^2 T_{X_j}^2, \tag{B5}$$

where T_{X_j} are the uncertainty in each measured value X_j. When the quantity is dependent on a product of the measured variables X_j:

$$r = X_1^a X_2^b \ldots X_j^n, \tag{B6}$$

the uncertainty of the quantity r is (Coleman and Steele 2009)

$$\frac{T_r}{r} = \left[\left(a\frac{T_{X_1}}{X_1}\right)^2 + \left(b\frac{T_{X_2}}{X_2}\right)^2 + \ldots + \left(n\frac{T_{X_j}}{X_j}\right)^2\right]^{1/2}. \tag{B7}$$

B.3 Error in the concentration (PLIF) measurements

The uncertainty in a PLIF measurement arises from many contributing factors. These include camera noise, laser power fluctuations, attenuation, photobleaching, variation in source concentration, and calibration error. Some of them are considered negligible in these experiments.

Camera noise: For the CCD camera, the noise levels were reported to have a standard deviation of the order of two grey scales (Ferrier et al. 1993). A series of 500

images were taken with a dark background (camera was covered with black cloth in a dark room) to check the noise levels and the standard deviation was found to be of the same order. Based on the noise level in the camera sensor, the errors are converted to concentration scale ($\mu g/l$) for different downstream locations at the centreline of the plume. The errors are found to be ± 0.048 $\mu g/l$, ± 0.025 $\mu g/l$, ± 0.04 $\mu g/l$ and ± 0.05 $\mu g/l$ at locations 0.5 m, 0.7 m, 1.2 m and 1.8 m downstream respectively.

Laser power fluctuation: The stability of the laser energy was provided by the manufacturer (NewWave Corp.), which was 0.59%. Given the linear relationship between fluorescence intensity and power of the incident radiation, the resulting uncertainty in measured concentration or intensity is also 0.59%.

Attenuation: As the laser sheet passes through water and fluorescent dye, it will attenuate as its energy is absorbed by the fluorescent dye. The attenuation correction was carried out using Beer-Lambert law (equation (3.6) in Chapter 3). The error in using attenuation correction is calculated to be 0.005%.

Photobleaching and thermal blooming: Photobleaching can have an effect on the detected signal as the fluorescence emitted by a fluorescent dye will decrease under constant laser irradiation. Thermal blooming can occur if the dyed fluid absorbs energy from the laser causing an increase in temperature. This temperature increase can lead to a density differences in the fluid and also possibly cause refraction gradients that will affect

the fluorescence signal (Lavertu et el., 2008). In the present study, the effects of photobleaching and thermal blooming are considered to be negligible.

Calibration error: The calibration method described here is based on the fact that there is constant flux through each cross-section of the fluorescent plume. Since the calculation is based on mean parameters, this reduces a great deal of uncertainty in the calibration procedure. The uncertainty involved in the calibration curve is considered here and the standard error in the calibration curve (s) is calculated using the following formulation (Larose 2006)

$$s = \sqrt{MSE} = \sqrt{\frac{SSE}{n-m-1}}, \tag{B8}$$

Where, MSE is the mean squared error, SSE is the sum of squared errors, n is the number of sample and $m = 1$ for linear regression. The estimated error involved in the calibration curve is found to be 2%.

Among the sources of error described above, the errors in camera noise and laser power fluctuation are considered to be bias errors and the errors from attenuation, photobleaching and calibration are precision errors. Table B.1 represents the sample calculations of bias and precision error estimations for a location 0.5 m downstream of a point source. The total error at a location 0.5 m behind the point source is calculated to be ± 0.085 $\mu g/l$. Similarly, the total errors in the concentration measurements are calculated for further location and found to be ± 0.05 $\mu g/l$, ± 0.03 $\mu g/l$ and ± 0.025 $\mu g/l$ at 0.7 m, 1.2 m and 1.8 m downstream respectively. Errors involved in the concentration

measurements are also estimated here and found to be ± 0.0008 $\mu g/l$, ± 0.0006 $\mu g/l$ and ± 0.001 $\mu g/l$ at 0.15 m, 0.5 m and 0.7 m downstream respectively.

Table B.1: Summary of bias and precision errors at x = 0.5 m behind the point source.

Bias Limit		
Camera noise	± 0.048 $\mu g/l$ = ± 3.0 % = ± 3.0/100	Total Bias Limit $=\pm\sqrt{\left(\frac{3}{100}\right)^2+\left(\frac{0.59}{100}\right)^2}$ = ± 3.06 %
Laser power fluctuation	± 0.59/100	
Precision Index		
Attenuation	± 0.005/100	Total Precision Index $=\pm\sqrt{\left(2\times\frac{0.005}{100}\right)^2+\left(2\times\frac{2}{100}\right)^2}$ = ± 4.0 %
Calibration	± 2.0/100	
Total Uncertainty	$=\pm\sqrt{\left(\frac{3.06}{100}\right)^2+\left(\frac{4.0}{100}\right)^2}$ = ± 5.0 % = ± 0.085 $\mu g/l$	

B.4 Error in the velocity (PIV) measurements

The velocity vector obtained through an interrogation area for any flow conditions by the PIV system defined as:

$$u = \frac{x}{t} r \quad , \tag{B9}$$

where x is the average pixel displacement of the particles in the interrogation area, t is the time between the two laser pulses and r is the ratio between the object size and the image

size. In the case where the velocity vector is not rejected by one of the filters it is possible to estimate the measured velocity error in the following equation (Gurka 2003):

$$\frac{\Delta u}{u} = \frac{\Delta x}{u}\frac{\partial u}{dx} + \frac{\Delta r}{u}\frac{\partial u}{dr} + \frac{\Delta t}{u}\frac{\partial u}{dt}. \qquad \text{(B10)}$$

The pixel displacement, Δx, was estimated by Westerweel (1997) to be 0.05 pixels for a 32 x 32 pixels interrogation window. Δt is assumed to be as one thousand of the time between the two laser pulses ($\Delta t \approx 3\mu s$) based on Gurka (2003). Δr is considered to be the same as the calculated value in Gurka (2003) that is $1\text{x}10^{-6}$ m/pixels. The total error is calculated based on the following experiment parameters: $u = 0.2$ *m/s*, $t = 3000$ μs, $x = 5$ - 6 pixels, $r = 3.4\text{x}10^{-5}$ *m*/pixel. The error in a velocity measurement is estimated to be ~1.5%. A rule of thumb of calculating the error in velocity measured by PIV was given by Westerweel (1997) that is 0.05 to 0.1 pixels for a 32 x 32 pixel interrogation window, which implies a relative measurements error of about 1% for a displacement that is one quarter of the interrogation window.

B.5 Error in the closure approximations

In order to calculate the propagated error in closure approximations, equation (B7) is used. In the convective closure approximation, the terms $d\langle u'\Gamma'^{n+1}\rangle/dx$ and $d(y\langle v'\Gamma'^{n+1}\rangle)/dy$ contain highest probable error due to the combined effect of velocity and concentration. The errors in the terms $u'\Gamma'^{n+1}$ and $v'\Gamma'^{n+1}$ are calculated and assumed to be the same as the error in the gradient terms based on the analysis given in Topping (1957) that is the maximum error in a quotient is the sum of the individual errors, where

the error in dx is negligible compared to the closure terms. The governing formulation based on (B7) is

$$\frac{T_r}{r} = \left[\left((n+1)\frac{T_\Gamma}{\Gamma} \right)^2 + \left(\frac{T_u}{u} \right)^2 \right]^{1/2}, \tag{B11}$$

where, T_r is the error in the product, T_Γ and T_u are the errors in concentration and velocity measurements. Table B.2 is prepared with the estimated errors in the product for different downstream locations for 3 moment values (n = 1, 2, 3). The values in Table B.2 are used to give the error bar in Figures 4.7 – 4.12.

Table B.2: Summary of the error estimation in the convective closure terms

Point Source			
	n = 1	n = 2	n = 3
x = 0.5 m	10%	15%	20%
x = 0.7 m	11%	16.5%	22%
x = 1.2 m	16%	24%	32%
x = 1.8 m	18%	27%	36%
Line Source			
x = 0.15 m	8.5%	12.5%	16.5%
x = 0.5 m	9%	13%	17%
x = 0.7 m	10%	15%	20%

The uncertainty analysis is kept limited to the convective closure approximation calculation due to the fact that the most significant error is involved in only the closure calculations.

Appendix C: Further Details of the Experiments

C.1 Calculation of particle relaxation time for Silicon Carbide

Both the LDV and PIV rely on scattering particles suspended in the flow to provide the velocity information for a continuous medium. Therefore, the accuracy of the velocity field depends on the capability of the scattering particles to follow the instantaneous motion of the medium (Melling 1997). To determine whether this particle size is suitable, the Stokes number was evaluated (AbuOmar 2002), $St = \tau_p / \tau_f$, where τ_f is the time scale of fluid motion and τ_p is the particle relaxation time. The particle relaxation time is defined as

$$\tau_p = \frac{\rho_p d_p}{18 \mu f}, \tag{C1}$$

where ρ_p is particle density, d_p is particle diameter, μ is the dynamic viscosity of the medium, and f is the ratio of the actual drag to the Stokes drag and can be calculated as,

$$f = 1 + 0.15 \mathrm{Re}_p^{0.687}; \quad \mathrm{Re}_p = \frac{\rho U_s d_p}{\mu}, \tag{C2}$$

where ρ is the fluid density and U_s is the slip velocity and is approximated as the maximum extreme velocity fluctuation (i.e., three times the maximum standard deviation). Particles with Stokes numbers much less than unity have ample time to respond to changes in the flow velocity. The particle relaxation time of Silicon Carbide for the present flow condition was calculated to be ~0.35 milliseconds (ms), which can be comparable with the response time of a particle (~0.4 ms) that has been calculated applying drag force acting on a sphere (Holmes 2004). Thus, a conservative estimate

(St < 0.1) based on the particle diameter of 2 μm yields that the particle will follow fluctuation of τ_f > 3.5 ms or 285 Hz.

C.2 Resolution in simultaneous PIV and PLIF measurements

As it was mentioned in Chapter 3, the CCD cameras had an array of 1600 x 1200 pixels. In order to get velocity measurements using PIV, the PIV images were divided into regular 32 x 32 pixels interrogation bins with a 50% overlap, which gave a total of 7326 velocity vectors on a measurement plane in an array of 99 x 74. For concentration measurements, the PLIF images were divided into regular 4 x 4 pixels interrogation bins, averaged over the 4 x 4 pixels, which gave a planar array of 400 x 300 concentration measurements. Therefore, for every 4 x 4 concentration array, there was a velocity vector representing the instantaneous velocity over the area of 4 x 4 concentration array (see Figure 3.21b). In order to compute the instantaneous concentration flux from simultaneous velocity and concentration measurements, the velocity was multiplied by the concentration value that was averaged over the centre 2 x 2 concentration array. The resolutions of the PLIF measurements were 0.13, 0.14, 0.17 and 0.18 mm at distances 500, 700, 1200 and 1800 mm downstream of the gird, respectively, for the point source measurements. For line source measurements the resolution in PLIF measurements was 0.2 mm. It is evident that the spatial resolution in PIV measurements was four times the spatial resolution in PLIF measurements.

C.3 Spatial calibration of PIV and PLIF measurements

The spatial calibration of PIV and PLIF measurements was done by blocking the laser sheet with a black strip of thin metal (dimension was know) at the bottom of the water tunnel, which would create a dark strip in the PIV image when the PIV camera was lowered vertically from the centreline of the tunnel to the bottom wall of the tunnel. The lowering was done carefully so that there were no displacements of the camera in any direction other than vertical. A calibration image is presented in Figure C1.

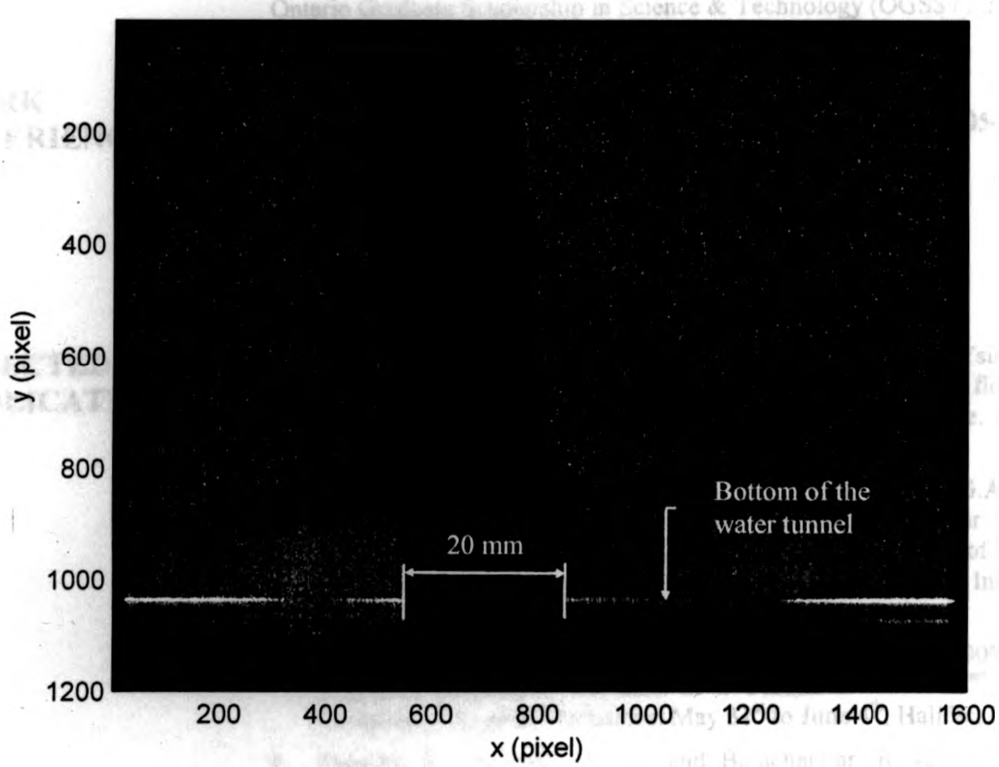

Figure C1: A spatial calibration image for PIV measurements.